VITA-SALUTE SAN RAFFAELE UNIVERSITY

Faculty of Medicine and Surgery

International PhD course in Molecular Medicine

Curriculum in Basic and Applied Immunology and Oncology

DYNAMICS OF CD8$^+$ T CELL DYSFUNCTIONAL DIFFERENTIATION UPON INTRAHEPATIC PRIMING AND MECHANISMS OF IL-2 MEDIATED RESTORATION

DoS: Prof. Matteo Iannacone
Second Supervisor: Prof. Dietmar Zehn

PhD thesis by: Giorgia De Simone
Registration number: 013819
XXXIV PhD cycle
SSD BIO/13

Academic Year 2020/2021

VITA-SALUTE SAN RAFFAELE UNIVERSITY

Faculty of Medicine and Surgery

International PhD course in Molecular Medicine

Curriculum in Basic and Applied Immunology and Oncology

DYNAMICS OF CD8$^+$ T CELL DYSFUNCTIONAL DIFFERENTIATION UPON INTRAHEPATIC PRIMING AND MECHANISMS OF IL-2 MEDIATED RESTORATION

DoS: Prof. Matteo Iannacone
Second Supervisor: Prof. Dietmar Zehn

PhD thesis by: Giorgia De Simone
Registration number: 013819
XXXIV PhD cycle
SSD BIO/13

Academic Year 2020/2021

CONSULTAZIONE TESI DI DOTTORATO DI RICERCA

I, **De Simone Giorgia**

registration number: **013819**

born at: **Nardò** (LE)

on: **12/12/1993**

author of the PhD Thesis titled:

DYNAMICS OF CD8$^+$ T CELL DYSFUNCTIONAL DIFFERENTIATION UPON INTRAHEPATIC PRIMING AND MECHANISMS OF IL-2 MEDIATED RESTORATION

AUTHORIZES the public release of the thesis.

Date

Signature

DECLARATION

This thesis has been composed by myself and has not been used in any previous application for a degree.
The results of this thesis have been published (*Bénéchet, De Simone et al. Nature 2019; De Simone et al. Immunity 2021*).
Part of the text, figures and material and methods were taken from *Bénéchet, De Simone et al. Nature 2019* and *De Simone et al. Immunity 2021*.
Figures in chapter 1-4 are used for educational purpose.

Results in chapter 10 of the thesis were obtained with the following other co-authors:

1. *Experiments in chapters 10.1.-10.4. were performed with Dr. Alexandre Bénéchet, PhD, Lausanne, Switzerland.*
2. *Experiments in chapters 10.5.-10.9. were performed with Dr. Francesco Andreata, PhD and Dr. Valeria Fumagalli, PhD, Iannacone lab, San Raffaele Scientific Institute, Milan, Italy.*

The results presented here were obtained by myself, except for:

1. *Western Blot experiment in fig. 13 (G) was performed by Dr. Paola Zordan, PhD, Iannacone lab, San Raffaele Scientific Institute, Milan, Italy.*
2. *Sample preparation and genomic analyses in fig. 15 (A-G) were performed in collaboration with Dr. Renato Ostuni's lab, San Raffaele Scientific Institute, Milan, Italy.*
3. *Sample preparation and genomic analyses in fig. 20 were performed in collaboration with Dr. Florent Ginhoux's lab, Institute Gustave Roussy, Villejuif, France.*
4. *Genomic analysis in fig. 19 (H-K), 20, 21 (D-E) were performed by Dr. Chiara Laura, Iannacone lab, San Raffaele Scientific Institute, Milan, Italy.*
5. *Immuno fluorescence experiment in fig 21 (C) was performed by Dr. Xenia Ficht, PhD, Iannacone lab, San Raffaele Scientific Institute, Milan, Italy.*
6. *Serum alanine aminotransferase (ALT) were measured by Dr. Raso Michele, Mouse Clinic, San Raffaele Scientific Institute, Milan, Italy.*
7. *Liver tissues for immunohistochemistry were processed by Dr. Amleto Fiocchi, Animal Histopathology Facility, San Raffaele Scientific Institute, Milan, Italy.*

All sources of information are acknowledged by means of reference.

1. ABSTRACT

The liver possesses a unique immunological niche within the body. Due to its constant exposure to microbial products, it is known to be biased to a more tolerogenic environment, however the mechanism driving this tolerance are still hill-defined.

In this work, we have dissected the spatiotemporal dynamics of liver tolerance by studying $CD8^+$ T cell priming restricted to hepatocytes and the $CD8^+$ T cell priming directed to hepatic Ag-presenting cells (hAPC). We observed that hepatocellular priming leads to moderate *in situ* expansion of $CD8^+$ T cells that fail to differentiate into effector cells, thus acquiring a dysfunctional phenotype. By contrast, priming by hAPC leads to vigorous expansion followed by development of cytolytic function and of IFN-γ expression. Taking advantage of intravital microscopy techniques, we observed that effector $CD8^+$ T cells were poorly motile and clustered outside the liver sinusoids all throughout the parenchyma. On the other hand, dysfunctional $CD8^+$ T cells remained intravascular, accumulated in the peri-portal area, and showed higher motility. Interestingly, exogenous IL-2 administration was able to partially revert $CD8^+$ T cell dysfunction both at gene expression and effector function levels. In this regard, we have identified a subtype of hepatic macrophages (Kupffer Cells, KCs), referred as KC2, which is more prone to sense IL-2 and to cross-present hepatocellular antigens to T cells, thus improving their antiviral function. Altogether these data suggest that T cell priming through KC2 could overcome the tolerogenic hepatic microenvironment and maybe use as new strategies for boosting hepatic T cell immunity.

2. TABLE OF CONTENTS

3. ACRONYMS AND ABBREVIATIONS

Ag: Antigen

APC: Antigen Presenting Cell

IFN: Interferon

IL2: Interleukin 2

KC: Kupffer Cell

LSEC: Liver Sinusoidal Endothelial Cell

LN: Lymph Node

DC: Dendritic Cell

IHL: Intrahepatic Leukocytes

NK: Natural Killer

TCR: T Cell Receptor

LPS: Lipopolysaccharide

HCV: Hepatitis C Virus

HBV: Hepatitis B Virus

MHC: Major Histocompatibility Complex

HCC: Hepatocellular Carcinoma

sALT: Serum Alanine Aminotransferase

ISG: Interferon Stimulated Genes

LSCM: Laser Scanning Confocal Microscopy

GFP: Green Fluorescent Protein

T_N: T naïve

MUP: Major Urinary Protein

WT: Wild Type

LCMV: Lymphocytic Choriomeningitis Virus

AAV: Adeno Associated Virus

ATAC: Assay for Transposase-Accessible Chromatin

GSEA: Gene Set Enrichment Analysis

IGV: Integrative Genome Viewer

NES: Normalized Enrichment Score

LV: Lentivirus

CLL: Clodronate Liposomes

BM: Bone Marrow

LNPCS: Liver Non-Parenchymal Cells

UMAP: Uniform Manifold Approximation and Projection

DT: Diphtheria Toxin

4. LIST OF FIGURES AND TABLES

5. CHAPTER ONE

1.1. Liver Anatomy

The liver is a vital organ that fulfills functions in the metabolism of carbohydrates, proteins, and lipids (by the bile production). It is the largest organ of the body, accounting for 2 to 3% of the total weight.

Mouse liver consists of four lobes, named as right, medial, left and caudate [1]. The right lobe has a transverse septum that approximately divide the organ in half; the medial lobe is the most prominent, while the left lobe is the largest. The caudal lobe is small and has two distinct segments and is located craniodorsal to the stomach[1].

The human liver has four lobes as well (right, left, caudate and quadrate), and is located in the upper quadrant of the abdomen, beneath right hemidiaphragm[2].

There are several differences between human and mouse liver in term of lobe patterns and location: mouse liver, indeed, occupies the entire subdiaphragmatic space, while human liver is transversely located in the right upper quadrant of the abdomen and it is suspended by surface ligaments,that are not present in the mouse.

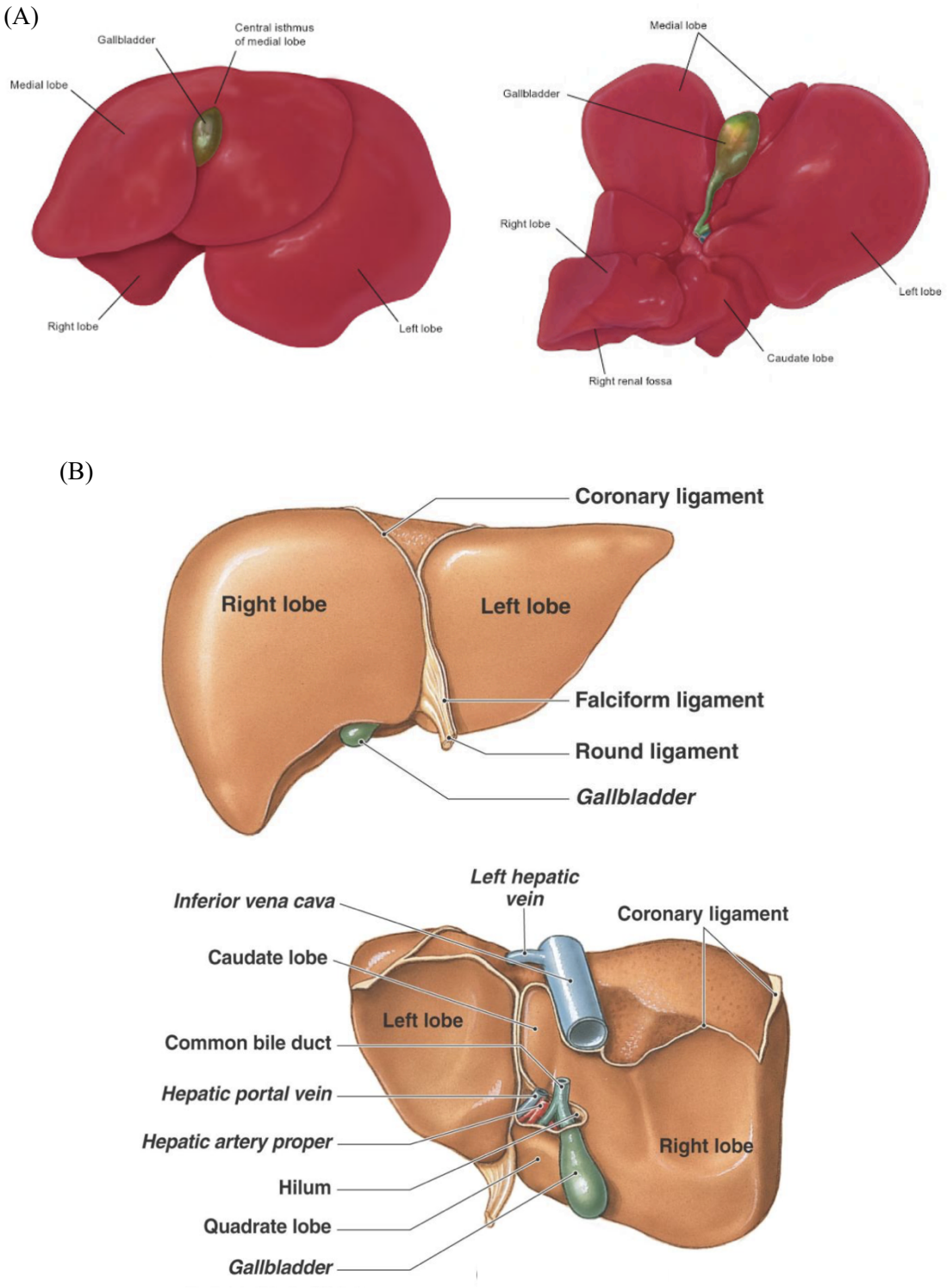

Figure 1. *Regional liver anatomy.*

(A) *Mouse liver with four lobes: left (largest), right (hemisected), medial and caudate. Source: www.netterimages.com*

(B) *Human liver with four lobes: right (largest), left, caudate and quadrate.*

Although there are differences macroscopically, the micro-organization of lobular units is well conserved between species.

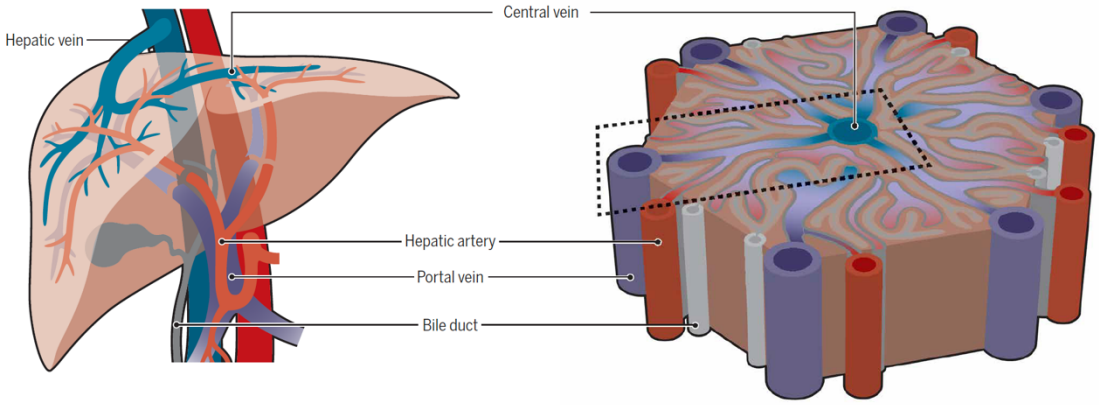

Figure 2. *Liver anatomy.*

*(**Left**) Macro-anatomy of the human liver receiving dual blood supply, with nutrient-rich blood from portal vein and oxygenated blood from the hepatic artery. Blood exits via the hepatic vein. The gall bladder collects bile produced by hepatocytes and releases it into the gastrointestinal tract via the bile duct. (**Right**) Overview of a liver lobule. Each lobule is flanked by portal tracts, composed of bile ducts, lymphatics, and the incoming dual blood supply. The blood flows in the sinusoids, the terminal branches of the liver vasculature, and exits via central veins. (Ficht X & Iannacone M. 2020).*

The lobule is the functional unit of the liver parenchyma, and its activity is strictly linked to the anatomical organization of vessels and hepatocytes.

The liver tissue is organized around vascular bundles, known as “portal tract” or “portal triad”, that contains a branch of the portal vein, an arteriole, and a tributary of the bile duct: nutrient-rich blood coming from the gastrointestinal tract is collected and sent to the organ by the portal vein, which provide most of the blood that is flowing through the liver. Arterial oxygen-rich blood coming from hepatic artery mixes with venous blood in the liver sinusoids, specific hepatic vessels that show an unusual morphology. Liver sinusoidal endothelial cells (LSECs), the main components of liver sinusoids, are organized in a discontinuous way (forming the so called “fenestrae”) and lack of a basal membrane, allowing the function of digestion and detoxification of the organ thanks to the exchange of molecules between blood and hepatocytes.

The blood flows from the portal tracts to the central veins, passing between hepatocytes through spaces defined by the LSECs. Blood plasma pass from the sinusoid into a sub-endothelial space (space of Disse), from which lymph is collected and sent to the lymphatic vessels that goes from the portal tract to the draining lymph nodes[3] (LNs) (celiac and portal LNs[4]).

A population of DCs and macrophages (named Kupffer cells, KCs) can be found in the hepatic sinusoids and have a role in phagocytosis and antigen presentation of particles and pathogens that enter in the liver[5].

1.2. The liver as a lymphoid organ

The liver is a complex organ, fulfilling a multitude of functions: it has not only an excretory, detoxifying and metabolic property, but it can also be considered, by its structure and cellular composition, as a lymphoid organ[6].

Indeed, one characteristic of a lymphoid organ is a structure that facilitates encounter between APC and lymphocytes. The liver is playing the role of an immune platform by facilitating arrival and arrest of lymphocytes into sinusoids, where different subsets of APCs are present.

The liver microcirculation consists of sinusoids of 200-250µm in length and of 7-15µm in diameter, in which blood flow velocity varies greatly between different segments (from 100 to 400µm/s). Therefore, a lymphocyte of about 8µm in diameter is just fitting the size of the vessel, allowing contacts and interactions with adhesion molecules and receptors on the cells lining the sinusoid, such as LSECs and Kupffer cells. Moreover, endothelial fenestrations permit cellular trans-sinusoidal protrusions for direct contact with hepatocytes and DC in the space of Disse.

Altogether, the confine micro-environment, combined with a low blood flow, is fostering arrest and contacts between lymphocytes and APC populations.

In accordance with this idea the liver is populated by a heterogeneous population of immune cells, called intrahepatic leukocytes (IHL).

20–25% of IHL are NKs ($CD3^+$ and $CD56^+$), while a higher percentage (30-35%) of IHL is composed by T cells carrying a γδ receptor (mostly $CD8^+$); these cells carry an invariant TCR, but they can recognize a modest number of different ligands: is thought that these cells act against potentially dangerous antigens coming from the gut, but they can also have an immuno-modulatory phenotype. On the other hand, T cells carrying the αβ TCR pass throughout the organ, entering from hepatic and portal blood.

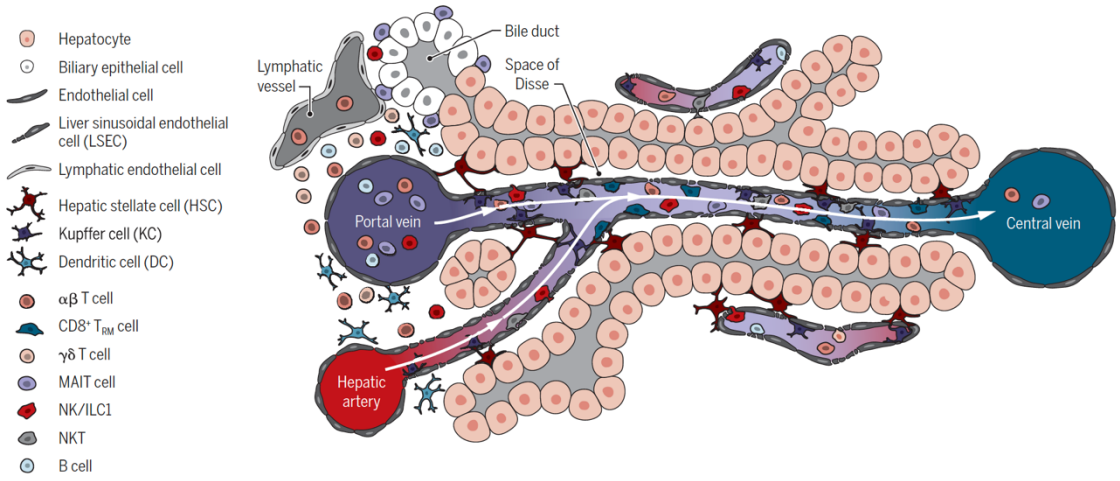

Figure 3. *Schematic representation of liver cell subsets.*

Hepatocytes arranged in cords produce bile, which is collected by bile ducts in the portal area. Fenestrated LSECs line the terminal vessels, and other specialized endothelium is found in portal and central veins as well as in lymphatic vessels. Arrows indicate direction of blood flow. HSCs locate within the space of Disse and are in close contact with KCs. DCs are found mainly around portal tracts. Other immune cell subsets contained within the liver include B cells, MAIT cells, γδ T cells, conventional αβ T cells—including $CD8^+$ tissue TRM—group 1 innate lymphoid cells (ILCs) such as NK cells and ILC1, and NKT cells. (Ficht X & Iannacone M. 2020).

1.3. The liver as a lymphoid organ biased towards tolerance

The presence in the organ of so many distinct subsets of immune cells, along with a multitude of APCs, raises the question of whether the liver can mount a productive immune response. However, the liver is generally bias toward a state of immune unresponsiveness, known as "tolerance". Mechanisms behind this phenomenon are still poorly understood[7]. The first obvious observation that can explain liver tolerance is the fact that the liver receives blood from the intestine, which is rich in microbial products. Constant arrival of bacterial derivatives is indeed modifying the local innate immune microenvironment. For instance, the lipopolysaccharide endotoxin (LPS), derived from the cell wall of the gram-negative bacteria, has been found at a concentration of 1ng/ml in the portal venous blood, while it is absent in the systemic circulation. LSECs, as well as Kupffer cells, express the LPS receptor and can effectively remove this molecule before it is released in the systemic circulation, protecting the host from endotoxemia[8,9].
In previous studies, setting up a major paradigm for liver tolerance, it has been shown that the capture of the LPS by Kupffer cells is leading to the secretion of the immunosuppressive cytokine IL-10. Balmer et al. have shown that, in the context of intestinal pathology, the liver is acting as a "vascular firewall", by capturing gut commensal bacteria that are entering the blood-stream[10].
Moreover, liver disease, such as nonalcoholic steatohepatitis in human, is leading to systemic immune response, consistent with increased extra-intestinal commensal exposure. Finally, interesting gene therapy studies have shown that targeting the transgene to hepatocytes can induce tolerance toward the therapeutic antigen[11].
Therefore, it seems that liver-resident immune cells are not completely passive to stimuli, but they rather exist in a state of "active tolerance"[6].

Such an immunosuppressive environment can explain in part why, in some cases, liver T cell priming is inadequate. In the case of chronic HCV and HBV infections, antigen-specific $CD8^+$ T cells exhibit a dysfunctional phenotype, with low expression levels of the IL-7 and IL-2 receptors, along with high levels of the inhibitory receptor PD-1 and failure to express effector molecules, such as IFN-γ or TNF-α[12,13].

More importantly, liver can induce a systemic tolerance and this phenomenon has been highlighted in the context of liver allograft. Indeed, it has been shown that, in animal models of liver transplantation, liver allografts are spontaneously accepted, even with MHC incompatibility[14]. In addition, liver transplants induce donor-specific tolerance in immune-competent recipients: this is translated by the acceptance of subsequent tissue transplants (e.g. skin or heart) from the same donor and rejection of graft coming from another donor[15].

In rodents, the acceptance of liver allografts is associated with early deletion of donor MHC-specific T cells; on the other hand, the number of recipient T cells that show a suppressor phenotype slowly increase in mice who have accepted the graft[16].

The detection of a small number of donor-derived leukocytes in multiple tissues of recipient mouse after a liver transplant is called “microchimerism”, and is it consider as an explanation for liver transplant tolerance. However, other possibility for hepatic tolerance can be explain by the presence of antigen presenting cells populating the liver parenchyma, such as Kupffer cells, LSECs, and stellate cells that can induce immune tolerance through the inhibitory co-signals like IL-10 or PD-L1. Given this hypothesis, recipient precursor T cells would enter the transplanted liver, undergo activation interacting with liver APCs, and then either undergo tolerance or deletion owing to inhibitory local signals. This model could also explain the unresponsiveness of the liver to food antigens or gut microbiota products in steady-state conditions: it has been shown that the delivery of ovalbumin (widely used as an antigen for immunization) into the stomach of mice models results in a systemic tolerance of $CD4^+$ T and $CD8^+$ T cells. In contrast, if the venous drainage of the gut is surgically disrupted, the tolerance is lost. In the context of tolerance model of oral-administered antigens, isolated and *ex vivo* cultured LSECs can interact with antigen-specific T cells, driving them to an anti-inflammatory phenotype.

The induction of systemic tolerance could also be driven by liver APCs, and it can be the result of both peripheral deletion of activated T cells and to the induction of antigen-specific T regulatory cells (Tregs). Indeed, circulating $CD8^+$ T effector cells are sequestered in the liver, even in the absence of antigen: for example, in the context of influenza virus (in which the infection is usually confined to the respiratory tract),

influenza-specific $CD8^+$ T cells are found in the liver, associated with Kupffer cell-rich inflammatory foci and with mild hepatocyte damage[6].
Moreover, liver can act as an "activated $CD8^+$ T cell graveyard", sequestering circulating activated T cells that are not rapidly localizing to the site of infection or to sites where they can mature into long-lived memory cells and induce their apoptosis. In this model, the liver acts shaping the size of T cells response, having at the same time an impact on the pool of memory T cells[17].

Not every T cell that enters the liver is deleted: it seems that recently activated lymphoblasts preferentially localize to hepatic sinusoids, being then recruited, and killed by Kupffer cells; on the other hand, resting memory cells may be over-represented in the liver (thanks to the high expression of adhesion molecules on LSECs), but are not able to activate Kupffer cells, therefore resting in the parenchyma without being phagocyted.

Suppressor T cells, also known as Tregs ($CD4^+$, $CD25^+$, $FoxP3^+$, $CTLA4^+$), can be another player in the regulation of activated T cell as well. In mouse models of liver transplantation, Tregs increase in abundance after liver grafting, and depletion of these cells causes acute rejection of the graft[3].

1.4. Hepatic resident antigen-presenting cells

The liver harbors the largest proportion of macrophages among all solid organs in the body[5]. In a healthy murine liver, every 100 hepatocytes are accompanied by 20–40 phagocytic cells[18] with several functions, including i) scavenging of bacteria and microbial products that reach the liver from the intestine via the portal vein, ii) sensing disturbances in tissue integrity and iii) serving as a gatekeeper for initiating or suppressing immune responses. Here, a self-sustained, locally proliferating population of phagocytes (KCs) can be distinguished from monocyte-derived, infiltrating macrophages that functionally differentiate *in situ*[19].

KCs, which represent about 35% of all hepatic non-parenchymal cells (HNPCs)[20], are mainly intravascular and remove damaged erythrocytes from the blood through the expression of Fc receptors and scavenger receptors. They originate from fetal liver-derived erythromyeloid progenitors and they principally rely on self-renewal for their maintenance[21], despite the fact that under some conditions bone marrow-derived monocytes can give rise to fully differentiated KCs[22]. Murine KCs can be characterized by the expression of F4/80, C-type lectin domain family 4 member F (CLEC4F) and by multiple Toll-like receptors (TLRs) like TLR4 and TLR9. KCs display all the characteristics to be professional APC but a number of experimental evidence (as the production of the immunosuppressive cytokine IL-10 upon LPS stimulation [8], suggest that they are preferentially biased towards a tolerogenic response. Under homeostatic condition, KCs express low levels of MHCII, CD80/86 and CD40 molecules compared to DCs (which represent the paradigmatic APCs) suggesting that KCs could act as ”incompetent” APCs[23] and promote T cell tolerance. However, it has been recently suggested that, under stimulation with anti-CD40 Ab (able to induce APCs activation), the capacity of KCs to act as APCs increase, leading to a full activation of Ag-specific T cells[24]. This function of KCs as functional APCs can also be modulated by innate signals since both reactive oxygen species and TLR3 ligation can increase the expression of tolerance-driving APC to immunogenic APC. So far, is clear that based on the context KCs cells can switch their immunological role from

The liver also contains several DCs populations, including myeloid DCs (mDC) and plasmacytoid DCs (pDC) that can present Ags. Compared to the same cells isolated from

the spleen, mouse liver mDC shown a reduction in the capacity to activate T cells, probably due to the high presence of IL-10 within the liver microenvironment[25]. Unlike KCs, mDCs traffic through the liver and migrate from the parenchyma to the portal tract[26].

6. CHAPTER TWO

6.1. HBV

Hepatitis B virus (HBV) is responsible, together with Hepatitis C virus (HCV), of most of the liver disease throughout the world. In particular, HBV infection is most commonly associated with acute or fulminant hepatitis, but it can also cause chronic infection that leads to the development of liver cirrhosis and eventually hepatocellular carcinoma (HCC)[27].

The natural history of HBV infection varies between young and adult subjects; the vertical transmission from the mother to the neonate or the acquisition of the virus during childhood is usually associated whit a subclinical acute infection, with high chance of chronicity (30 to 90% of cases)[28].

In the adult, instead, HBV causes an acute symptomatic hepatitis in about 30% of infected patients, with acquisition of lifelong protective immunity. Also, the risk of evolving into chronic disease in the adult is low (less than 5%) if compared to neonatal infection; finally, in adult patient fulminant hepatitis is rare (0,1-0,5%), whit higher risk in the case of co-infection with other hepatitis viruses.

HBV is a member of *Hepadnaviridae* family, and its genome consists in a relaxed circular (RC) DNA of approximately 3200 nucleotides. The virus is spherical, with a diameter of about 42nm; the outer component of the particle, the viral envelope, consists of a lipoprotein membrane (acquired from the host cell during the budding from multivescicular bodies), into which are included three forms of the viral envelope protein, also known using its serological name as "s antigen" (HBsAg): large (L), middle (M) and small (S). These proteins have two distinct functions: first, they are the main components of the virus envelope; second, they assemble into aggregates that will be secreted as sub viral particles. The capsid, a protein structure that can be found inside the envelope, is made of core antigen (HBcAg), a 185-aa-long polypeptide of MW 21kDa, derived from the "core region" of the viral DNA. This region codifies also for the pre-core protein, also known as its serologic name "e-antigen" or HBeAg: this protein is translated from a "pre-C RNA", with 5' ends located a few nucleotides upstream the first codon (AUG) in the core open reading frame. A signal sequence directs early antigen (HBeAg) to the secretory pathway, allowing its release from the infected cells as a 15-kDa protein. Expression of HBeAg is not required for the establishment of productive infection, but is thought to be involved in the transient suppression of the immune response[27].

Viral DNA is packed inside the capsid; the conformation of HBV genome is particular, with a full-length negative strand and a shorter positive strand. Because of its small dimension, the genomic information of HBV is packed in a complex way, with four promoters, two enhancer elements and a single polyadenylation signal to regulate transcription of viral RNAs.

The first step for the viral replicative cycle is the binding of the virus to the hepatocyte surface; recently it has been shown that the HBV surface protein are able to bind the sodium taurocholate co-transporting polypeptide (NTCP), mediating the viral entry[29].As soon as the virus enters the cell, the capsid migrates along the microtubules from the cytoplasm to the nucleus, in which genomic RC DNA is converted to covalently closed circular (CCC) DNA. The viral DNA remains into the nucleus, associated with histone proteins to form a mini chromosome, which can be used as a template for the viral

RNAs' transcription.

HBV genome encodes for three major transcripts, that derive from the minus strand, termed pre-C/C, pre-S and S mRNAs. Another transcript, named pregenome RNA or pgRNA, acts as an alternative template for the translation of the core and reverse transcriptase (RT) but is also the template for viral DNA synthesis via reverse transcription. To complete the replicative cycle, the virus itself carries the viral RT, which remains covalently linked to the 5' of the negative strand during the assembly phase. In the case of productive infection, capsid proteins can interact and bind envelope proteins along the membrane of multivescicular bodies, leading to the viral assembly; finally, complete HBV particles can bud passing through the endoplasmic reticulum and the Golgi complex. The virus is then release into the bloodstream, together with sub viral particles of 20-nm, that consist of HBV surface antigen (HBsAg) and host-derived lipids[30].

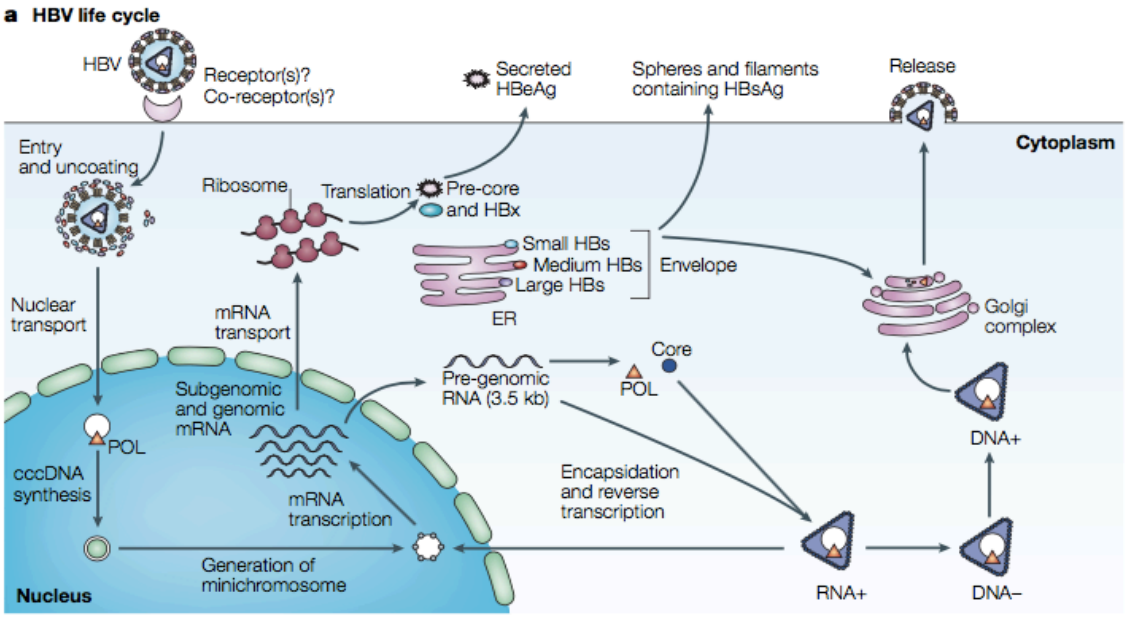

Figure 4. *HBV replicative cycle.*

HBV binds to the hepatocyte surface, then the capsid migrate to the nucleus, in which genomic RC DNA is converted to covalently closed circular (CCC) DNA.

Viral DNA is transcribed in mRNA that codifies both for structural proteins and for the pre-genome of the virus.

The pre-genome is encapsulated into HBV structural proteins, together with the viral RT, which remains covalently linked to the RNA during the assembly phase.

Complete HBV particles can bud from the cell passing through the endoplasmic reticulum and the Golgi complex. The virus is then release into the bloodstream, together with subviral particles.

Main routes of infection are the one that involve blood/fluid exposure: delivery from an infected mother, blood transfusion, intravenous drug use, sexual intercourse etc. In case of acute infection, viral DNA can be detectable within the first month of infection and its levels remain low up to six weeks. From a serological point of view, HBcAg-specific IgM are considered as a maker of early infection, while HBcAg-specific IgG can persist for life. An indirect marker of HBV infection is the level of serum alanine aminotransferase (sALT), that start to rise 10-15 weeks after the infection and is indicative of T-cell-mediated liver injury, since the virus is not cytopathogenic. Neonates, that generally do not exhibit a symptomatic acute hepatitis, are HBeAg seropositive, and present high viral loads but normal sALT levels and near-normal liver histology. Fulminant hepatitis is also a very rare event in pediatric patients, and its mostly reported in infants born from HBsAg-carrier mothers that show HBeAg-negativity. A possible explanation for this event is that the absence of the antigen during pregnancy could lead to a vigorous response against HBV in the infant liver. In contrast, presence of HBeAg in maternal blood during pregnancy is probably necessary for the induction of immunological tolerance in the fetus that promotes persistent infection in most neonates. The mechanism of this tolerance is still not well understood, but a plausible hypothesis is that the unresponsiveness of helper T cells to HBeAg, leads to an ineffective $CD8^+$ T-cell response in neonates[27] resulting in a in the development of chronic hepatitis. Moreover, high viral load seems necessary in order to maintain the tolerant state[31].

HBV infection during adulthood results in 95% of cases to viral clearance. Others 5% fail to clear the virus and develop chronic hepatitis.

HBV infection, replication and shedding are non-cytopathic events, however the strong immune response against the infected cells is responsible for liver damage.

Several components of the immune response are required to clear the infection. Usually, during a viral infection, the infected cells release pro-inflammatory cytokines, such as IFNα/β, that are important for the induction of the innate response. This kind of cytokines enhance the expression of the so called “inducible stimulated genes” (ISGs), involved in several antiviral processes that can limit the spread of the infection. Interestingly, the production of ISGs is strongly reduced during the first phases of HBV infection, maybe due to an inadequate activation of the innate response. This may be due

to the capacity of the HBV to hide from the immune system using different strategies: first, the virus confines the transcription of its genes inside the nucleus, then it uses the cell machinery to process viral mRNA with cap and polyadenylation signal (in order to mimic normal cellular transcripts), finally it protects its replicating DNA inside the capsid from recognition in the cytoplasm[32].

Humoral response against HBcAg, HBsAg and HBeAg can be efficiently evoked during HBV infection and this element can be used to discriminate different clinical profiles. The earliest marker of acute infection is the IgM response against HBcAg, whereas in the late phase is common to find antibodies specific for HBsAg and HBeAg. Neutralizing IgG response is developed in the late phase of the acute infection and can persist lifelong, giving protective immunity against the virus; IgG specific for HBsAg decline overtime, while HBcAg remains high and represents a solid marker for past exposure to the virus. Despite this, during chronic infection, anti-HBs Ab level is not easy to measure since the antibodies are usually bound with the antigen.

The action of T cells in the acute phase of HBV infection is crucial: patients who can spontaneously resolve the infection mount vigorous $CD4^+$ and $CD8^+$ T-cell responses, while patients with chronic hepatitis are characterized by transient or narrowly focused T-cell responses.

7. CHAPTER THREE

7.1. $CD8^+$ T cell response during HBV infection

HBV is a non-cytopathic virus causing acute and chronic necro-inflammatory liver diseases. The outcome of hepatitis B is variable and the host response to the virus is thought to be determinant in the pathogenesis of the infection[13]. Indeed, studies of HBV pathogenesis, both in humans and in animal models, suggest that viral hepatitis is initiated by an antigen-specific antiviral cellular immune response. The hypothesis of a participation of the T cell component in the response against HBV raised from the observation of acute and chronically infected patients: while in the acute hepatitis there is a strong multi-epitope-specific $CD4^+$ and $CD8^+$ T-cell response against infected cells, the response is weak or even absent in chronically infected patients[32]. In addition, studies on chimpanzees showed that viral clearance involves two distinct processes: a non-cytolytic action, that reduce the size of infection by eliminating the virus through the production of antiviral cytokines, such as IFNs[33] and a cytolytic CD8+T cell response against infected hepatocytes. This last point has been studied not only in chimpanzees but also on woodchucks and ducks (infected with the corresponding hepadnaviruses), therefore proving that cytolytic events are required for the complete elimination of HBV from hepatocytes[34]. In this line, the depletion of $CD8^+$ T cells in HBV infected chimpanzees delayed the onset of viral clearance and liver disease, thus supporting the important role of CD8+T cells on both the non-cytolytic control of HBV replication and the above mentioned cytolytic process that anticipate viral clearance[35]. On the other hand, HBV infected chimpanzees depleted of $CD4^+$ T cells at the peak of viremia are not affected neither on the time of recovery or on the level of liver damage. As described before, this result may suggest that CD4+ T cells are not directly involved in the clearance of the virus from infected cells, but they can instead indirectly induce and sustain an HBV-specific $CD8^+$ T cell response[32].

For decades, the main obstacle for the study of HBV infection has been the restricted host range. First attempts to study HBV immune response in mice were performed using chimeric mouse models in which mice were first irradiated and depleted

of their hepatocytes, to be further replaced by human ones. Because of the disruption of the basic liver anatomical structure and the loss of lymphocyte contribution, this model was useful for studying the innate cellular antiviral response but not suitable for adaptive immune response studies. With the advent of HBV-replication-competent transgenic mice, in which hepatocytes are able to produce the full virus or its structural proteins without evidence of cytopathology, it has been possible to overcome these limitations[36]. Indeed, first studies on Tg mice models, allow to demonstrate that, the peculiar anatomical structure of the liver permit the hepatic priming of naïve T cells as has been described in chapter one. Models of Ag-specific $CD8^+$ T cell adoptive transfer in mice that express HBcAg in the hepatocytes, showed that naïve T cells primed by hepatocytes were able to proliferate but did not acquire cytotoxic functions. On the contrary, when priming was driven by APCs in secondary lymphoid organs, $CD8^+$ T cells were able not only to proliferate, but they were also fully differentiated into effectors[37]. However, these studies were performed mostly on mice in which viral protein expression was induced using Vaccinia viral vectors carrying HBV genes; given the broad cellular tropism of the vector and the experimental setup that did not exclude secondary lymphoid organs for the priming of naïve T cells, the real contribution of the liver to the fate of primed naïve T cells remain uncertain.

7.2. Interleukin 2

IL-2 is a cytokine produced predominately by activated $CD8^+$ and $CD4^+$ T cells after the engagement of the TCR and costimulatory signals[38]. This cytokine acts as a potent mitogen and growth regulator of T cells, able to influence CTLs activity by inducing the expression of IFNγ, Tumor Necrosis Factor-α (TNFα), granzyme B and by regulating amino acid uptake and protein synthesis[39].

Due to its potent biological effect, IL-2 interaction with its receptors on $CD8^+$ T cell is strongly controlled. IL-2 receptors (IL-2R) are composed by three different subunits, the combination of which generates different receptors with different IL-2 affinity: IL-2 binds with low affinity the IL-2R formed only by the CD25 subunit; with intermediate affinity to dimeric receptors containing the CD122:CD132 subunits and with high affinity to trimeric receptors formed by the CD25:CD122:CD132 subunits[40].

Naïve $CD8^+$ T cells do not display CD25 at the cellular surface but only the intermediate affinity IL-2R form. However, following TCR engagement, CD25 is expressed and endows T cells to respond to IL-2 that is transiently available *in vivo*.

On the other hand, $CD4^+$ $FoxP3^+$ T regulatory cells (Treg), which constitutively express the high affinity form of IL-2R. For such reason, it has been proposed that Tregs act as a "sink", absorbing IL-2 from the local environment; this regulatory loop would deprive recently stimulated T cells from the IL-2 required to initiate proliferation and subsequent differentiation[41].

Despite the fact that IL-2R expression changes between different cellular population, the signal transduction triggered by IL-2 is conserved and relies on the cytoplasmic tails of CD122 and CD132 (note that CD25 subunits is not involved is signal transduction). Binding of IL-2 on the high affinity or intermediate affinity receptors leads to the activation of multiple signaling pathways, with the initial signaling transduction involving the recruitment of Janus family tyrosine kinases (JAK1 and JAK3) to the cytoplasmatic domains of the CD122 and CD132 subunits. The activation of JAK kinases ends in the recruitment and phosphorylation of various members of the signal transducer and activator of transcription family 5 (STAT5).

Once STAT5 is phosphorylated (pSTAT5), it translocates to the nucleus and promotes the transcriptions of genes involved with cellular survival, proliferation, differentiation, activation and cytokine production[42].

Since IL-2 signaling is required for optimal immune responses in vivo[42], IL-2 therapy has been used in clinic for more than three decades as cancer therapy and to a lesser extent in viral infection.

For cancer, IL-2 is an approved drug for treating melanoma and metastatic renal cell carcinoma, both as a monotherapy or combined with chemotherapeutic agents[42]. Nevertheless, it has to be considered that several aspects limit the use of this cytokine as an immunotherapy strategy. First, due to rapid elimination and metabolism via the kidney, IL-2 has a short plasmatic half-life (minutes)[43]. For this reason, to achieve an optimal immune-modulatory effect, IL-2 should be given to a high dose, which results in severe toxicities such as vascular leak syndrome (VLS), pulmonary edema, hypotension and cardiotoxicity. Moreover, the high expression of CD25 by Treg leads to a preferential binding of IL-2 on these cells, which may expand and eventually promote a general state of immunosuppression.

To overcome the aforementioned limitations, injection of IL-2 coupled with anti-IL-2 Abs (IL-2 complexes, i.e. “IL-2c”) was found to greatly increase the therapeutic potential of IL-2. In comparison to free IL-2, IL-2c possess indeed a higher half-life and, due to steric hindrance, circumvents the interaction with IL-2Rα (CD25) avoiding the Treg sinking[44]. IL-2 conjugated to the monoclonal antibody S4B6, which blocks the CD25 interaction domain of IL-2, preferentially binds to $CD8^+$ T cells with no expression of CD25 rather than to Treg. It is important to highlight that the biological activity of this complex was found to be independent from Fc receptors.

8. CHAPTER FOUR

8.1. Imaging methods to study the T cell migration

The extent of the T cell migration process *in-situ* became possible by the development of the microscopy and advances in genetically encoded fluorescent proteins. Moreover, inventive ideas from investigators to set up novel methods and surgeries allowed intravital imaging of a multitude of organs[45,46].

Imaging technologies

Observations of organ's sections or even intravital imaging were first performed using two-dimensional methods, such as bright field trans-illumination and epifluorescence video microscopy[47]. This first approaches helped, for example, to understand how leukocytes interact with endothelial cells. Afterwards, the development of the laser scanning confocal microscopy (LSCM), that eliminates the out-of-focus signals, allowed three-dimensional imaging and better optical resolution. This technique is now widely used and advances in the number of colors that can be detected, enabling the observation of T cell phenotype or sub-cellular events *in-situ*. Conversely, the LSCM is sequentially focusing on a region of interest of the specimen; due to the precise control of galvanometer mirrors, the acquisition may be too slow for the observation of a dynamic specimen. For a typical imaging scenario, an LSCM scan at a speed of 1μm/pixel, which means the acquisition of a generalized 512x512 pixel array takes 0.26 second. Therefore, this time "skew" between the first and the last pixel can generate errors in the observation. In addition, for a multicolor imaging, the time skew is repeated for each laser. To circumvent this limitation, the upgrade of the system by a spinning disk allows the excitation, as well as the light detection, at multiple points simultaneously[48]. The high-speed acquisition of a spinning disk confocal microscope offers the possibility to acquire very large area of a specimen.

For example, such microscopy setting is very well suited to observe fast-moving parasites in the vast liver parenchyma *in-vivo*[49]. In this case, the liver parenchyma is readily accessible (80µm of depth); however, the detection of biological processes happening deeper in the tissue (>100µm) or the structure of the tissue itself (for example the presence of a collagen capsule), render the use of a confocal microscope impossible in a lot of cases.

The development of the two-photon microscopy technique a decade ago allowed the imaging of very deep section in the tissue (~400µm) thus favoring the first understandings on immune cell dynamics[45]. This technology uses long wavelength (infrared range, >690nm) that can penetrate deeper in the tissue compared to the ones used for conventional microscope (400-600nm).

The principle of two-photon microscopy relies on the excitation of fluorophores by two infrared photons that hit the molecule in a short window time. The excitation with one infrared photon indeed is not energetic enough to excite most of the fluorophores commonly used for immunofluorescence. However, the use of a pulsed laser capable of producing a high photon density, allows to excite the specimen with two photons simultaneously and correctly excite the fluorophores.

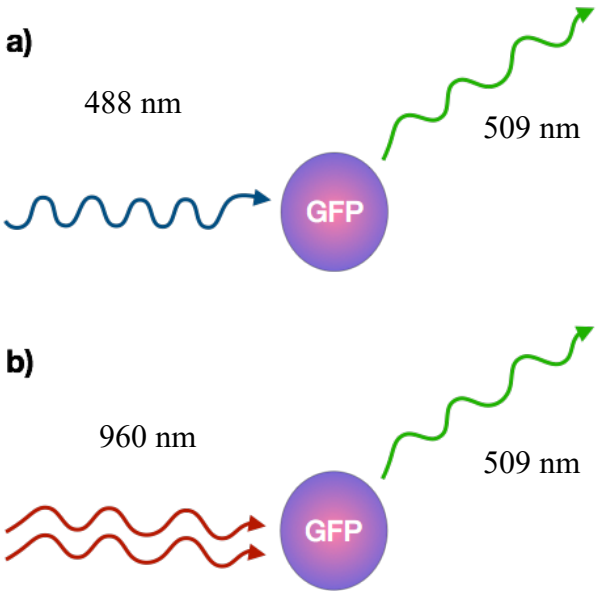

Figure 5. *Single-photon absorption (a) versus two-photon absorption (b) of a green fluorescent protein (GFP) molecule.*
Visible light is used for excitation in single-photon microscopy, whereas near-infrared light is used in two-photon microscopy, obtaining the same wavelength emission[104].

Moreover, the near simultaneous interactions of two photons together are only possible at the focal plan, thereby providing an inherent pinhole and limiting the photo-damage out of the focus. Therefore, the multi-photon microscopy, offering depth and limiting bleaching, became the method of choice for dynamic imaging.

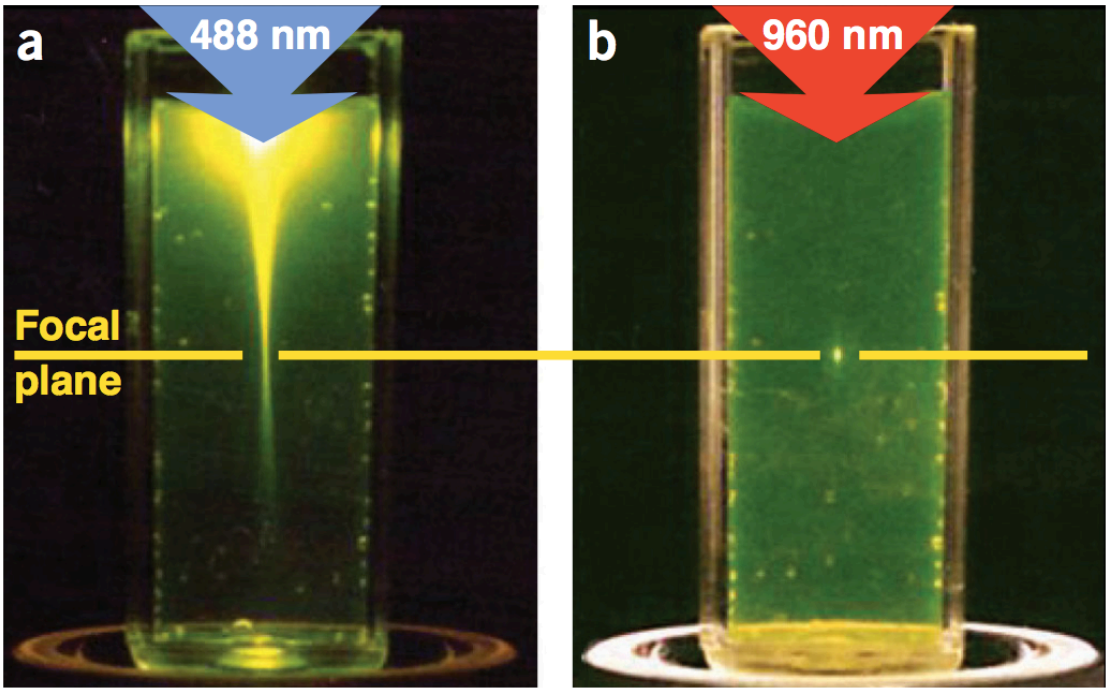

Figure 6. *Localization of two-photon excitation.*

(a) *Single-photon excitation of fluorescein by focused 488-nm light.*

(b) *Two-photon excitation using focused (0.16 NA) femtosecond pulses of 960-nm light*[105].

Surgical techniques to study T cell dynamic in-situ

The growth in dynamic immuno-imaging has been fueled by pivotal studies starting in 2002, describing the T cell dynamic in the LN and the thymic microenvironment[45]. Since then, a lot of groups developed their own system and surgical techniques to image T cell dynamics in a multitude of organs. One example of this technological development is the explant chamber a setup that has been used for several organs[50,51,52]. It consists of a flexible system to image cell dynamics directly in the organ microanatomy that must be maintained perfused with oxygenated and kept at the 37°C. All of this and offers high stability during image acquisition. Another advantage of this system is the possibility to image vibratome-thick organ' sections, enabling its use *ex vivo*[53], as well as the significant possibility to visualize cell dynamic in a viable human organ[54]. Although such *ex-vivo* system likely reproduces the T cell locomotion that can be seen *in-vivo*, for example, in a LN cortex, it is important to keep in mind that organ excision can affect the chemokine distribution.

This system suits better for sealed organs such as LN cortex, however it fails to reproduce the environment of vascularized organs, such as the liver or the lung, where the forces induced by the fluid circulation is a determining factor of the cell migration. For this reason, when it is technically feasible, intravital microscopy is the preferred technique to analyze the cell dynamic in these highly vascularized organs.

In 2002, investigators developed custom-built stages that allowed the immobilization of organs in a living mouse[55]. While the skin draining LN is relatively easy to expose and requires only a minimal incision of the skin[56], others organs that locate deeper in the mouse body necessitates the design of technically demanding procedures. For instance, our group has designed a specific surgical procedure in order to expose the liver without perturbation of the blood circulation[57].

9. AIM OF THE WORK

$CD8^+$ T cells play critical roles in immune defence against infections and tumours that affect the liver. The protective capacity of these cells is mediated by antigen (Ag)-experienced effector cells and depends on their ability to migrate and traffic within the liver, recognizing pathogen and/or tumor-derived antigens, get activated and deploy effector functions. While some of the rules that characterize hepatic $CD8^+$ T cell behaviour have been studied at the population level, we have only limited knowledge on the precise dynamics whereby $CD8^+$ T cells migrate, activate, and carry out their effector functions at the single-cell level and many questions remain to be clarified: what are the spatial and temporal character of such interactions? What are the molecular mechanisms that regulate $CD8^+$ T cell communication with liver cells? How does interactive behaviour influence immunological outcome? What are the mechanisms that drives the immunostimulant or immunosuppressive capacity of liver environment? Are there treatments that could drive an immunostimulant state of the liver? What are the cell targets of those treatments? During this project we have address these questions to better understand the functional consequences of hepatic priming of naïve $CD8^+$ T cells in the context of chronic HBV infections.

10. RESULTS

The following data have been published (*Bénéchet, De Simone et al. Nature 2019; De Simone et al. Immunity 2021*).

10.1. Spatiotemporal dynamics of naïve CD8+ T cells undergoing intrahepatic priming

The first set of experiment that we carried out had the scope of unveiling the early dynamics of naïve T cell response in the liver, to have a better understanding of the potential outcomes of T cell response in the context of HBV infection.

Adult immune competent individuals are able to mount an effective $CD8^+$ immune response against HBV[58]. In contrast, experiments performed in mouse models showed that, when naïve $CD8^+$ T cell with a transgenic TCR specific for an immunodominant peptide of the HBeAg (Env28 T_N cells)[37] are adoptively transfer to a transgenic mouse expressing HBV viral proteins on hepatocytes[59], CD8+T cells expand, but they are not able to differentiate in effectors cells endowed with cytotoxic or antiviral potential (Fig.7). These contradictory results make us think that the outcomes observed could be due to i) the cross-priming of cells in secondary lymphoid organs or ii) the liver is able to support naïve $CD8^+$ T cell priming and differentiation. To clarify these questions, we setup an experimental system to investigate naïve $CD8^+$ T cell intrahepatic priming in a non-inflamed liver. To this end, we took advantage of a well characterized experimental model where specific HBV core CD8+T cells (Cor93 T cells)[37] are transferred to a recipient mouse in which 100% of hepatocytes express a non secretable form of the HBV core antigen under the Major Urinary Protein promoter (known as MUP-core mouse)[60]. This system enables $CD8^+$T cell priming exclusively by hepatocytes (Fig.8 E).

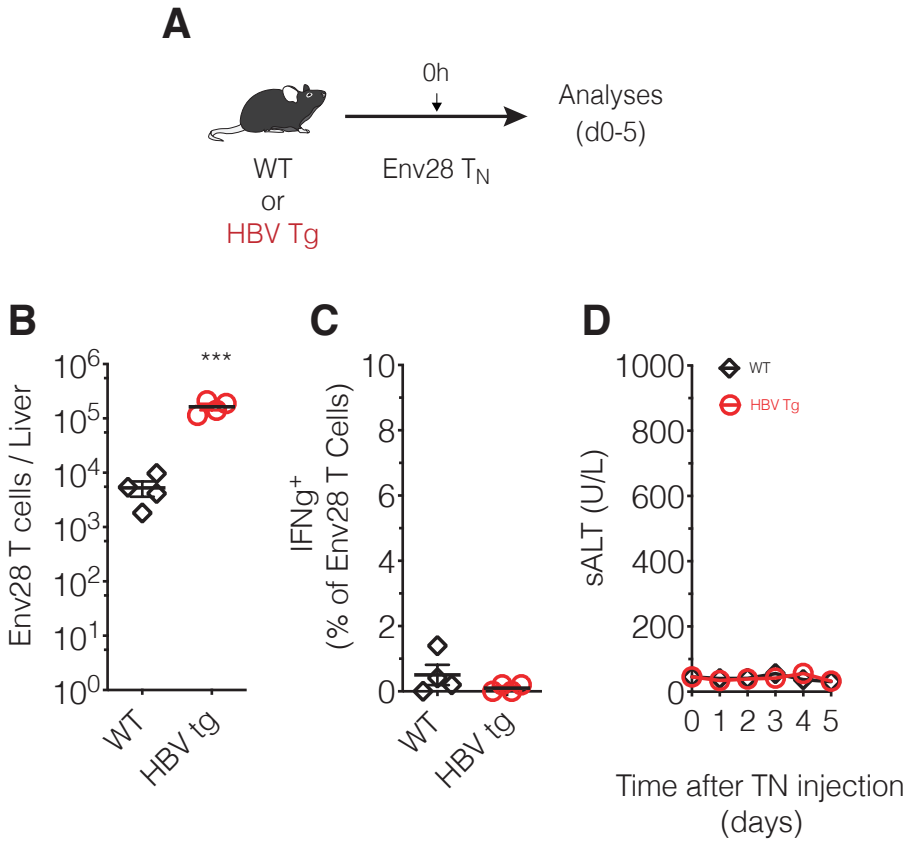

Figure 7. *Naïve CD8$^+$ T cells that recognize hepatocellular Ag are activated and expand but fail to develop effector function.*

*(**A**) Schematic representation of the experimental setup. 5 x 10^6 Env28 T_N were transferred into C57BL/6 x Balb/c F1 (WT) or HBV replication-competent transgenic (HBV Tg, C57BL/6 x Balb/c F1) recipients. Livers were collected and analysed five days after Env28 T_N transfer and sera from the same mice were collected every day from day 0 to day 5 after Env28 T_N transfer. (**B-C**) Absolute numbers (**B**) and frequency of IFNγ-producing (**C**) Env28 T cells in the livers of the indicated mice. (**D**) ALT levels detected in the sera of the indicated mice at the indicated time points. n = 4. Results are expressed as mean ± SEM. Means among groups were compared with two-tailed t test. Data are representative of at least 3 independent experiments. *** p value < 0.001. (Bénéchet, De Simone et al. Nature 2019).*

To avoid T cell recruitment to lymph via high endothelial venules, we threated the recipient mice with anti CD62L blocking antibody and surgically removed the spleen of the mice two days before the $CD8^+$T cell transferring. As controls groups we used: i) WT C57BL/6 mice ii) WT C57BL/6 mice injected with a recombinant replication defective LCMV-based viral vector (rLCMV-core) which can transduce a non secretable form of HBcAg to liver APCs (mostly KCs and DCs), that are not the natural target of HBV (Fig. 8 E).

As illustrated in Fig.8 F, the results showed that the naïve $CD8^+$ T cell priming is restricted to the liver, as we found the early activation marker CD69 upregulated on Cor93 T_N as early as 1h after transfer; moreover, CD69 was exclusively upregulated on intrahepatic Cor93 T_N cells and not on cells isolated from other organs.

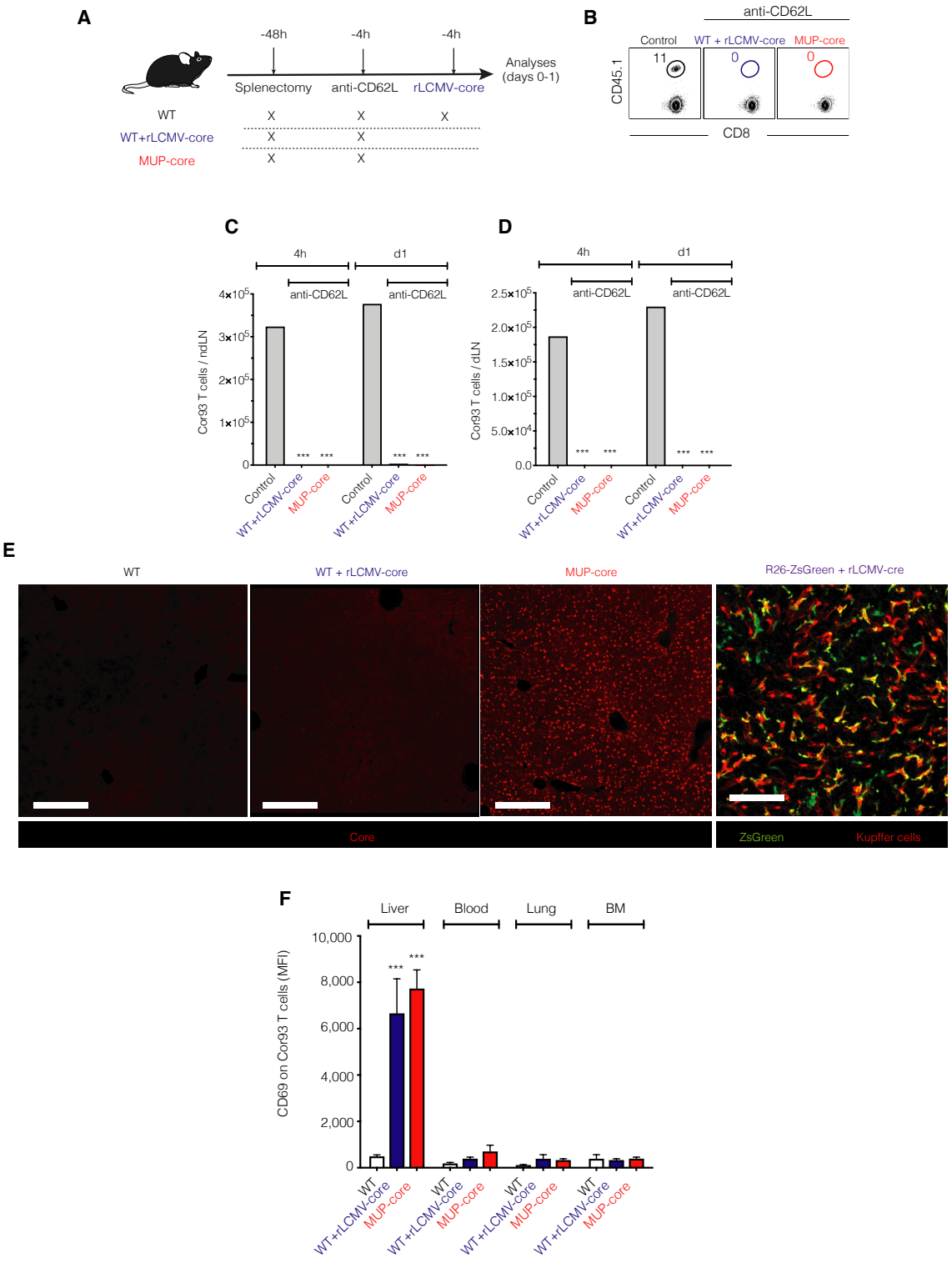
A
-48h
-4h
-4h
Splenectomy
anti-CD62L
rLCMV-core
Analyses
(days 0-1)
WT
WT+rLCMV-core
MUP-core
B
anti-CD62L
Control
WT + rLCMV-core
MUP-core
CD45.1
CD8
C
4h
d1
anti-CD62L
Cor93 T cells / ndLN
Control
WT+rLCMV-core
MUP-core
D
Cor93 T cells / dLN
E
WT
WT + rLCMV-core
MUP-core
R26-ZsGreen + rLCMV-cre
Core
ZsGreen
Kupffer cells
F
Liver
Blood
Lung
BM
CD69 on Cor93 T cells (MFI)

Figure 8. *Naïve $CD8^+$ T cells that recognize hepatocellular Ag are activated and expand locally.*

*(**A**) Schematic representation of the experimental setup. 5 x 10^6 Cor93 T_N were transferred into C57BL/6 (WT) or MUP-core recipients. Mice were splenectomized and treated with anti-CD62L 48 hours and 4 hours prior to cell transfer, respectively. Untreated WT mice that received 5 x 10^6 Cor93 T_N were used as controls. Where indicated, mice were injected with 2.5 x 10^5 infectious units of non-replicating rLCMV-core 4 hours prior to Cor93 T_N transfer. Liver-draining lymph nodes (dLN) and non-draining inguinal lymph nodes (ndLN) were collected at four hours and one day after Cor93 T_N. (**B**) Representative flow cytometry plot at four hours upon Cor93 T_N transfer. Numbers indicate the percentage of cells within the indicated gate. (**C-D**) Quantification of the absolute numbers of cells recovered from the ndLN (**C**) and dLN (**D**) of the indicated mice four hours and one day upon Cor93 T_N transfer. n = 3. Results are expressed as mean ± SEM. Means among groups were compared with one-way ANOVA with Bonferroni post-test. (**E**) Confocal immunofluorescence micrographs of liver sections from WT mice (WT), rLCMV-core-injected WT mice (WT + rLCMV-core), MUP-core mice and R26-ZsGreen mice injected with 2.5 x 10^5 infectious units of non-replicating rLCMV-cre (R26-ZsGreen + rLCMV-cre). Scale bars represent 100 mm. Note that, because HBV core protein did not accumulate at detectable levels in KCs and hepatic dendritic cells [DCs] upon rLCMV-core injection, we confirmed the tropism of this vector by injecting rLCMV-cre into R26-ZsGreen mice – these mice express the fluorescent protein ZsGreen upon Cre-mediated recombination. (**F**) Mean Fluorescent Intensity (MFI) of CD69 expression on Cor93 T cells in the liver, blood, lung, and bone marrow of the indicated mice four hours after Cor93 T_N transfer. n = 4. Results are expressed as mean ± SEM. Means among groups were compared with one-way ANOVA with Bonferroni post-test.*
*Data are representative of at least 3 independent experiments. *** p value < 0.001**. (Bénéchet, De Simone et al. Nature 2019).*

We then characterized the fate and functions of transferred Cor93 T_N in the different setups. We observed that Cor93 T_N recognizing the antigen in the liver were not only able to be primed intrahepatically, but they also underwent local activation and proliferation, since we were able to recover up to 30-fold more cells in the liver of antigen bearing mice respect to liver of the control C57BL/6 mice (Fig. 9 B).

The model and control we used, however, are relying on two different cell populations for T cell priming (as previously stated): on one hand, the antigen in MUP-core mice is presented by hepatocytes, while on the other hand the same antigen in WT transduced with rLCMV-core is presented by APCs.

Even though the antigen presented to Cor93 T_N was the same, we observed two different outcomes after T cell priming.

Indeed, whereas the antigen recognition on KCs and liver DCs was leading to $CD8^+$ T cell effector differentiation (with cells producing IFNγ and cytotoxic cytokines), the recognition of the antigen on hepatocytes lead to the differentiation of dysfunctional $CD8^+$ T cells. Those cells were not only producing little or no IFNγ after in vitro peptide re-stimulation, but they did not develop cytotoxic activity either, instead upregulating inhibitory receptors such as PD-1, as shown in Fig.9 C-D.

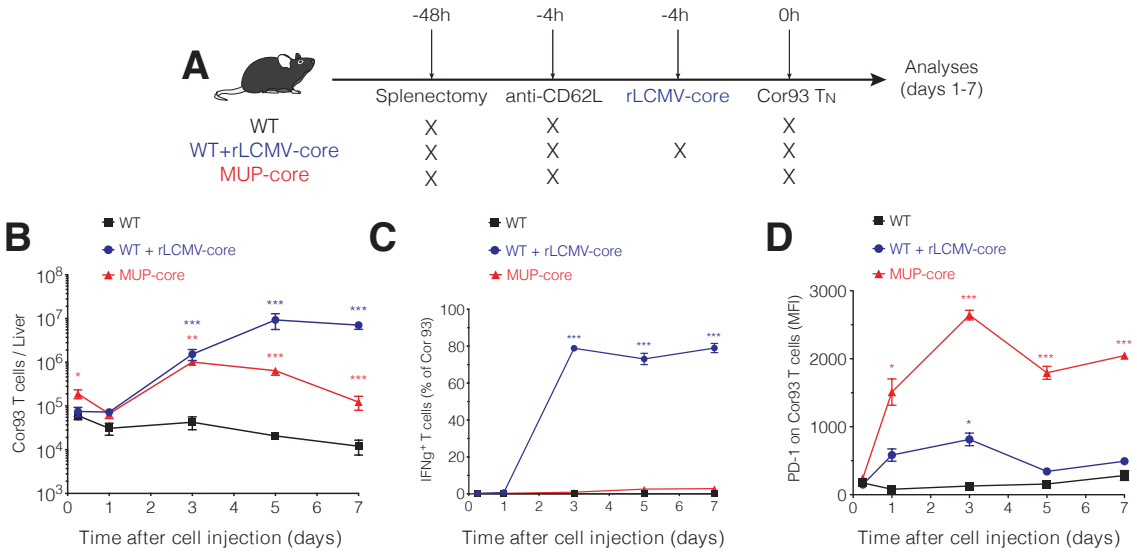

Figure 9. *Spatiotemporal dynamics of naïve CD8$^+$ T cells undergoing intrahepatic priming.*

*(**A**) Schematic representation of the experimental setup. (**B**) Absolute numbers of Cor93 T cells in the livers of indicated mice at indicated time points. (**C**) Frequency of IFN-□-producing Cor93 T cells in the livers of indicated mice at indicated time points. (**D**) MFI of PD-1 expression on Cor93 T cells in the livers of indicated mice. Results are expressed as mean ± SEM. Data are representative of at least 3 independent experiments. * p value < 0.05; ** p value < 0.01; *** p value < 0.001. (Bénéchet, De Simone et al. Nature 2019).*

Together, these results indicate that the liver can support the development of either functional or dysfunctional $CD8^+$ T cells and this phenomenon is depending on the nature of the cell that is presenting the antigens.

To have a better idea of the behavior of T_N and understand what the differences of the intrahepatic priming in the two experimental models are then analyzed the spatiotemporal dynamics of transferred cells.

We observed that effector cells in the liver of mice transduced with rLCMVcore formed clusters scattered throughout the liver lobule in a pattern like the one observed during acute HBV infection.

On the other hand, $CD8^+$ T cells formed clusters confined to the portal tracts in MUP-core mice (despite the antigen being expressed by 100% of hepatocytes in the parenchyma), resembling what it was observed during chronic HBV (Fig. 10).

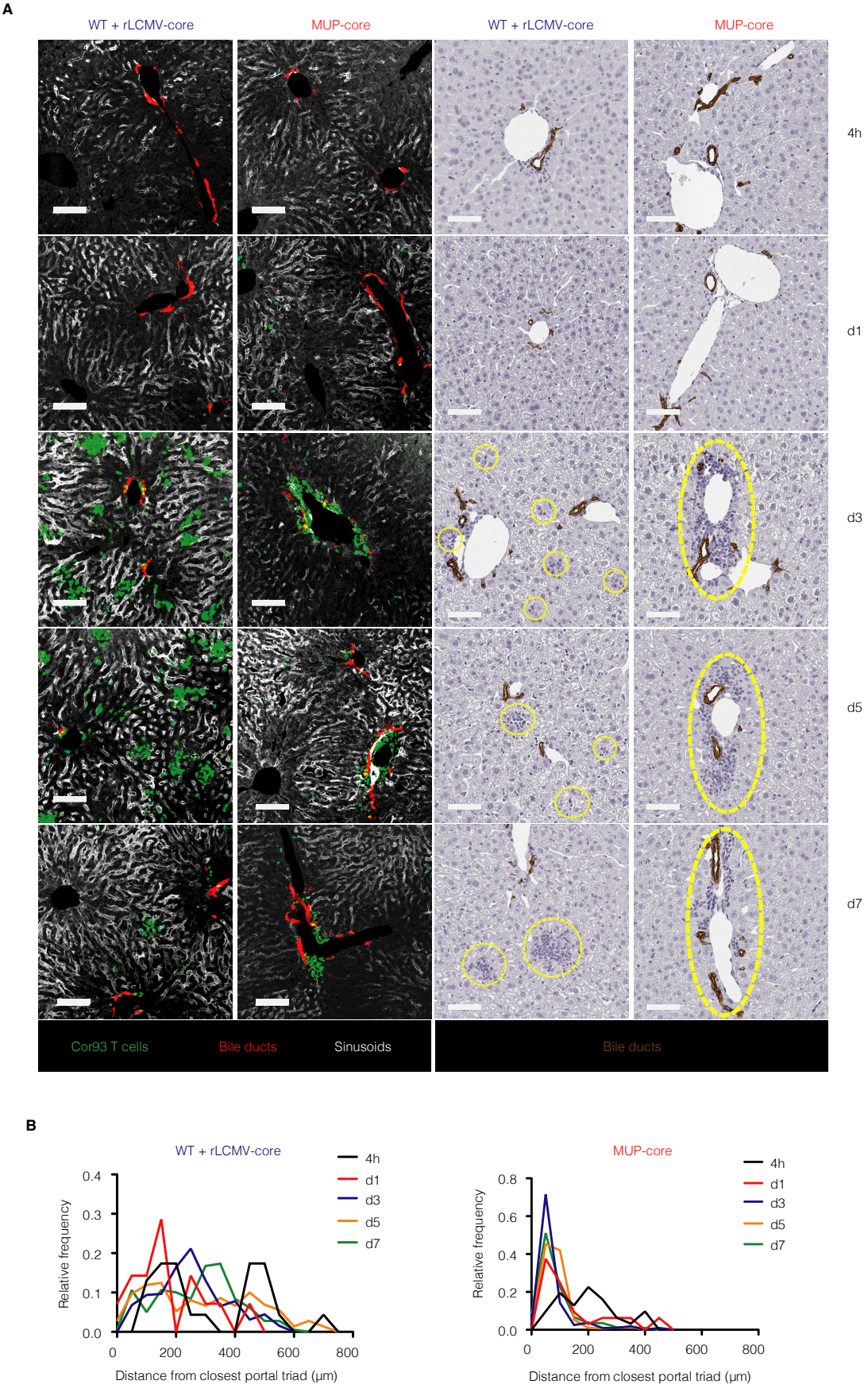
A
WT + rLCMV-core
MUP-core
WT + rLCMV-core
MUP-core
4h
d1
d3
d5
d7
Cor93 T cells
Bile ducts
Sinusoids
Bile ducts
B
WT + rLCMV-core
MUP-core
4h
d1
d3
d5
d7
Relative frequency
0.0
0.1
0.2
0.3
0.4
0.6
0.8
0
200
400
600
800
Distance from closest portal triad (μm)

Figure 10. *Spatiotemporal dynamics of naïve $CD8^+$ T cells upon intrahepatic priming. (I)*

*5 x 10^6 fluorescent Cor93 T_N were transferred into MUP-core or rLCMV-core-injected WT recipients. Mice were splenectomized and treated with anti-CD62L 48 hours and 4 hours prior to Cor93 T_N transfer, respectively. (*A*) (left panels) Confocal immunofluorescence micrographs of liver sections from the indicated mice at the indicated timepoints upon Cor93 T_N transfer, showing the distribution of Cor93 T cells (green) relative to portal tracts (highlighted by anti-cytokeratin 7 Ab-mediated staining of bile ducts in red). Sinusoids are highlighted by anti-Lyve-1^+ Abs (white). Scale bars represent 100 μm. (right panels) Immunohistochemical micrographs of liver sections from the indicated mice at the indicated timepoints upon Cor93 T_N transfer, showing the distribution of leukocyte infiltrates relative to portal tracts (highlighted by anti-cytokeratin 7 Ab-mediated staining of bile ducts in brown). Scale bars represent 100 μm. (*B*) Distribution of the distances (μm) of each Cor93 T cell from the center of the closest portal triad at the indicated timepoints. n = 3 mice. Data are representative of at least 3 independent experiments. (Bénéchet, De Simone et al. Nature 2019).*

Taking advantage of multiphoton intravital imaging, we observed that cells wild-type mice transduced with rLCMV-core form dense clusters of cells that moved at low speed. Interestingly, cells accumulated in the parenchyma outside blood vessels since the clusters were not perfused by sinusoidal blood. On the other hand, cells in MUP-core mice formed cluster of cells at higher speed, that tended to aggregate loosely around the portal tract (Fig. 11 B).

After five days post transfer, cells in wild-type mice transduced with rLCMV-core start to separate from the clusters and leave from the liver circulation, while periportal clusters in MUP-core mice remain stable, possibly reflecting antigen persistence (Fig. 11 A).

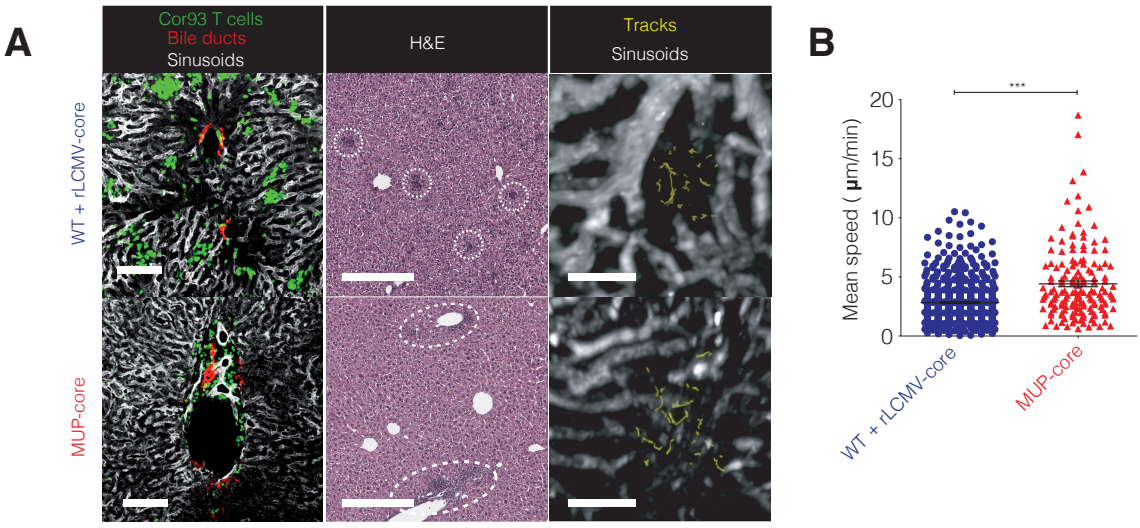

Figure 11. *Spatiotemporal dynamics of naïve CD8$^+$ T cells undergoing intrahepatic priming. (II)*

*(**A**) (Left panels) Representative confocal immunofluorescence micrographs of liver sections from WT + rLCMV-core (upper panels) or from MUP-core mice (lower panels) three days after Cor93 TN transfer. Distribution of Cor93 T cells (green) relative to portal tracts (red). Sinusoids are in white. Scale bars represent 100 μm. (Middle panels) H&E staining of liver sections from the same mice, where dotted lines denote leukocyte clusters. Scale bars represent 300 μm. (Right panels) Snapshots from representative intravital multiphoton microscopy movies of the same mice. Cor93 T cells tracks are in yellow and blood vessels are in white. Scale bars represent 40 μm. (**B**) Mean speed of Cor93 T cells in the livers of indicated mice. (Bénéchet, De Simone et al. Nature 2019).*

Since the tropism of the rLCMV vector is directed both on KCs and hepatic DCs, we decided to investigate which of this cell subset is responsible of supporting intrahepatic priming. Thus, we depleted KCs by injection of clodronate liposomes (CLL) into wild-type mice before transducing them with rLCMV-core viral vector. To note, clodronate injection is targeting exclusively phagocytes while sparing DCs[61] (Fig. 12 A-C).

We observed that in absence of liver macrophages (including KCs) T_N cell were not able to expand and differentiate into effector T cells (Fig. 12 D-F). On the other hand, when we depleted hepatic DCs by injection of diphtheria toxin in wild-type mice reconstituted with CD11c-DTR bone marrow, both the expansion and the effector differentiation of Cor93-specific $CD8^+$ T cells were only slightly affected (Fig. 12 G-K).

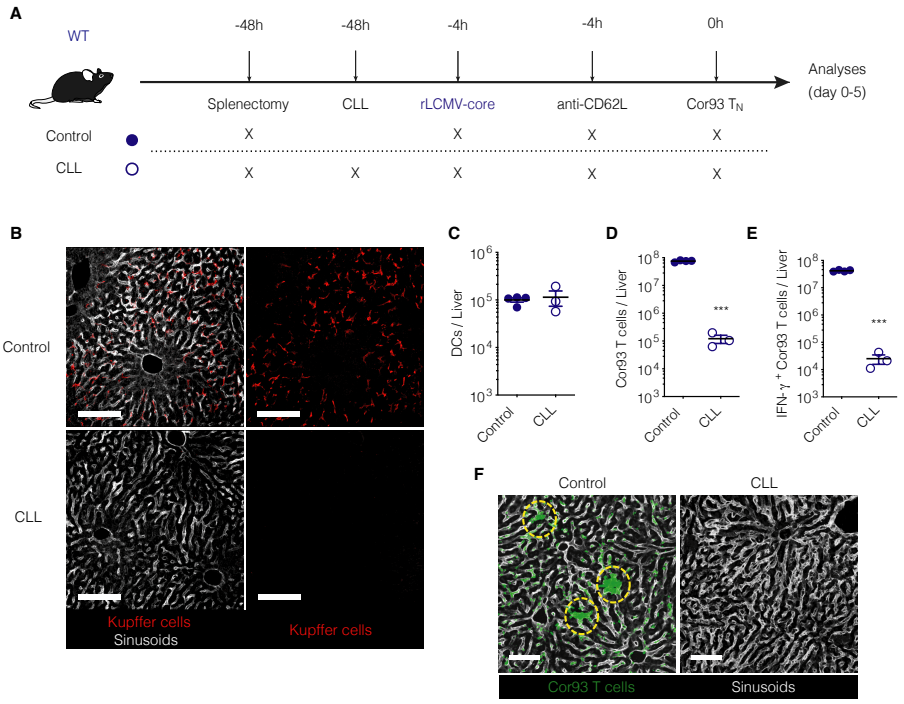
A
WT
-48h
-48h
-4h
-4h
0h
Analyses
(day 0-5)
Splenectomy
CLL
rLCMV-core
anti-CD62L
Cor93 T_N
Control
CLL
B
Control
CLL
Kupffer cells
Sinusoids
Kupffer cells
C
DCs / Liver
Control
CLL
D
Cor93 T cells / Liver
***
Control
CLL
E
IFN-γ+ Cor93 T cells / Liver
***
Control
CLL
F
Control
CLL
Cor93 T cells
Sinusoids

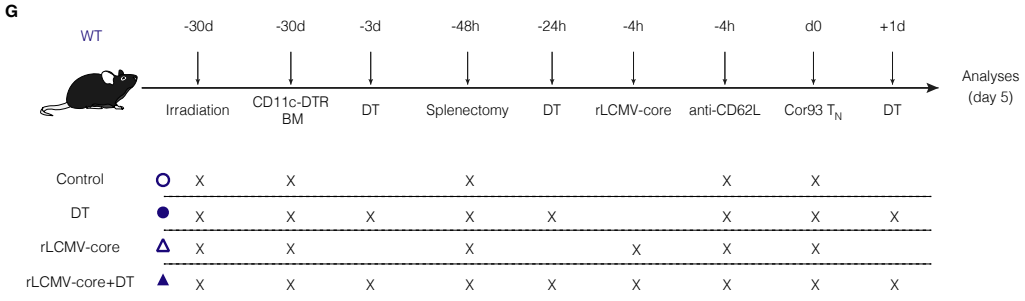
G
WT
-30d
-30d
-3d
-48h
-24h
-4h
-4h
d0
+1d
Analyses
(day 5)
Irradiation
CD11c-DTR BM
DT
Splenectomy
DT
rLCMV-core
anti-CD62L
Cor93 T_N
DT
Control
DT
rLCMV-core
rLCMV-core+DT

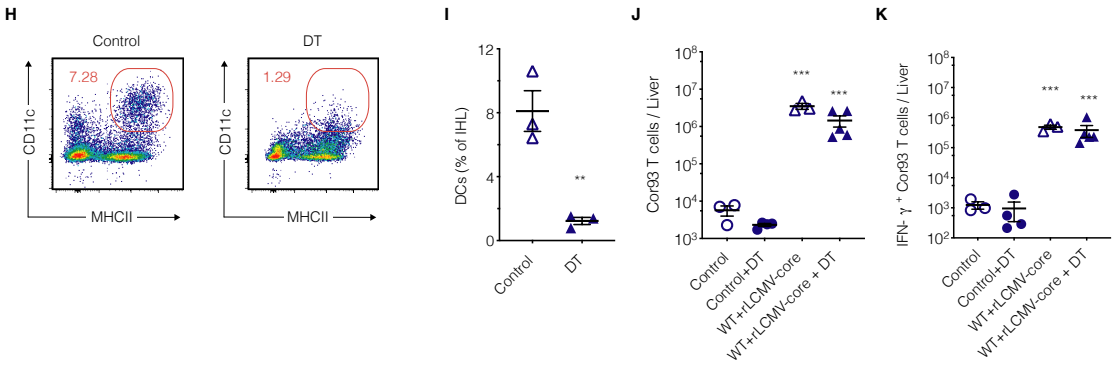
H
Control
DT
7.28
1.29
CD11c
MHCII
I
DCs (% of IHL)
**
Control
DT
J
Cor93 T cells / Liver
***
***
Control
Control+DT
WT+rLCMV-core
WT+rLCMV-core + DT
K
IFN- γ+ Cor93 T cells / Liver
***
***
Control
Control+DT
WT+rLCMV-core
WT+rLCMV-core + DT

Figure 12. *Kupffer cells, but not dendritic cells, promote $CD8^+$ T cell effector differentiation upon rLCMV injection.*

*(**A**) Schematic representation of the experimental setup. 5 x 10^6 Cor93 T_N were transferred into C57BL/6 (WT) recipients. Mice were splenectomized and treated with anti-CD62L 48 hours and 4 hours prior to cell transfer, respectively and injected with 2.5 x 10^5 infectious units of non-replicating rLCMV-core 4 hours prior to Cor93 T_N transfer. Where indicated, mice were treated with clodronate liposomes (CLL) 48 hours prior to Cor93 T_N transfer. (**B**) Confocal microscopy of liver sections from control mice (left panels) and clodronate liposomes-treated mice (right panels). Kupffer cells are depicted in red in all panels, while sinusoids are depicted in grey only in the first and third panel. Scale bars represent 100 μm. (**C**) Absolute numbers of $CD11c^+$ MHC-II^{high} dendritic cells (DCs) in the livers of the indicated mice. (**D**-**E**) Absolute numbers of total (d) and of IFN-γ producing (**E**) Cor93 T cells in the livers of the indicated mice five days after Cor93 T_N transfer. n = 4 (Control), 3 (CLL). Results are expressed as mean ± SEM. Means among groups were compared with two-tailed t test. (**F**) Confocal immunofluorescence micrographs of liver sections from the indicated mice five days after Cor93 TN transfer. Scale bars represent 100 μm. (**G**) Schematic representation of the experimental setup. WT mice were lethally irradiated and reconstituted with CD11c-DTR bone marrow (BM). 1 x 10^6 Cor93 T_N were transferred into recipients. Mice were injected with 2.5 x 10^5 infectious units of non-replicating rLCMV-core 4 hours prior to Cor93 T_N transfer. Indicated mice were treated with 400 ng of diphtheria toxin three days before, one day before and one day after T cell transfer. Livers were collected and analyzed five days after Cor93 T_N transfer. (**H**) Representative flow cytometry plots in the liver of control (left) or DT-treated (right) mice. (**I**) $CD11c^+$ $MHC\text{-}II^+$ DCs (expressed as percentage of the total intrahepatic leukocyte population, IHL) in the livers of the indicated mice. n = 3. Results are expressed as mean ± SEM. Means among groups were compared with two-tailed t test. (**J**-**K**) Absolute numbers of total (**J**) and of IFN- γ-producing (**K**) Cor93 T cells in the livers of the indicated mice five days after Cor93 T_N transfer. n = 3 (Control and WT + rLCMV-core), 4 (Control + DT), 5 (WT + rLCMV-core + DT). Results are expressed as mean ± SEM. Means among groups were compared with one-way ANOVA with Bonferroni post-test. Data are representative of 3 independent experiments. ** p value < 0.01, *** p value < 0.001. (Bénéchet, De Simone et al. Nature 2019).*

Together, these data suggest that KCs, but not hepatic DCs, are required for naïve $CD8^+$ T cell priming in the liver upon rLCMV injection.

High levels of antigen expressed by hepatocytes in MUP-core mice might trigger a dysfunctional T cell differentiation due to a continuous stimulation, therefore, to test this hypothesis, we decided to evaluate the fate of Cor93 T_N priming in a liver with low antigen level. First, we inject WT mice with a low dose of a hepatotropic adeno-associated viral vector (AAV) encoding the HBV core protein together with a GFP reporter protein (the same protein expressed by MUP-core hepatocytes), then we transferred Cor93 T_N cells. The dose we choose can transduce less than 5% of hepatocytes, as shown in Fig. 13 B. We observed that even in the presence of low antigen levels Cor93 $CD8^+$ T cell can proliferate still do not differentiated into effector cells, indicating that the constant stimulation by 100% of hepatocytes in MUP-core mice did not cause the dysfunctional phenotype of primed T cells (Fig. 13 C-E).

To further confirm these results, we perform the experiments in young MUP-core mouse hepatocyte (3–4-week-old). Core protein expression is developmentally regulated therefore 3-4 week old mouse express fewer amounts of antigen per hepatocyte compared to adult mice (around 15-fold less), in which antigen expression reaches its maximum level.[60] The results (Fig.13 J-L) supports the previous experiments: reduced amount of antigen per hepatocyte did not result in effector differentiation of hepatically primed $CD8^+$ T cells. Together, these experiments indicate that low expression of hepatocellular core antigen is *per se* not sufficient to induce effector differentiation.

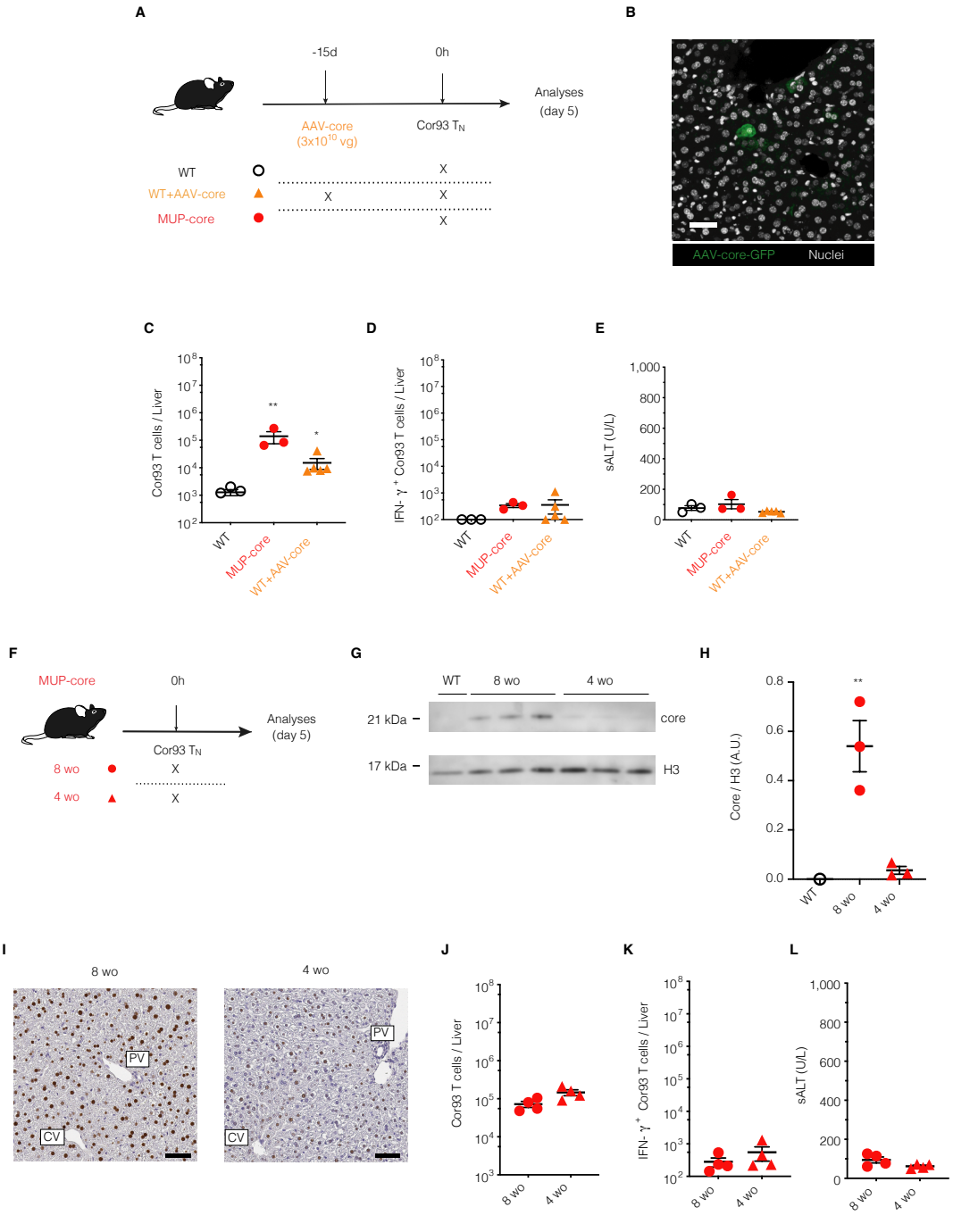
A
-15d
0h
Analyses
(day 5)
AAV-core
(3x10^10 vg)
Cor93 T_N
WT
WT+AAV-core
MUP-core
X
B
AAV-core-GFP
Nuclei
C
Cor93 T cells / Liver
WT
MUP-core
WT+AAV-core
D
IFN- γ + Cor93 T cells / Liver
E
sALT (U/L)
F
MUP-core
0h
Analyses
(day 5)
Cor93 T_N
8 wo
4 wo
G
WT
8 wo
4 wo
21 kDa
core
17 kDa
H3
H
Core / H3 (A.U.)
I
8 wo
4 wo
PV
CV
J
K
L

***Figure 13**. A strong reduction in the levels of hepatocellular core Ag expression is per se not sufficient to induce effector differentiation.*

*(**A**) Schematic representation of the experimental setup. 1 x 10^6 Cor93 T_N were transferred into C57BL/6 (WT) or MUP-core recipients. Indicated WT mice were injected with 3 x 10^{10} viral genomes of AAV-core 15 days prior to Cor93 T_N transfer. Livers were collected and analyzed five days after Cor93 T_N transfer. (**B**) Representative confocal immunofluorescence micrographs of a liver section from an AAV-core injected mouse 15 days after virus injection. Transduced hepatocytes are depicted in green and nuclei in grey. Scale bar represents 50 μm. n = 3 mice. (**C-E**) Absolute numbers of total (**C**) and of IFN-γ-producing (**D**) Cor93 T cells in the livers of the indicated mice five days after Cor93 T_N transfer. (**E**) ALT levels detected in the sera of the indicated mice. n = 3 (WT and MUP-core), 5 (AAV-core). Results are expressed as mean ± SEM. Means among groups were compared with one-way ANOVA with Bonferroni post-test. (**F**) Schematic representation of the experimental setup. 1 x 10^6 Cor93 T_N were transferred into 8-week-old (8 wo) or 4-week-old (4 wo) MUP-core mice. Livers were collected and analyzed five days after Cor93 TN transfer. (**G**) HBcAg expression in the livers of the indicated mice was analyzed by Western Blotting (WB). (**H**) Quantification of the WB shown in C. Core expression, normalized to the housekeeping nuclear protein H3, is expressed as arbitrary units (A.U.). n=1 (WT), 3 (MUP-core 8wo and MUP-core 4wo). Results are expressed as mean ± SEM. Means among groups were compared with two-tailed t test. (**I**) Immunohistochemical micrographs of liver sections from the indicated mice, showing core Ag expression (brown). Scale bars represent 50 μm. PV, portal vein, CV, central vein. n = 3 mice. (**J-K**) Absolute numbers of total (**J**) and of IFN- γ -producing (**K**) Cor93 T cells in the livers of the indicated mice five days after Cor93 TN transfer. n = 4. Results are expressed as mean ± SEM. Means among groups were compared with two-tailed t test. (**L**) ALT levels detected in the sera of the indicated mice. n = 4. Results are expressed as mean ± SEM. Means among groups were compared with two-tailed t test.*

*Data are representative of 2 independent experiments. * p value < 0.05, ** p value < 0.01. (Bénéchet, De Simone et al. Nature 2019).*

Finally, to evaluate the contribution of hepatocyte priming in a context in which the antigen is present on both hepatic cells as well as DCs and KCs, we co-transferred Env28 and Cor93 T_N cells in WT and MUP-core mice transduced with rLCMV vectors that encode either the HBV envelope protein (rLCMV-env) or both the HBV core and envelope proteins (rLCMV-core/env).

As expected, antigen-specific T_N cells expanded and differentiated into effector T cells only when cognate antigen was present in WT mice. However, when we transduced MUP-core mice with rLCMV-env or rLCMV-core/env, we observed that only Env28 (but not Cor93) T_N cell expanded differentiated into effector cells (Fig. 14). This experiment indicates that i) innate immune signals carried by rLCMV vectors are not sufficient to overcome Cor93 T cell dysfunction induced by hepatocellular priming; ii) dysfunctional Cor93 T are not able to provide soluble or membrane-bound inhibitor mediators capable

of affecting an efficient Env28 T cell effector differentiation; iii) hepatocellular antigen presentation is dominant in inducing immune dysfunction.

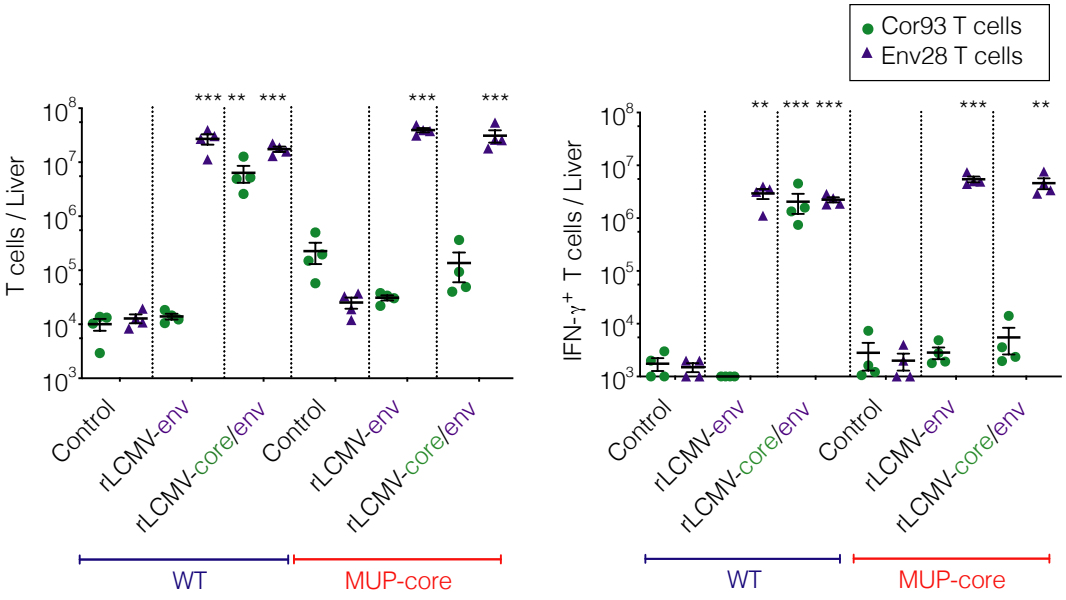

Figure 14. *Spatiotemporal dynamics of naïve CD8+ T cells undergoing intrahepatic priming. (III)*

Cor93 and Env28 naïve CD8⁺ T cells were co-transferred into splenectomized and anti-CD62L-treated C57BL/6 x Balb/c F1 (WT) or MUP-core x Balb/c F1 (MUP-core) recipients. When indicated, mice were injected with rLCMV-env or rLCMV-core/env. Livers were collected and analysed five days after T cell transfer. Total numbers (left) and numbers of IFN-γ-producing (right) Cor93 and Env28 T cells in the livers of indicated mice. (Bénéchet, De Simone et al. Nature 2019).

10.2. Genomic landscape of CD8+ T cells undergoing intrahepatic priming

To further understand the molecular mechanisms underlying the immune dysfunction of hepatically primed $CD8^+$ T cells, we performed transcriptomic (RNA sequencing, RNA-seq) and chromatin accessibility (assay for transposase-accessible chromatin using sequencing, ATAC-seq) analyses of Cor93 $CD8^+$ T cells FACS sorted from the livers of control wild-type mice transduced with rLCMV-core or of MUP-core mice at days 1, 3 and 7 after transfer. All mice were treated as described in Fig.9.

From analyzing the transcriptomic profile of T cells, we observed a progressive transcriptional divergence in intrahepatic Cor93 $CD8^+$ T cells sorted from the two groups of mice. We observed that only $CD8^+$ T cells from wild-type rLCMV-core-transduced mice upregulated genes of the T cell effector program such as Gzma, Gzmb and Ifng[62,63]. By contrast, $CD8^+$ T cells isolated from the livers of MUP-core mice upregulated transcripts that encode a different set of cytokines and chemokines (Ccl1, Csf2 and Xcl1), growth factors and hormones (Areg and Calcb), inhibitory molecules (Pdcd1, Lag3 and Havcr2) or surface markers (Siglecf) (Fig. 15 A).

Moreover, $CD8^+$ T cells from wild-type rLCMV-core-transduced mice or from MUP-core mice had distinct chromatin accessibility profiles at days 3 and 7 after transfer (Fig. 15 B). Motif enrichment analysis on differentially induced ATAC-seq peaks revealed an over-representation of binding sites for transcription factor families involved in effector T cell differentiation, such as IRF, IRF–AP-1 and T-bet at day 3, as well as T-bet, RUNX and bHLH at day 7 in $CD8^+$ T cells from wildtype rLCMV-core-transduced mice[64,65]. By contrast, ATAC-seq peaks of $CD8^+$ T cells from MUP-core mice were enriched in binding sites for AP-1, NFAT, NFAT–AP-1 as well as for NR4A (recently associated with $CD8^+$ T cell dysfunction[66,67]), OCT, TCF and EGR (Fig. 15 C).

From genomic analyses we could then assess that antigen recognition on KCs can support priming and differentiation into effector $CD8^+$ T cells functionally and transcriptionally similar to those recovered from secondary lymphoid organs. By contrast, antigen recognition on hepatocytes leads to a defective differentiation program with progressive accumulation of genomic alterations that ultimately brings to a dysregulated T cell phenotype.

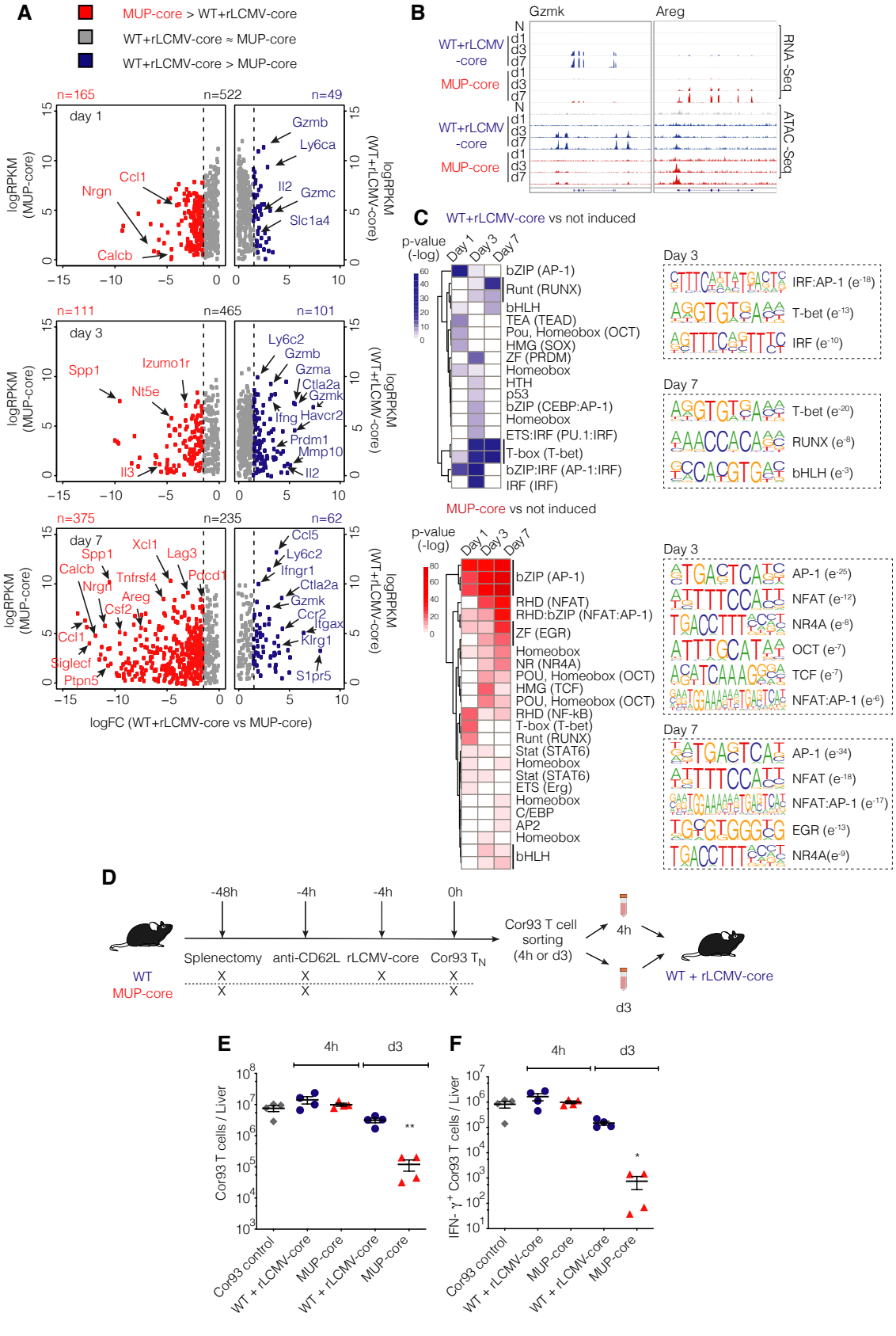
A
MUP-core > WT+rLCMV-core
WT+rLCMV-core ≈ MUP-core
WT+rLCMV-core > MUP-core
n=165
n=522
n=49
day 1
Ccl1
Nrgn
Calcb
Gzmb
Ly6ca
Il2
Gzmc
Slc1a4
n=111
n=465
n=101
day 3
Spp1
Izumo1r
Nt5e
Il3
Ly6c2
Gzmb
Gzma
Ctla2a
Gzmk
Ifng
Havcr2
Prdm1
Mmp10
Il2
n=375
n=235
n=62
day 7
Spp1
Xcl1
Lag3
Calcb
Tnfrsf4
Pdcd1
Nrgn
Areg
Csf2
Ccl1
Siglecf
Ptpn5
Ccl5
Ly6c2
Ifngr1
Ctla2a
Gzmk
Ccr2
Itgax
Klrg1
S1pr5
logRPKM (MUP-core)
logRPKM (WT+rLCMV-core)
logFC (WT+rLCMV-core vs MUP-core)
B
Gzmk
Areg
WT+rLCMV -core
MUP-core
N
d1
d3
d7
RNA-Seq
ATAC-Seq
C
WT+rLCMV-core vs not induced
p-value (-log)
Day 1
Day 3
Day 7
bZIP (AP-1)
Runt (RUNX)
bHLH
TEA (TEAD)
Pou, Homeobox (OCT)
HMG (SOX)
ZF (PRDM)
Homeobox
HTH
p53
bZIP (CEBP:AP-1)
Homeobox
ETS:IRF (PU.1:IRF)
T-box (T-bet)
bZIP:IRF (AP-1:IRF)
IRF (IRF)
Day 3
IRF:AP-1 (e-18)
T-bet (e-13)
IRF (e-10)
Day 7
T-bet (e-20)
RUNX (e-8)
bHLH (e-3)
MUP-core vs not induced
bZIP (AP-1)
RHD (NFAT)
RHD:bZIP (NFAT:AP-1)
ZF (EGR)
Homeobox
NR (NR4A)
POU, Homeobox (OCT)
HMG (TCF)
POU, Homeobox (OCT)
RHD (NF-kB)
T-box (T-bet)
Runt (RUNX)
Stat (STAT6)
Homeobox
Stat (STAT6)
ETS (Erg)
Homeobox
C/EBP
AP2
Homeobox
bHLH
Day 3
AP-1 (e-25)
NFAT (e-12)
NR4A (e-8)
OCT (e-7)
TCF (e-7)
NFAT:AP-1 (e-6)
Day 7
AP-1 (e-34)
NFAT (e-18)
NFAT:AP-1 (e-17)
EGR (e-13)
NR4A(e-9)
D
-48h
-4h
-4h
0h
Splenectomy
anti-CD62L
rLCMV-core
Cor93 T_N
WT
MUP-core
Cor93 T cell sorting (4h or d3)
4h
d3
WT + rLCMV-core
E
4h
d3
Cor93 T cells / Liver
Cor93 control
WT + rLCMV-core
MUP-core
WT + rLCMV-core
MUP-core
F
4h
d3
IFN- γ+ Cor93 T cells / Liver
Cor93 control
WT + rLCMV-core
MUP-core
WT + rLCMV-core
MUP-core

Figure 15. *Transcriptomic and chromatin accessibility analyses of CD8+ T cells undergoing intrahepatic priming.*

*(***A***) Scatter plot showing the level (y axis) and the difference in expression (x axis) of inducible genes in the dataset (versus Cor93 T_N) in the indicated conditions. Genes expressed at higher levels in WT + rLCMV-core or MUP-core mice are shown in blue or red, respectively. (***B***) Integrative Genomics Viewer (IGV) snapshots showing RNA-seq and ATAC-seq data at Gzmk and Areg loci, selected as representative genes with differential expression in WT + rLCMV-core or MUP-core mice, respectively. (***C***) Left panels. Heatmap showing the enrichment of DNA motifs (HOMER) within the top 200 inducible (versus Cor93 T_N) and differential ATAC-Seq peaks in WT + rLCMV-core (blue) or MUP-core mice (red). A set of 3899 non-inducible ATAC-seq peaks was used as background. Right panels. Selected enriched motifs and putative cognate transcription factors in ATAC-Seq peaks from WT + rLCMV-core (top) or MUP-core (bottom) mice. Values between brackets indicates p-value. () Schematic representation of the experimental setup. (***E-F***) Total numbers (***E***) and numbers of IFN-γ-producing (***F***) Cor93 T cells in the livers of the indicated mice. (Bénéchet, De Simone et al. Nature 2019).*

We then investigated whether the dysfunctional phenotype of T cells was permanent once acquired or it could be reverted by subsequential immune stimulations.

To this end, we sorted Cor93 T cells from MUP-core livers 4 hours or 3 days after injection and then we transferred into wild-type rLCMV-core-transduced mice (Fig. 15 D). We observed that cells that sorted after 4h from livers of MUP-core mice were fully capable of expanding and differentiating into effector cells upon rLCMV re-stimulation. In contrast, cells isolated at day 3 (a time point in which chromatin alterations were evident, as shown before) were significantly impaired in their ability to expand and differentiate into IFNγ-producing cells once transferred into wild-type rLCMV-core-transduced mice (Fig. 15 E-F). These data indicate that three days of continuous hepatocellular antigen exposure renders T cells partially refractory to further stimuli that could make them acquire effector functions.

When we analyzed gene set from effector vs. dysfunctional of Cor93 T cells by gene set enrichment analysis (GSEA) we identified that genes with higher expression in $CD8^+$ T cells from wild-type mice transduced with rLCMV-core were enriched in GO categories belonged to gene sets of effector immune responses, such as responses to type I interferon, cell proliferation, T cell migration and cell–cell adhesion. On the other hand, $CD8^+$ T cells from MUP-core mice expressed genes belonging to GO categories linked to tissue development and organ remodeling, cell differentiation and cell-matrix

interaction and were not obviously overlapping with GO of other known dysfunctional $CD8^+$ T cell profiles. Genes with selective expression in our dysfunctional cells were indeed poorly expressed in reference transcriptomic datasets of splenic LCMV-specific exhausted $CD8^+$ T cell[68,69] or tolerant self-antigen-specific $CD8^+$ T cells[70]. However, we observed an exhaustion-like signature progressively enriched in the transcriptome of $CD8^+$ T cells from MUP-core mice at days 3 and 7 after transfer, as determined by GSEA (Fig. 16 A). These data indicate that, while priming by hepatocytes initiates a unique dysfunctional program, hepatocellular antigen persistence gradually triggers an additional exhaustion profile.

10.3. Dysfunctional CD8+ T cells can be rescued by IL-2 but not by anti-PD-L1 Abs

Among the genes that are differentially expressed between the dysfunctional T cells in MUP-core mice and effector T cells in WT mice transduced with rLCMV-core, we focused on two known regulators of T cell function: Pdcd1 (coding gene for the surface protein PD-1) and Il2 (coding gene for the cytokine IL-2)[71,72,73,74].

Pdcd1 was hyper-expressed in hepatic Cor93 $CD8^+$ T cells sorted from MUP-core mice, whereas Il2 was found to be hyper-expressed on Cor93 $CD8^+$ T cells sorted from the livers of WT mice transduced with rLCMV (Fig. 15 A).

In order to understand the functional outcomes of these findings we transfer Cor93 T_N cell and we treated MUP-core mice with anti-PD-L1 blocking antibodies, with recombinant IL-2 coupled with non-neutralizing IL-2-specific monoclonal antibodies (S4B6) that enhance the half-life of IL-2 *in vivo*[75], or with a combination of both treatments. Interestingly, the exogenous administration of IL-2c promoted expansion and differentiation of Cor93 T cells into IFNγ-producing, cytotoxic effector cells, whereas anti-PD-L1 treatment had no effect either when given alone or had any further combinatorial effect when given with IL-2c (Fig. B-E).

Not only the phenotype of dysfunctional cell was rescued, but we also observed a substantial rescue of the dysfunctional gene program as observed by analyzing the transcriptomic profile of Cor93 T cells upon administration of IL-2c 1 day after transfer into MUP-core mice. More than half of hypo-expressed genes in $CD8^+$ T cells from MUP-core mice were indeed upregulated in IL-2c-treated MUP-core mice, often reaching expression levels comparable to those detected in effector cells isolated by wild-type mice injected with rLCMV-core.

Similarly, a comparable fraction of hyper-expressed genes in dysfunctional hepatic $CD8^+$ T cells isolated from untreated MUP-core mice were downregulated upon IL-2c treatment (Fig. 16 F).

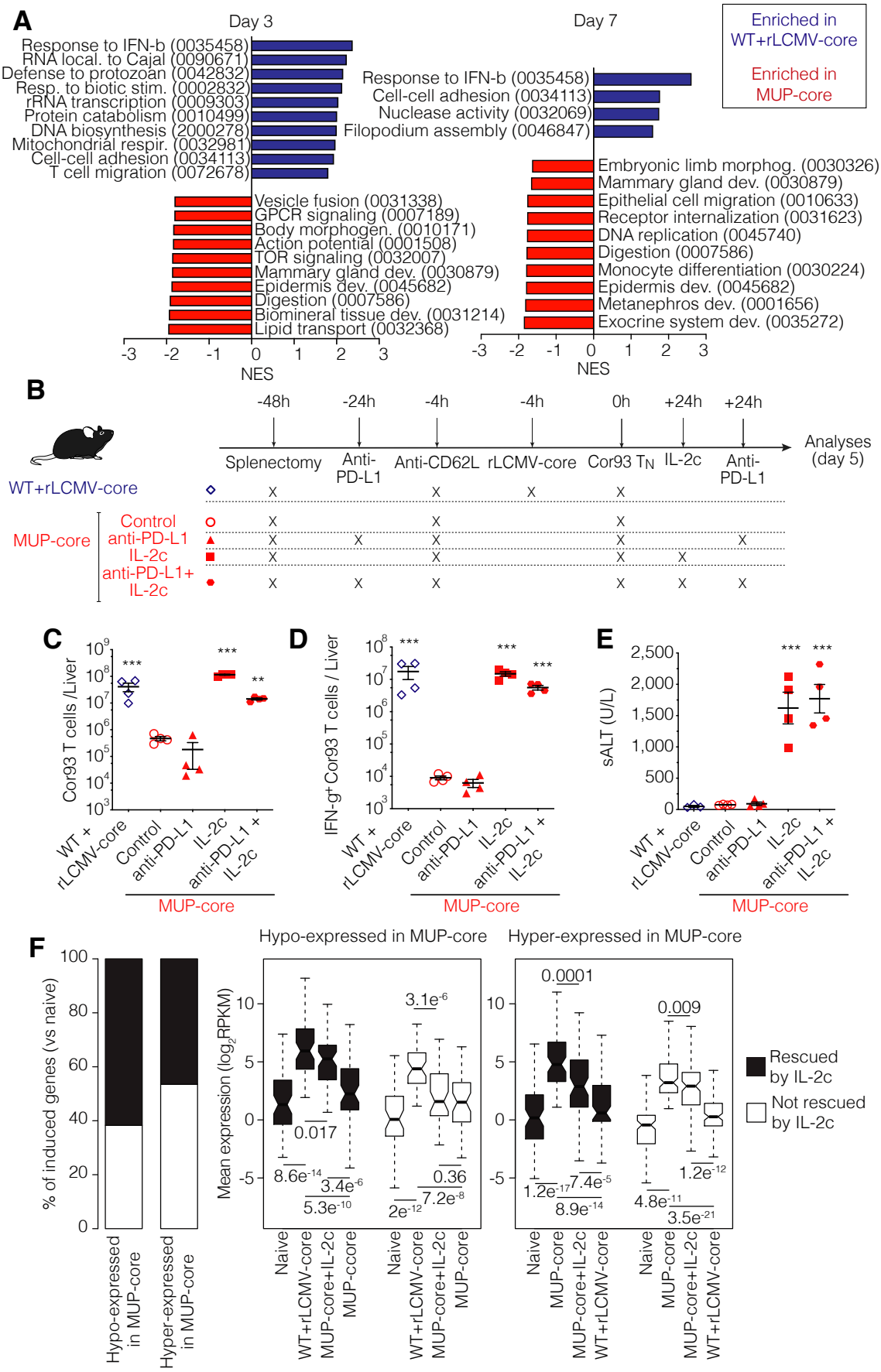
A
Day 3
Day 7
Enriched in WT+rLCMV-core
Enriched in MUP-core
Response to IFN-b (0035458)
RNA local. to Cajal (0090671)
Defense to protozoan (0042832)
Resp. to biotic stim. (0002832)
rRNA transcription (0009303)
Protein catabolism (0010499)
DNA biosynthesis (2000278)
Mitochondrial respir. (0032981)
Cell-cell adhesion (0034113)
T cell migration (0072678)
Vesicle fusion (0031338)
GPCR signaling (0007189)
Body morphogen. (0010171)
Action potential (0001508)
TOR signaling (0032007)
Mammary gland dev. (0030879)
Epidermis dev. (0045682)
Digestion (0007586)
Biomineral tissue dev. (0031214)
Lipid transport (0032368)
Response to IFN-b (0035458)
Cell-cell adhesion (0034113)
Nuclease activity (0032069)
Filopodium assembly (0046847)
Embryonic limb morphog. (0030326)
Mammary gland dev. (0030879)
Epithelial cell migration (0010633)
Receptor internalization (0031623)
DNA replication (0045740)
Digestion (0007586)
Monocyte differentiation (0030224)
Epidermis dev. (0045682)
Metanephros dev. (0001656)
Exocrine system dev. (0035272)
NES
B
-48h
-24h
-4h
-4h
0h
+24h
+24h
Splenectomy
Anti-PD-L1
Anti-CD62L
rLCMV-core
Cor93 TN
IL-2c
Anti-PD-L1
Analyses (day 5)
WT+rLCMV-core
MUP-core
Control
anti-PD-L1
IL-2c
anti-PD-L1+ IL-2c
C
Cor93 T cells /Liver
D
IFN-g+ Cor93 T cells / Liver
E
sALT (U/L)
WT + rLCMV-core
Control
anti-PD-L1
IL-2c
anti-PD-L1 + IL-2c
MUP-core
F
% of induced genes (vs naive)
Hypo-expressed in MUP-core
Hyper-expressed in MUP-core
Mean expression (log2RPKM)
Hypo-expressed in MUP-core
Hyper-expressed in MUP-core
Naive
WT+rLCMV-core
MUP-core+IL-2c
MUP-core
Rescued by IL-2c
Not rescued by IL-2c

Figure 16. *Intrahepatically-primed, dysfunctional $CD8^+$ T cells can be rescued by IL-2, but not by anti-PD-L1 Abs.*

*(**A**) Normalized enrichment score (NES) of selected GO categories enriched within genes expressed at higher levels in WT + rLCMV-core (blue) or from MUP-core (red) mice at the indicated time points. GO categories were identified by GSEA42 and grouped by similarity with REVIGO43. (**B**) Schematic representation of the experimental setup. (**C**-**D**) Total numbers (**C**) and numbers of IFN-γ-producing (**D**) Cor93 T cells in the livers of the indicated mice. (**E**) ALT levels in the sera of the indicated mice. (**F**) Left panel. Stacked bar plot showing the effect of IL-2c on genes induced at day 5 (versus naïve) in Cor93 T cells from WT + rLCMV-core or MUP-core mice. Genes hypo-expressed or hyper-expressed in MUP-core mice as compared to WT + rLCMV-core mice are shown separately. Right panels. Box plots showing expression levels of hypo-expressed (left) or hyper-expressed (right) genes at day 5 in the indicated conditions. Genes the expression of which is rescued or not rescued in MUP-core+IL2c mice are shown in black or white, respectively. (Bénéchet, De Simone et al. Nature 2019).*

10.4. Therapeutic potential of IL-2 treatment for T cell restoration during chronic HBV infection

Finally, to test the clinical potential of IL-2 in a system that may limit its systemic toxicity[72], we generated third-generation, self-inactivating lentiviral vectors (LV.ET.mIL2.142T) that allow selective hepatocellular expression of mouse IL-2[76]. We injected wild-type or MUP-core mice with 2.5×10^8 (LV-IL2^{low}) or 5×10^8 (LV-IL2^{high}) transducing units per mouse, 7 days before Cor93 or control T_N cell injection. Lentiviral-mediated hepatic expression of IL-2, even at a dose that transduces less than 10% of hepatocytes in vivo, increased the capacity of Cor93 (but not control) T cells to expand and differentiate into IFNγ-producing cells endowed with cytolytic capacities (Fig. 17).

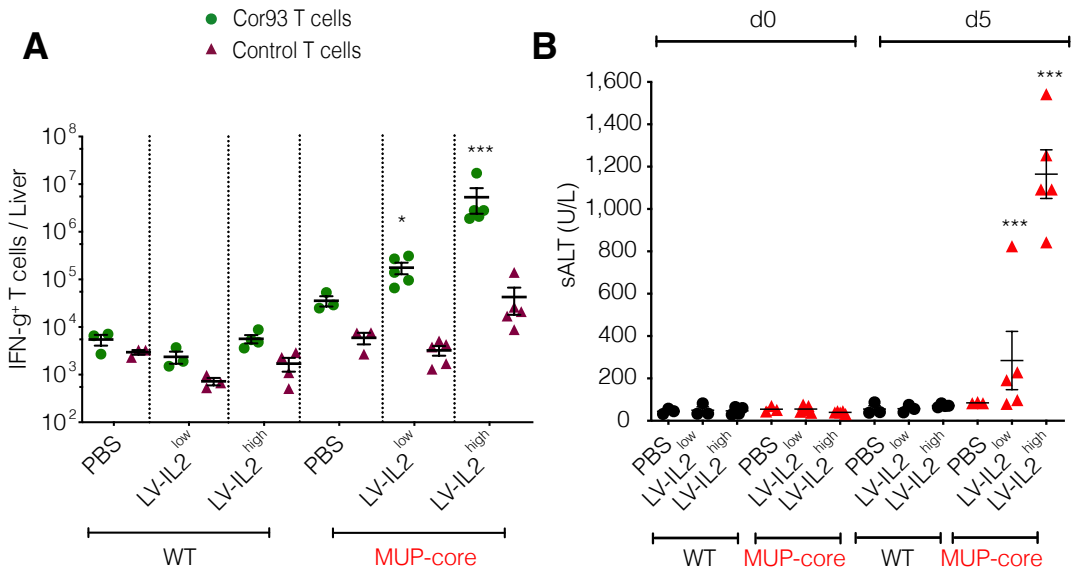

Figure 17. *Therapeutic potential of IL-2 treatment for T cell restoration during chronic HBV infection. (***A***) Absolute numbers of IFN-γ-producing T cells in the livers of the indicated mice. (***B***) Serum ALT levels at day 0 and day 5 in the same mice. (Bénéchet, De Simone et al. Nature 2019).*

Altogether, those data suggest that the functional and genomic program of dysfunction acquired by T cells after hepatic priming could be reverted by the treatment with IL-2. After the treatment indeed, dysfunctional cells can reprogram their gene expression and start to secrete cytotoxic cytokines, acquiring antiviral functions similar to those of effector cells primed by hAPCs.

However, whether IL-2 exerts a direct effect on HBV-specific T cell or an indirect effect on other cell population remains to be determined.

10.5. KCs but not DCs are required for optimal in vivo reinvigoration of intrahepatically-primed T cells by IL-2

In order to understand the immune mechanisms driving the IL-2-mediated reinvigoration, we took advantage of the experimental setup previously described: naïve Cor93 and Env28 T_N were injected in MUP-core transgenic mice and WT mice transduced with rLCMV-core/env (as control) and selected MUP-core mice received IL-2c 24h before cell transfer[77].

To test whether IL-2c treatment acts directly on T_N or whether the presence of additional cells is required, we performed depletion experiments on possible target cell candidates.

We initially focused on KCs and DCs, since these cells can induce full effector differentiation of $CD8^+$ T cells upon LCMV-core/env transduction, as previously described[77].

To this end, liver macrophages were depleted through clodronate liposomes (CLL) intravenous injection two days before T cell injection: this treatment effectively depletes KCs while does not affect hepatic DCs compartment[61,77] (Fig. 18 A-F).

Interestingly, we noticed that optimal *in vivo* reinvigoration of intrahepatically primed Cor93 T cells required the presence of KCs but apparently not DCs, as IL-2c treatment failed to improve T cell expansion, effector differentiation and intraparenchymal cluster formation in CLL-treated mice (Fig. 18 G-I).

Similar results were obtained when recombinant IL-2 was used in place of IL-2c and when HBV replication competent transgenic mice in place of MUP-core recipients (data not shown).

To confirm that hepatic DCs are not necessary for the optimal *in vivo* response to IL-2, we depleted this cell population as well.

First, we generated BM chimeras irradiating MUP-core mice and reconstituting them with $CD11c^{DTR}$ bone marrow or WT BM. After reconstitution, we injected mice with diphtheria toxin (DT) (which significantly decreased the number of hepatic DCs while sparing KCs) and proceeded with cell transfer and IL-2 treatment (Fig. 18 J-O).

We observed that DC depletion did not affect the capacity of IL-2 to promote expansion, effector differentiation and cluster accumulation around portal tracts of intrahepatically-primed Cor93 T cells (Fig. 18 P-R).

Moreover, since CLL treatment acts broadly and not exclusively on KCs, we wanted to assess the possible contribution of other phagocytic cells such as neutrophils and monocytes. To this end, we injected MUP-core mice with depleting Abs to erase neutrophil (via anti-Ly6G Abs) or both neutrophil and monocyte (via anti-Gr1Abs) populations and we proceeded with the experimental setup of T cell transfer and IL-2 administration, as previously described.

We observed that neither neutrophil nor monocyte depletion affected the in vivo reinvigoration of intrahepatically-primed T cells by IL-2 (data not shown).

Taken together, these results indicate that KCs are required for optimal in vivo reinvigoration of intrahepatically-primed T cells by IL-2.

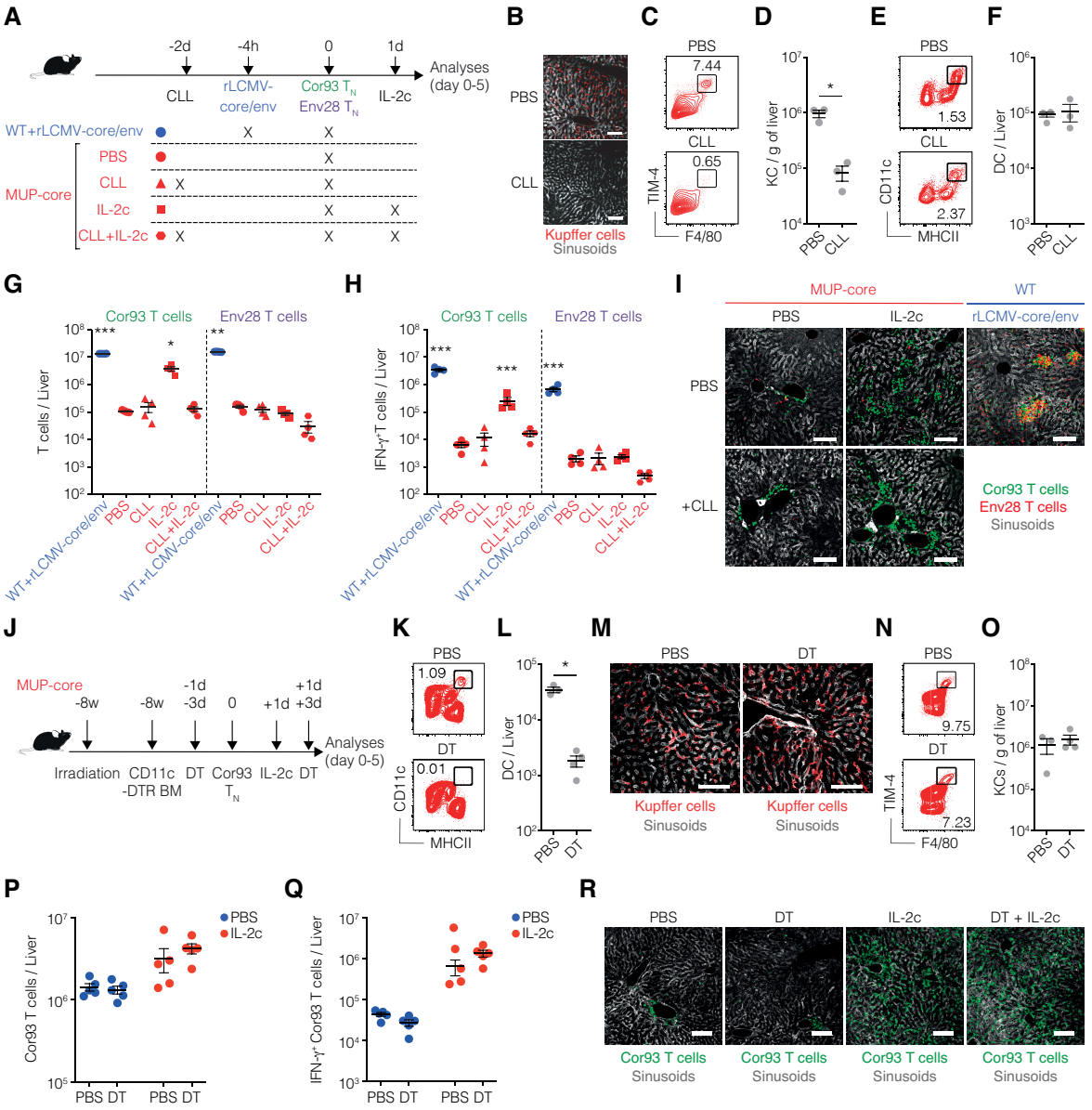
A
-2d
-4h
0
1d
CLL
rLCMV-core/env
Cor93 T_N Env28 T_N
IL-2c
Analyses (day 0-5)
WT+rLCMV-core/env
MUP-core
PBS
CLL
IL-2c
CLL+IL-2c
B
PBS
CLL
Kupffer cells
Sinusoids
C
PBS
7.44
CLL
0.65
TIM-4
F4/80
D
KC / g of liver
PBS
CLL
E
PBS
1.53
CLL
2.37
CD11c
MHCII
F
DC / Liver
G
Cor93 T cells
Env28 T cells
T cells / Liver
H
IFN-γ+ T cells / Liver
I
MUP-core
WT
PBS
IL-2c
rLCMV-core/env
+CLL
Cor93 T cells
Env28 T cells
Sinusoids
J
MUP-core
-8w
-8w
-1d
-3d
0
+1d
+1d
+3d
Irradiation
CD11c -DTR BM
DT
Cor93 T_N
IL-2c
DT
Analyses (day 0-5)
K
PBS
1.09
DT
0.01
CD11c
MHCII
L
DC / Liver
PBS
DT
M
PBS
DT
Kupffer cells
Sinusoids
N
PBS
9.75
DT
7.23
TIM-4
F4/80
O
KCs / g of liver
P
Cor93 T cells / Liver
PBS
IL-2c
PBS DT
PBS DT
Q
IFN-γ+ Cor93 T cells / Liver
R
PBS
DT
IL-2c
DT + IL-2c
Cor93 T cells
Sinusoids

Figure 18. *KCs are required for optimal in vivo reinvigoration of intrahepatically-primed T cells by IL-2.*

*(**A**) Schematic representation of the experimental setup. 5 x 10^6 Cor93 and Env28 T_N were transferred into C57BL/6 x Balb/c F1 (WT) or MUP-core x Balb/c F1 (MUP-core) recipients. When indicated, mice were injected with 2.5 x 10^5 infectious units of non-replicating rLCMV-core/env 4h prior to T_N transfer. Selected MUP-core mice received clodronate liposomes (CLL) and/or IL-2/anti-IL-2 complexes (IL-2c) at the indicated timepoints. Livers were collected and analyzed five days after T_N transfer. (**B**) Representative confocal immunofluorescence micrographs of liver sections from the indicated mice 48h after CLL treatment. KCs were identified as F4/80$^+$ cells and are depicted in red. Sinusoids were identified as Lyve-1$^+$ cells and are depicted in grey. Scale bars represent 100 µm. (**C-D**) Representative flow cytometry plot (**C**) and absolute numbers (**D**) of KCs from the indicated mice 48h after CLL treatment. KCs were identified as live, CD45$^+$, TIM4$^+$, F4/80$^+$ cells. n = 3 * p value< 0.05, one-tailed Mann-Whitney U-test. (**E-F**) Representative flow cytometry plot (**E**) and absolute numbers (**F**) of dendritic cells (DCs, identified as live, MHC-II^{hi}, CD11c$^+$ cells) from the indicated mice 48h after CLL treatment. n = 3. (**G-H**) Total numbers (**G**) and numbers of IFN-γ-producing (**H**) Cor93 and Env28 T cells in the livers of indicated mice. n = 4. *p value< 0.05, ** p value< 0.01, *** p value< 0.001, one-way Brown-Forsythe and Welch ANOVA test with Dunnett correction for multiple comparison. Each group was compared to control. Normal distribution was verified by Shapiro-Wilk test. (**I**) Representative confocal immunofluorescence micrographs of liver sections from the indicated mice five days after T_N transfer. Cor93 T cells were identified as GFP$^+$ cells and are depicted in green. Env28 T cells were identified as DsRed$^+$ cells and are depicted in red. Sinusoids were identified as Lyve-1$^+$ cells and are depicted in grey. Scale bars represent 100 µm. (**J**) Schematic representation of the experimental setup. MUP-core mice were lethally irradiated and reconstituted with CD11c^{DTR} bone marrow (BM). Eight weeks after BM reconstitution, 1 x 10^6 Cor93 T_N were transferred. Indicated mice were treated with diphtheria toxin (DT) every 48h starting from three days before T cell injection. Indicated mice received IL-2c one day after Cor93 T cell transfer. Livers were collected and analyzed five days after T_N transfer. (**K-L**) Representative flow cytometry plot (**K**) and absolute numbers (**L**) of DCs (identified as live, MHC-II^{hi}, CD11c$^+$ cells) from the indicated mice at the time of Cor93 T cell transfer. (PBS, n = 3; DT n = 4) * p value< 0.05, one-tailed Mann-Whitney U-test. (**M**) Representative confocal immunofluorescence micrographs of liver sections from the indicated mice 48h after DT treatment. KCs were identified as F4/80$^+$ cells and are depicted in red. Sinusoids were identified as Lyve-1$^+$ cells and are depicted in grey. Scale bars represent 50 µm. (**N-O**) Representative flow cytometry plot (**N**) and absolute numbers (**O**) of KCs (identified as live, CD45$^+$, TIM4$^+$, F4/80$^+$ cells) from the indicated mice at the time of Cor93 T cell transfer (PBS, n = 3; DT n = 4). (**P-Q**) Total numbers (**P**) and numbers of IFN-γ-producing (**Q**) Cor93 T cells in the livers of the indicated mice. (n = 5). (**R**) Representative confocal immunofluorescence micrographs of liver sections from the indicated mice five days after T_N transfer. Cor93 T cells were identified as CD45.1$^+$ cells and are depicted in green. Sinusoids were identified as Lyve-1$^+$ cells and are depicted in grey. Scale bars represent 100 µm. Data are representative of at least 3 independent experiments. (De Simone et al. Immunity 2021).*

10.6. KCs respond to IL-2 and cross-present hepatocellular antigens

To have a better understanding of KC contribution to the IL-2 mediated T cell reinvigoration, we decided to deeply characterize KC sensitivity to IL-2 and the response to the treatment.

First, we investigated the presence of an IL-2 sensing machinery on KC. To this end, we performed flow cytometric analyses and we observed that a fraction of KCs expresses all 3 subunits of the IL-2 receptor (CD25, CD122 and CD132), thus implying that KCs might bind exogenous IL-2 by surface receptors (Fig. 19 A-B).

To test the functionality of the IL-2 receptor on KCs, we decided to investigate their response to the treatment by isolating liver non-parenchymal cells (LNPCs) –including KCs– from WT mice and stimulating them *ex vivo* with recombinant IL-2.

When we analyzed the phosphorylation of STAT5 (one of the first intracellular mediators of IL-2 receptor signaling), we observed a dose-dependent increase in in KCs, but not in liver sinusoidal endothelial cells (LSECs). Similar results were obtained when IL-2c was used in place of IL-2 (Fig. 19 C-E).

This data indicate that KCs express a functional IL-2 receptor capable of responding to IL-2 in vitro.

Once we assessed the functionality of IL-2 sensing on KCs, we proceeded on the study of the effects of the treatment on these cells by analyzing their transcriptome upon IL-2 administration. To this end, we treated WT mice with IL-2c and 48 hours later we performed RNA-seq analysis on FACS-sorted KCs (Fig. 19 F).

When we analyzed the differentially expressed genes (DEGs) between untreated and treated mice, ewe identified 4073 genes (1515 up- and 2558 down-regulated) as significantly regulated by IL-2c.

Functional enrichment analysis of up-regulated genes showed an increased transcription of genes involved mainly in Ag presentation and proteasomal processing, ribosomal RNA processing and splicing, DNA replication and cell cycle, as well as mitochondrial oxidative metabolism.

Among the up-regulated gene clusters, we focused on the Ag presentation pathway which includes several macromolecular complexes comprised of ubiquitins, chaperones, MHC-I, and proteasome subunits (Fig. 19 G-J).

Moreover, we confirmed the up-regulation of MHC-I and costimulatory molecules on KCs isolated from mice treated with IL-2c by flow cytometric analyses (Fig. 19 L).

Based on the results, we reasoned that the mechanisms by which IL-2 could act *in vivo* might be trough the increase of cross-presentation ability of KCs to naïve $CD8^+$ T cells. To test this possibility, we measured the capacity of *in vitro* differentiated Cor93 T_E to produce IFN-γ (as an indirect measure of Ag recognition) upon incubation with KCs isolated from HBV replication-competent transgenic mice treated or not treated with IL-2c. Interestingly, treating HBV replication-competent transgenic mice with IL-2c slightly but significantly increased the capacity of KCs to cross-present antigen to Cor93 T_E *in vitro* (Fig. 19 M-O).

Of note, baseline KC cross-presentation of the core protein in this experimental system at steady state is negligible, despite KCs being constantly exposed to abundant HBV virions in the circulation. Moreover, we observed that Cor93 T_N remain dysfunctional even when isolated from the liver of HBV replication-competent transgenic mice previously transferred with highly pathogenic Env28 T_E cells (data not shown), indicating that cross-presentation by KCs is not inducing effector T cell differentiation even during acute liver inflammation.

Next, we wanted to evaluate if *in vivo* IL-2 treatment could also improve the capacity of KCs to present antigens in vitro to naive $CD8^+$ T cells. To this end, we treated WT mice with IL-2 or PBS (as control), and we isolated KCs 48h after treatment; we then *in vitro* co-cultured KCs with HBV-specific naive $CD8^+$ T cells in a medium containing the serum of HBV replication-competent transgenic mice. When compared to KCs isolated from PBS-treated mice, KCs exposed to IL-2 *in vivo* induced a higher proliferation of Cor93 T_N in in vitro culture (Fig.19 P-R).

Finally, to evaluate the relevance of the *in vitro* experiments, we decided to setup an experimental system that allowed us to study the antigen cross presentation capacity of KC, with the notion that in MUP-core mice KC cross-presentation should depend on the uptake of the few hepatocytes that are injured by Cor93 T_N transfer (as previously described).

We then generated MUP-core mouse chimeras whose hematopoietic cells (including KCs) lack Tap1, a transporter protein essential for the expression of MHC-I molecules (so required to present Ags to $CD8^+$ T cells).

We generated chimeras by injection of either WT or $Tap1^{-/-}$ bone marrow into irradiated MUP-core mice, followed by CLL treatment in order to deplete the residual radioresistant KCs; we then allowed the complete reconstitution of the entire KC compartment with bone marrow-derived cells[61]. After the reconstitution, we injected Cor93 T_N and treated mice with IL-2c, as previously described.

We observed that cells that underwent priming into MUP-core mice whose KCs lacked MHC-I had a much lower response to IL-2c than did Cor93 T_N injected into mice carrying WT KCs, suggesting that Cor93 T cells interacted with IL-2-stimulated KCs and those cells cross-presented hepatocyte-derived epitopes after their uptake (Fig. 19 S-U).

Taken together, these results indicate that optimal reinvigoration of intrahepatically primed $CD8^+$ T cells by IL-2 requires the capacity of KCs to cross-present HBV Ags, possibly derived from circulating virions and/or damaged hepatocytes.

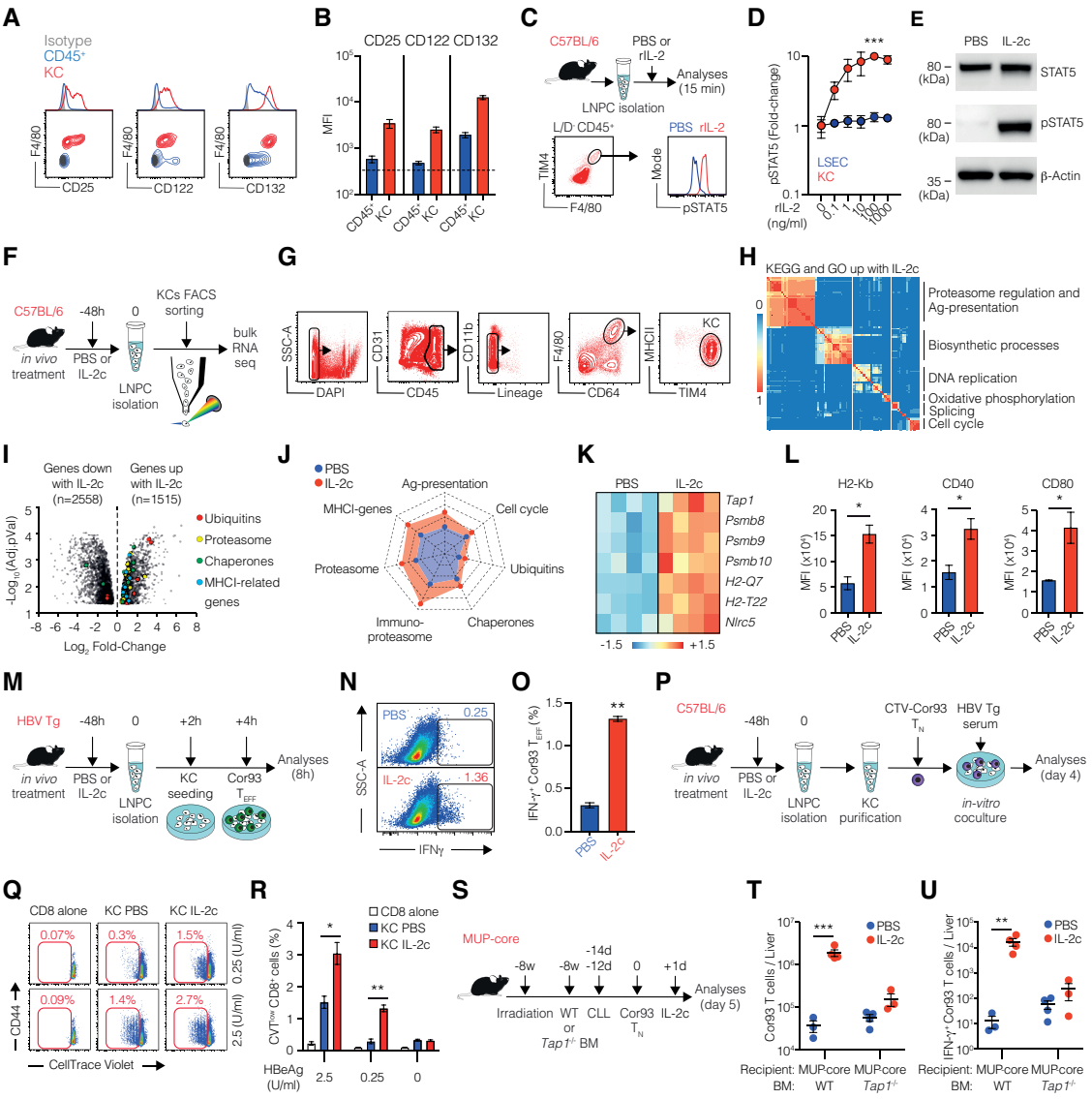
A
Isotype
CD45+
KC
F4/80
CD25
CD122
CD132
B
CD25 CD122 CD132
MFI
CD45+ KC
C
C57BL/6
PBS or rIL-2
Analyses (15 min)
LNPC isolation
L/D- CD45+
TIM4
F4/80
PBS rIL-2
Mode
pSTAT5
D
***
pSTAT5 (Fold-change)
LSEC
KC
rIL-2 (ng/ml)
E
PBS IL-2c
80 – (kDa)
STAT5
pSTAT5
35 – (kDa)
β-Actin
F
C57BL/6
-48h
0
KCs FACS sorting
in vivo treatment
PBS or IL-2c
LNPC isolation
bulk RNA seq
G
SSC-A
DAPI
CD31
CD45
CD11b
Lineage
F4/80
CD64
MHCII
TIM4
KC
H
KEGG and GO up with IL-2c
Proteasome regulation and Ag-presentation
Biosynthetic processes
DNA replication
Oxidative phosphorylation
Splicing
Cell cycle
I
Genes down with IL-2c (n=2558)
Genes up with IL-2c (n=1515)
-Log10(Adj.pVal)
Log2 Fold-Change
Ubiquitins
Proteasome
Chaperones
MHCI-related genes
J
PBS
IL-2c
Ag-presentation
Cell cycle
Ubiquitins
Chaperones
Immuno-proteasome
Proteasome
MHCI-genes
K
PBS IL-2c
Tap1
Psmb8
Psmb9
Psmb10
H2-Q7
H2-T22
Nlrc5
-1.5 +1.5
L
H2-Kb
CD40
CD80
MFI (x10³)
PBS IL-2c
M
HBV Tg
-48h
0
+2h
+4h
in vivo treatment
PBS or IL-2c
LNPC isolation
KC seeding
Cor93 TEFF
Analyses (8h)
N
PBS
IL-2c
0.25
1.36
SSC-A
IFNγ
O
IFN-γ+ Cor93 TEFF (%)
PBS
IL-2c
P
C57BL/6
-48h
0
in vivo treatment
PBS or IL-2c
LNPC isolation
KC purification
CTV-Cor93 TN
HBV Tg serum
in-vitro coculture
Analyses (day 4)
Q
CD8 alone
KC PBS
KC IL-2c
0.07%
0.3%
1.5%
0.09%
1.4%
2.7%
CD44
CellTrace Violet
0.25 (U/ml)
2.5 (U/ml)
R
CD8 alone
KC PBS
KC IL-2c
CV7low CD8+ cells (%)
HBeAg (U/ml)
2.5
0.25
0
S
MUP-core
-8w
-8w
-14d -12d
0
+1d
Irradiation
WT or Tap1-/- BM
CLL
Cor93 TN
IL-2c
Analyses (day 5)
T
Cor93 T cells / Liver
PBS
IL-2c
Recipient: MUPcore MUPcore
BM: WT Tap1-/-
U
IFN-γ+ Cor93 T cells / Liver
PBS
IL-2c
Recipient: MUPcore MUPcore
BM: WT Tap1-/-

Figure 19. *KCs respond to IL-2 and cross-present hepatocellular Ags.*

*(**A**) Representative flow cytometry plots of CD25 (left panel), CD122 (middle panel), and CD132 (right panel) expression on CD45$^+$ (blue) and F4/80$^+$ (red) cell populations in the livers of C57BL/6 mice. Isotype control is depicted in gray. (**B**) Mean Fluorescent Intensity (MFI) of CD25 (left), CD122 (middle), CD132 (right) expression on live CD45$^+$ (blue) and KCs (red identified as live, CD45$^+$, TIM4$^+$, F4/80$^+$ cells) cells in the livers of C57BL/6 mice. (n = 3). (**C**) Schematic representation of the experimental setup. Liver non-parenchymal cells (LNPCs) were isolated from C57BL/6 mice and incubated in vitro for 15 minutes with increasing doses of rIL-2. pSTAT5 signal was analyzed on CD45$^+$ F4/80$^+$ TIM4$^+$ cells (KCs) or CD31$^+$ CD45$^-$ cells (LSECs) by flow cytometry (representative plot of KCs at the bottom). (**D**) Fold change of STAT5 phosphorylation upon treatment with the indicated concentrations of rIL-2 in KCs (red dots) or LSECs (blue dots). (n = 3) *** p value< 0.001, two-way ANOVA with Geisser-Greenhouse's correction. Significance indicates time x column factor. (**E**) Immunoblot analysis of STAT5 and pSTAT5 in adherent KCs isolated from C57BL/6 mice and incubated in vitro with IL-2c or PBS. (**F**) Schematic representation of the experimental setup. C57BL/6 mice were treated in vivo with PBS or IL-2c. 48h after treatment, liver non-parenchymal cells (LNPCs) were isolated and RNA-seq was performed on flow cytometry-sorted KCs. (**G**) KC sorting strategy. KCs were identified as live, CD45$^+$, Lineage$^-$ (CD3, CD19, Ly6G, CD49b), F4/80$^+$, CD64$^+$, MHCII^{int}, TIM4$^+$ cells (n = 4 per group). (**H**) Clustering of top significant (EnrichR Combined Score > 100, FDR < 0.05) Gene Ontology Biological Processes and KEGG pathways of processes up-regulated in KCs upon in vivo IL-2c treatment. The thermal scale represents the Jaccard Similarity Coefficient between every gene set pair (blue representing a 0 Similarity Coefficient, red a 1 Similarity Coefficient). (**I**) Volcano plot of RNA-Seq results. The X-axis represents the Log2 Fold-Change of Differentially Expressed Genes (DEG) upon IL-2c treatment, the Y-axis the -Log10(FDR). Only DEGs with an FDR < 0.05 were considered. Genes belonging to specific biological process are highlighted in different colors (see also **Fig. S3A-E**). (**J**) Radar plot of different biological processes. Each dimension of the radar plot is represented as the mean of the Transcripts Per kilobase Million (TPM) of selected genes (see also **Fig. S3A-E**), in PBS (blue) and IL-2c treated (red) samples. Values range from 0 to 350 TPM. (**K**) Heatmap of selected genes linked to Ag presentation that were upregulated in KCs upon IL-2c treatment. Values are in Z-score, calculated from scaling by row the Log2(TPM) values. (**L**) MFI of H2-K^b, CD40 and CD80 expression on KCs (defined as live, CD45$^+$, TIM4$^+$, F4/80$^+$ cells) 48h after PBS or IL-2c treatment in vivo. (n = 3) * p value< 0.05, one-tailed Mann-Whitney U-test. (**M**) Schematic representation of the experimental setup. HBV replication-competent transgenic mice (HBV Tg) were treated in vivo with PBS or IL-2c. After 48h liver non-parenchymal cells (LNPCs) were isolated, KCs were seeded for 2h and co-cultured with in vitro-differentiated Cor93 effector T cells (Cor93 T_E). After 4h, T cells were harvested and analyzed by flow cytometry. (**N-O**) Representative flow cytometry plot (**N**) and percentage (**O**) of IFN-g producing Cor93 T_{EFF} cells in the indicated conditions. (n = 3) ** p value< 0.01, one-tailed Mann-Whitney U-test. (**P**) Schematic representation of the experimental setup. C57BL/6 mice were treated in vivo with PBS or IL-2c. After 48h LNPCs were isolated, and KCs were purified by immunomagnetic separation. Purified KCs were co-cultured with CellTrace^{TM} violet (CTV)-labelled Cor93 T_N. Serum from HBV replication-competent transgenic mice (containing the indicated concentrations of HBeAg) was added to the wells (note that HBeAg contains the Cor93 determinant). After 4 days, Cor93 T cells were harvested and analyzed by flow cytometry. (**Q-R**) Representative flow cytometry plots (**Q**) and percentages (**R**) of proliferating Cor93 T cells at the indicated conditions. * p value< 0.05, ** p value< 0.01, one-way Brown-Forsythe and Welch ANOVA test with Dunnett correction for multiple comparison. Each group was compared to every other group within the same Ag dose. (n = 3). Normal distribution was verified by Shapiro-Wilk test. (**S**) Schematic representation of the experimental setup. MUP-core mice were lethally irradiated and reconstituted with WT or Tap1$^{-/-}$ bone marrow (BM). Eight weeks after BM reconstitution mice received two injections of clodronate liposomes (CLL) to remove residual radio-resistant KCs. Two weeks after the last dose of CLL, 5 x 10^6*

*Cor93 T_N were transferred. Indicated mice received IL-2c one day after Cor93 T cell transfer. Livers were collected and analyzed five days after Cor93 T_N transfer. (**T**-**U**) Total numbers (**T**) and numbers of IFN-γ-producing (**U**) Cor93 T cells in the livers of the indicated mice. (MUP-core WT-PBS, n = 3; MUP-core WT-IL-2c, n = 4; MUP-core Tap1$^{-/-}$-PBS, n = 4; MUP-core Tap1$^{-/-}$-IL-2c, n = 4) ** p value < 0.01, *** p value< 0.001, two-way ANOVA with Sidak's multiple comparison test. Data are representative of at least 3 independent experiments. (De Simone et al. Immunity 2021).*

10.7. Single-cell RNA-seq identifies two distinct populations of KCs among liver-resident macrophages

Next, we asked whether we could identify a distinct subpopulation of KCs more responsive to IL-2-responsive and find tools to increase or deplete it.

To this end, we employed high-dimensional single-cell RNA-sequencing to characterize KC heterogeneity at steady state. We FACS-sorted live CD45^{+} Lineage^{-} CD64^{+} F4/80^{+} liver macrophages from WT mice, isolated RNA and generated transcriptional profiles for each cell (n = 169) using the Smart-seq2 pipeline[78] (Fig. 20 A). When we analyze the dataset we identified 4 main cell clusters that we visualized using the uniform manifold approximation and projection (UMAP)[77] (Fig. 20 B). Cluster 0 (n = 68) and cluster 1 (n = 59) cells showed higher expression of classical KC-associated gene markers, such as Clec4f, Lyz2 and Csf1r. Pathway analysis of their respective gene markers yielded immunological pathways and processes typical of macrophages and professional APCs and were thus considered bona fide KCs.

Cells in cluster 2 (n = 30) expressed genes such as Cd34, Cd209c and Fgd4 but low levels of macrophage genes, while amongst their specific markers we found a high number of ribosomal and non-coding genes.

They also showed a lower number of transcripts detected per cell and a higher percentage of mitochondrial genes, indicating a high fraction of apoptotic cells in this population, and hence were excluded from subsequent analyses.

Cells in cluster 3 (n = 12) expressed genes associated to endothelial cells including Pecam1 (CD31), Clec4g, Lyve1, Kdr (VGFR2); in addition, their specific markers were enriched in endothelial cells processes, arguing for contamination of sorted cells with LSECs. Although both cluster 0 and cluster 1 showed expression of KC markers, they were clearly distinguished by the expression of many genes. Of note, when compared to cells in cluster 0, we found that cells in cluster 1 were enriched in genes associated to Ag processing, cross-presentation and IL-2 signaling pathway (Fig. B-F).

Among the differentially expressed genes, we initially focused on Mrc1 (CD206) and Lamp2 (CD107b) as a first approach to identify and FACS-sort the two KC populations, then an *ad interim* bulk RNA-seq analysis of the two populations revealed Esam (ESAM) as highly differentially expressed gene.

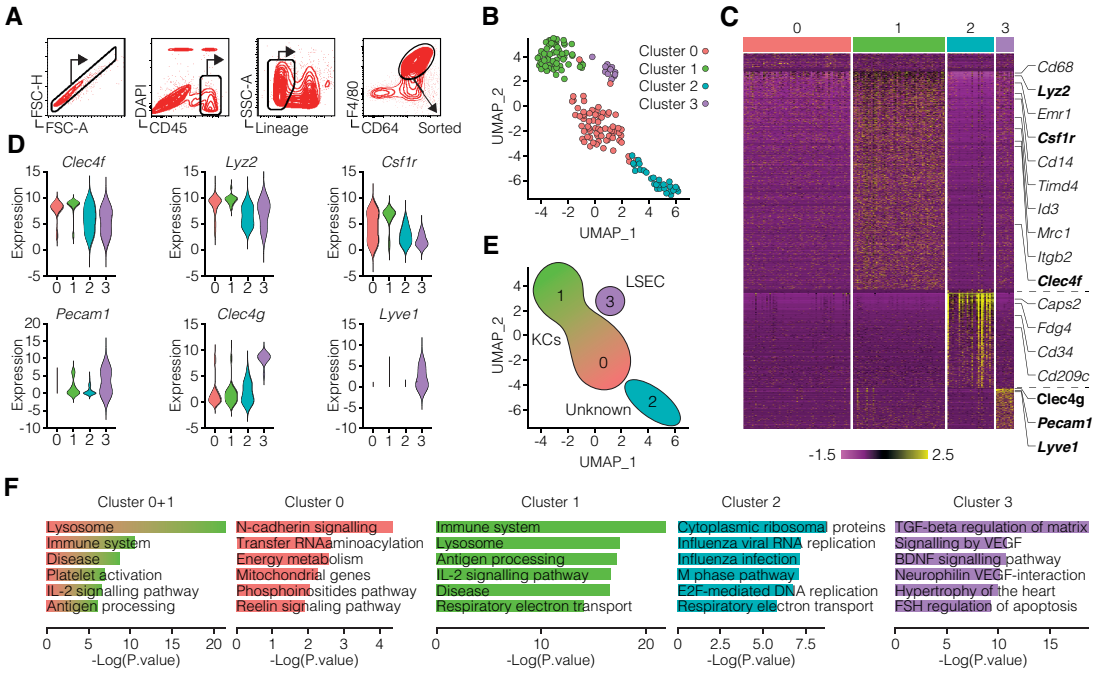

Figure 20. *Single-cell RNA-seq identifies two distinct populations of KCs among liver-resident macrophages.*

*(**A**) Sorting strategy for liver macrophages. Liver macrophages are defined as live, CD45^{+}, Lineage^{-} (CD3, CD19, Ly6G, CD49b), CD64^{+}, F4/80^{+} cells. (**B**) UMAP projection of sorted cells. Each dot corresponds to a single cell, colored according to the unbiased clusters identified: cluster 0 (red, 68 cells), cluster 1 (green, 59 cells), cluster 2 (blue, 30 cells) and cluster 3 (purple, 12 cells). (**C**) Heatmap of normalized and scaled expression values of the 2,811 marker genes identifying the four clusters. Genes highlighted on the right are representative of each cluster. Color coding of the bar on the top of the heatmap as in (B). (**D**) Violin plots showing the normalized expression profile of selected genes differentially expressed in the four clusters. (**E**) Cell type annotation of the four clusters based on the identified markers. (**F**) Pathway analysis of each cluster. Enriched pathways (BioPlanet 2019) are ordered by p value and the most biologically informative among the top 10 are shown. (De Simone et al. Immunity 2021).*

10.8. A KC subset with enriched IL-2 sensing machinery and Ag presentation capacity can be identified

Based on these data, we designed a panel of markers for use in conventional flow cytometry to identify and sort these KC subpopulations and validate the high-throughput transcriptomic approach.

Based on surface marker expression, we observed that $CD45^+$ $F4/80^+$ $CD11b^{int}$ $TIM\text{-}4^+$ KC population was split into $CD206^-ESAM^-$ (hereafter KC1, ~70-85% of total KCs) and $CD206^+ESAM^+$ (hereafter KC2, ~15-30% of total KCs) cells.

Using the same surface markers, we also performed confocal imaging analyses that confirmed the presence of two distinct KC subpopulations (Fig. 21 A-C). Importantly, RNA-seq analyses on bulk KC1 and KC2 sorted from WT mice confirmed that KC2 are enriched in IL-2 signaling components, such as IL-2 receptor subunits and molecules implicated in intracellular signal transduction. Higher expression of the IL-2 receptor subunits, MHC-I, and co-stimulatory molecules in KC2 was also confirmed at the protein level by FACS analysis (Fig. 21 D-F).

Together, the data suggest that KC2 are better equipped than KC1 to respond to IL-2 and increase their capacity to cross-present hepatocellular Ags.

Thus, one might predict that IL-2 treatment might render KC2 a preferential target compared to KC1 for $CD8^+$ effector cell-mediated killing; to test this hypothesis, we treated HBV replication competent transgenic mice with IL-2c 24 hours after Cor93 T_N injection and checked the KC1/KC2 ratio 4 days later.

Consistent with the previous hypothesis, we found that KC2 almost completely disappeared in Cor93 T cell-injected HBV transgenic mice treated with IL-2c (Fig. 21 K-N).

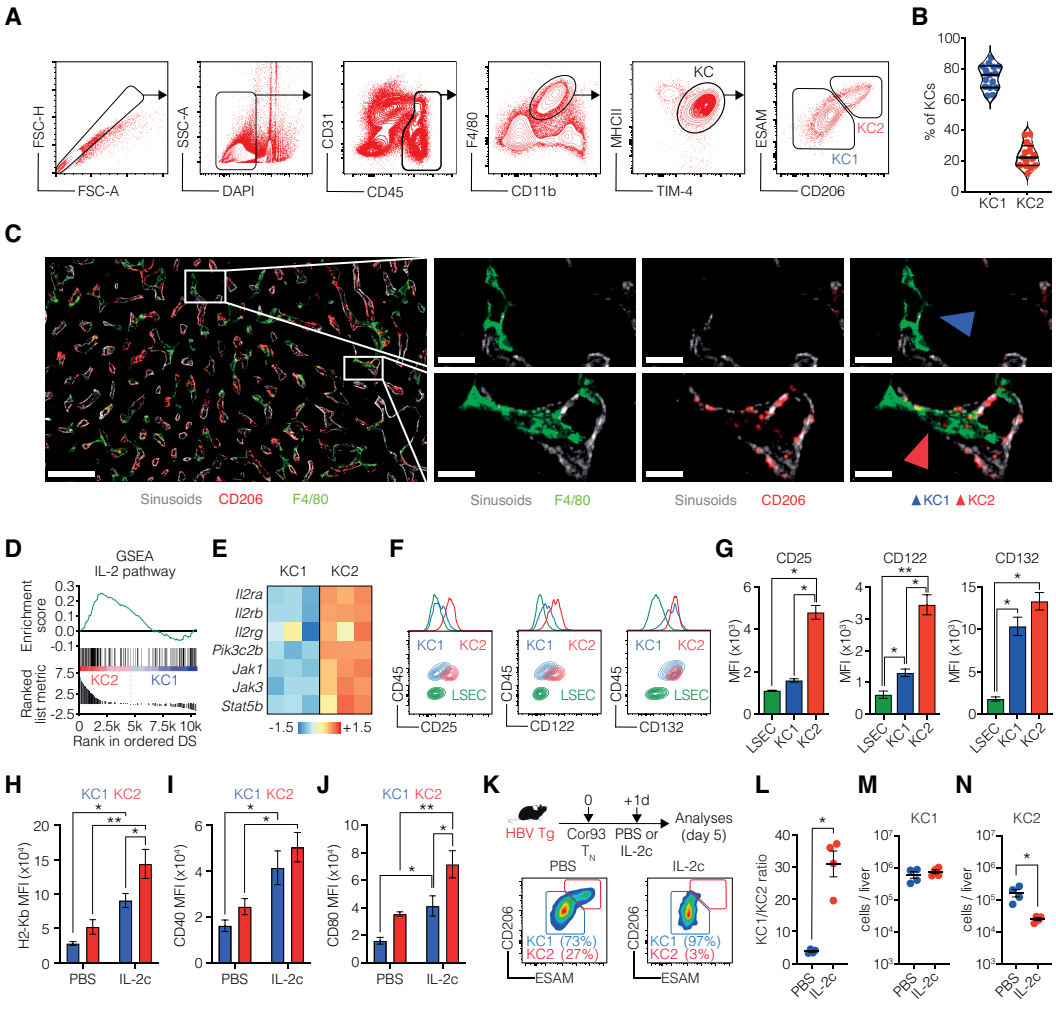

Figure 21. *Identification of a KC subset with enriched IL-2 sensing machinery.*

*(**A**) Representative flow cytometry plot of KC1 and KC2 gating strategy. KCs are identified as live, CD45$^+$, CD11b^{int}, F4/80$^+$, MHCII$^+$, TIM4$^+$ liver non-parenchymal cells. KC1 are defined as ESAM$^-$ CD206$^-$ KCs. KC2 are defined as ESAM$^+$ CD206$^+$ KCs. (**B**) Relative representation of KC1 and KC2 percentages in the liver of C57BL/6 mice (n = 15). (**C**) Representative confocal immunofluorescence micrographs of liver sections from C57BL/6 mice. Sinusoids were identified as CD38$^+$ cells and are depicted in white. CD206$^+$ cells are depicted in red, F4/80$^+$ cells in green. Scale bars represent 50 µm or 10 µm (See also **Movie S1**). (**D**) GSEA relative to the IL-2 pathway enrichment in KC2 (red) and KC1 (blue) samples. Genes were pre-ranked based on the Log2 Fold Change between KC2 and KC1. (**E**) Heatmap representing the relative expression of the IL-2 receptor signaling components in KC1 and KC2 isolated from C57BL/6 mice (n = 3 per group). Values in log2TPM were scaled by row across samples (Z-score). (**F-G**) Representative flow cytometry plots (**F**) and MFI (**G**) of CD25, CD122 and CD132 expression in KC1, KC2 and LSEC (defined as live, CD45$^-$, CD31$^+$ cells) in C57BL/6 mice (n = 3 per group). * p value< 0.05, ** p value< 0.01, two-way ANOVA with Sidak's multiple comparison test. (**H-J**) MFI of H2-Kb (**H**), CD40 (**I**) and CD80 (**J**) expression on KC1 (blue) and KC2 (red) 48h after PBS or IL-2c treatment in vivo (n = 3 per group). * p value< 0.05, ** p value< 0.01, two-way ANOVA with Sidak's multiple comparison test. Test is performed comparing PBS vs IL-2c treatment and KC1 vs KC2. (**K**) Schematic representation of the experimental setup. HBV Tg mice were injected with 1 x 10^6*

*Cor93 T_N cells. Mice were treated with PBS or IL-2c one day after Cor93 T_N transfer. Livers were collected and analyzed five days after T_N transfer. Representative flow cytometry plots (bottom) of KC1 and KC2 in the livers upon PBS (left) or IL-2c (right) treatment. (**L-N**) Ratio between KC1 and KC2 (**L**) and absolute numbers of KC1 (**M**) and KC2 (**N**) in the liver of PBS (blue) or IL-2c (red) treated mice. (n = 4). * p value< 0.05, one-tailed Mann-Whitney U-test. Data are representative of at least 3 independent experiments. (De Simone et al. Immunity 2021).*

Notably, neither IL-2c treatment alone (in the absence of Cor93 T_N transfer) nor severe liver inflammation (induced by Cor93 T_E) altered the KC1/KC2 ratio (Fig. 22).

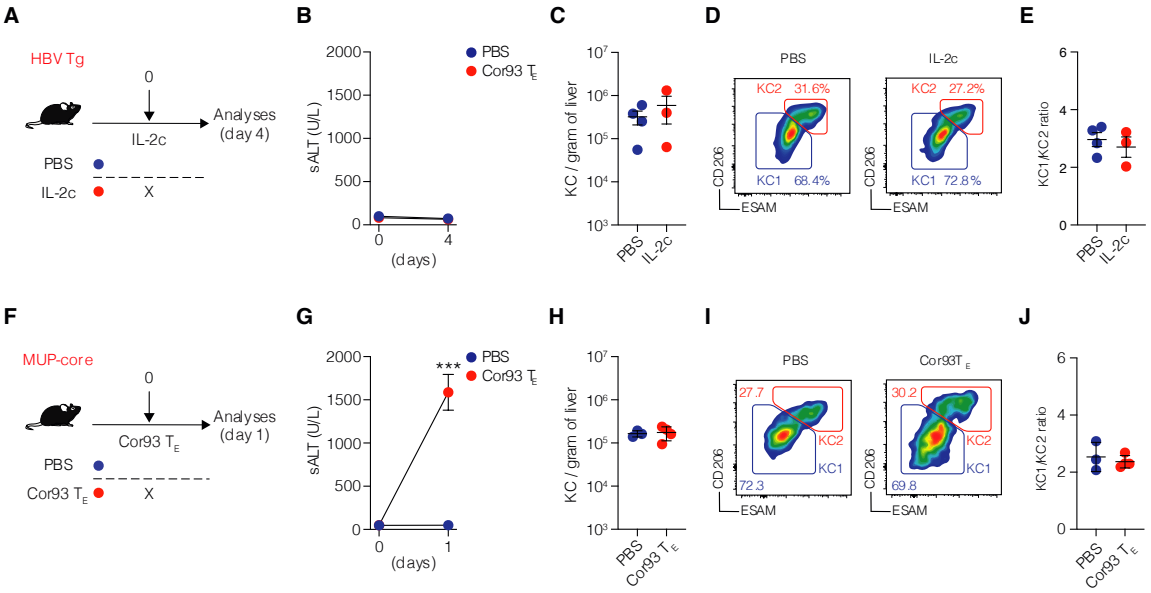

Figure 22. *IL-2c treatment alone or liver inflammation have no impact on KC1/KC2 ratio, Related to Figure 4*

*(**A**) Schematic representation of the experimental setup. HBV Tg mice were treated with PBS or IL-2c and livers were collected and analyzed four days after treatment. (**B**) Levels of ALT in the serum of the indicated mice at the indicated timepoints. (**C**) Numbers of KCs (identified as live, $CD45^+$, $F4/80^+$, $TIM4^+$ cells) per gram of liver in the indicated mice.*
*(**D**) Representative flow cytometry plots of KC1 ($CD206^-$ $ESAM^-$) and KC2 ($CD206^+$ $ESAM^+$) in the indicated mice. (**E**) KC1/KC2 ratio in the indicated mice (PBS, n = 4; IL-2c, n = 3).*
*(**F**) Schematic representation of the experimental setup. MUP-core mice were injected with PBS or Cor93 T_E. Livers were collected and analyzed one day after T cell transfer. (**G**) Levels of ALT in the serum of indicated mice at the indicated timepoints.*
*(**H**) Numbers of KCs per gram of liver in the indicated mice. *** p value< 0.001, two-way ANOVA with Sidak's multiple comparison test. (**I**) Representative flow cytometry plots of KC1 ($CD206^-$ $ESAM^-$) and KC2 ($CD206^+$ $ESAM^+$) in the indicated mice. (**J**) KC1/KC2 ratio in the indicated mice (PBS, n = 3; Cor93 T_E, n = 3). Data are representative of at least 2 independent experiments. (De Simone et al. Immunity 2021).*

10.9. KC2 are required for the optimal restoration of intrahepatically-primed, dysfunctional CD8+ T cells by IL-2

We next took advantage of the observation that KC2 (but not KC1) express the endothelial cell marker VEcadherin (encoded by Cdh5) to generate a mouse model where KC2 could be selectively depleted to assess their role in the cross-presentation of hepatocellular Ags upon in vivo IL-2 treatment.

This was achieved by: 1) injecting $Cdh5^{CreERT2}$; $Rosa26^{iDTR}$ bone marrow into irradiated MUP-core mice; 2) depleting the residual radio-resistant KCs; 3) inducing DTR expression in KC2 by tamoxifen administration and, finally, 4) depleting KC2 by DT injection (Fig. 23 A-E).

After generating KC2 deficient mice, we proceeded to transfer Cor93 T_N and to treat mice with IL-2c. We observed that Cor93 T cells in KC2 deficient mice have a lower ability to proliferate and differentiate into T_E in response to IL-2c. The functional impairment of IL-2 action was also reflected by the reduction of intra-parenchymal accumulation and increased clustering around the portal tracts (Fig. 23 I-L).

These data reinforce the idea that KC2 are required for the optimal reinvigoration of intrahepatically primed T cells by IL-2.

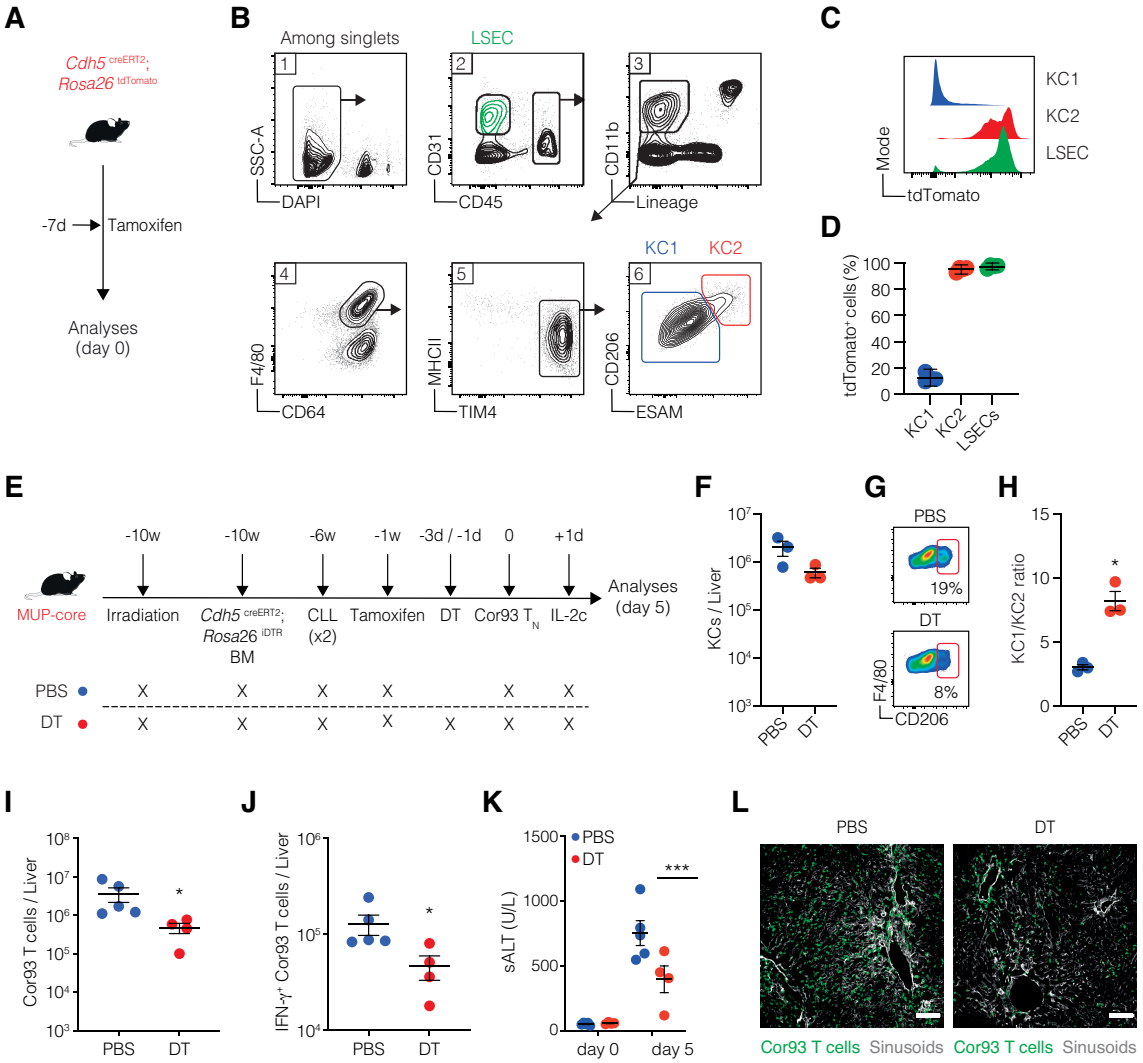

Figure 23. *KC2 are required for the optimal restoration of intrahepatically-primed, dysfunctional CD8⁺ T cells by IL-2.*

*. **(A)** Schematic representation of the experimental setup. Cdh5 ^{CreERT2}; Rosa26 ^{tdTomato} mice were treated with tamoxifen and livers were collected and analyzed 7 days after treatment. **(B)** Gating strategy for KC1, KC2 and LSECs. **(C-D)** Representative histograms **(C)** and percentage **(D)** of tdTomato expression on of KC1 (blue) and KC2 (red) and LSECs (green) (n = 3). **(E)** Schematic representation of the experimental setup. MUP-core mice were lethally irradiated and reconstituted with Cdh5^{creERT2}; Rosa26^{iDTR} bone marrow (BM). Four weeks later mice received two injections of clodronate liposomes (CLL) to remove residual radio-resistant KCs. Nine weeks after BM reconstitution, mice were treated once with 5 mg of Tamoxifen by oral gavage. Mice were treated with diphtheria toxin (DT) every 48h starting three days before Cor93 T_N injection (1 x 10^6 cells/mouse). Indicated mice received IL-2c one day after Cor93 T_N transfer. Livers were collected and analyzed five days after Cor93 T_N transfer. **(F)** absolute numbers of total KCs (defined as live, CD45⁺, TIM4⁺, F4/80⁺ cells) in the liver of PBS (blue) or DT (red) treated mice. **(G)** Representative flow cytometry plots of KC1 (CD206⁻ KCs) and KC2 (CD206⁺ KCs) populations gated on total KCs (live, CD45⁺, TIM4⁺, F4/80⁺ cells) in the liver of the indicated mice at the time of T_N injection. **(H)** Ratio between KC1 and KC2 in the liver of PBS (blue) or DT (red) treated mice. n = 3. * p value< 0.05, one-tailed Mann-Whitney U-test. **(I-L)** Total numbers*

*(**I**) and numbers (**J**) of IFN-γ-producing Cor93 T cells in the livers of the indicated mice. PBS, n = 5; DT, n = 4. * p value< 0.05, two-tailed Mann-Whitney U-test. (**K**) Values of ALT in the serum of the indicated mice at the indicated timepoints. PBS, n = 5; DT, n = 4. *** p value< 0.001, two-way ANOVA with Sidak's multiple comparison test. (**L**) Representative confocal immunofluorescence micrographs of liver sections from the indicated mice five days after Cor93 T_N transfer. Cor93 T cells were identified as CD45.1$^+$ cells and are depicted in green. Sinusoids were identified as CD38$^+$ cells and are depicted in gray. Scale bars represent 100 μm. Data are representative of 2 independent experiments. (De Simone et al. Immunity 2021).*

11. DISCUSSION

In this work we have studied the dynamics of T_N priming in the liver using functional, transcriptomic, and imaging approaches. We showed that T cells primed by hepatocytes differentiate into dysfunctional cells while APCs lead to T cell effector differentiation, partially answering the dichotomic behavior of the liver as capable of supplying both immunosuppressive and immuno-stimulatory environment.

On one hand, we observed that T cells primed by liver APCs are similar to those primed in secondary lymphoid organs both in terms of functional cytotoxic activity and transcriptomic profile.

On the other hand, cells undergoing priming on hepatocytes show similarities both in function and gene expression profiles with anergic and exhausted $CD8^+$ T cells. However, when we compared the transcriptomic profile of Cor93 T cells isolated from MUP-core mice at late timepoints (e.g. D5), we observed that they actually show a unique gene expression profile, that we called "dysfunctional", which seems to render theme more prone to a tissue remodeling function rather than an anti-viral one.

Taken together, one can speculate that during the natural course of HBV infection, the two phenotypes co-exist and cooperate to viral clearance without causing tissue disruption.

We also showed that hepatocellularly primed T cells progressively acquire a phenotype that renders them refractory to anti-PD-1 treatment.

PD-1 treatment has been extensively studied as successful checkpoint inhibitor therapy for cancer patients, in which terminally exhausted CD8 T cells were reinvigorated in order to kill cancerous cells. Our observation that dysfunctional cells are refractory to anti-PD1 inhibition could be explained by the fact that their transcriptome is not completely overlapping to the one of exhausted cells in cancer, rendering them a less suitable target for the treatment.

Moreover, as shown by Huang et al. [79], PD-1 therapy loses its efficacy once the cell has been profoundly imprinted with an exhausted epigenetic profile. As we showed in our experiment, also Cor93 T cells in MUP-core mice are progressively acquiring an epigenetic imprinting that is reinforcing their phenotype during time and that is then rendering them refractory to further stimuli.

On the other hand, the lack of upregulation of IL-2 related genes made us identify IL-2 as a key to revert the dysfunctional phenotype and to acquire effector functions.

We have also outlined the molecular mechanisms by which IL-2 is acting on the liver environment: for the first time we showed that Kupffer Cells are able to sense IL-2 and pick up antigen from hepatocytes to present to T cells.

We showed that a sub-population of KCs (namely KC2) is more sensitive to IL-2 sensing and thus can be a starting point for targeted IL-2 based immunotherapy strategies.

Noteworthy, many points need to be still addressed.

First, we still do not have a clear idea of the role of DCs for T cell reinvigoration.

Although DCs are the main antigen cross-presenting cells in secondary lymphoid organs[80], they lack of a functional IL-2 receptor[81] and this might partially explain the reason why they are not required for IL-2 mediated dysfunctional T cell reinvigoration in the liver. Moreover, DCs reside mainly around the portal tract and outside the sinusoids, while KCs are located inside the vessel and extend protrusions in the space of Disse[82]: their different localization respect to DCs and the close contact between them and circulating naïve T cells might favor T cell priming on KCs.

However, we still do not have a clear picture of the precise dynamics of T cell priming during HBV infection. The common dogma of immune response would suggest that naïve T cells would reach secondary lymphoid organs, in which they would be cross primed by APCs loaded with viral antigens uptaken from circulating virions. This priming would result in the differentiation of T cells into T_E capable to migrate to the liver and kill infected hepatocytes.

In this sense, we still lack evidence that support (or exclude) a direct involvement of secondary lymphoid organs in the case of hepatotropic infections. However, based on the results of this work, we can assume that hepatocellular priming results in a functional impairment of the $CD8^+$ T cell response, contributing to the establishment of a chronic infection rather than supporting an acute response. Nevertheless, knowing that KC2 can effectively promote effector T cell differentiation, one might speculate that during an acute infection and in the presence of high IL-2, the liver could promote also an active immune response mediated by KC2 cross-presentation.

Another point that is worth discussing is the putative source of IL-2.

One of the possible candidates for this role could be the pool of effector $CD4^+$ T cells.

Data in chimpanzees and data from liver biopsies collected from chronically infected HBV patients indeed suggest that effector $CD4^+$ T cells play a critical role in the resolution of the infection and might be incisive on the clinical outcome of the patients[60]. Since the connection between $CD4^+$ T cells and KC2 stimulation linked to dysfunctional T cell reinvigoration has never been studied yet, there is still the need of a deep characterization.

Based on the results presented here, it is tempting to speculate that an effective immune response against HBV needs the presence of high local concentration of IL-2 at the time and location in which $CD8^+$ T cells intrahepatic priming occurs, in order to increase KC cross-presentation and lead to $CD8^+$ T cells activation. For these reasons we are in the process to generate $CD4^+$ T cells specific for HBsAg and inject them in 1.3.32 Tg mice together with Cor93 T_N to evaluate their capacity to i) produce IL-2 after Ag-recognition; ii) promote the effector function of Ag-specific naïve $CD8^+$ T cell that undergoes intrahepatic priming.

Taken together all the data suggest investing on IL-2 based therapeutic strategies for chronic HBV infection. Immunotherapies based on IL-2 have being long used for the treatment of different types of cancer (such us melanoma and renal carcinoma) and we know they are accompanied by severe side effects[83]. Finding tools that specifically target IL-2 to KC2 might overcome the potential systemic toxicity of these therapies. Such strategies might include liposomes or nanoparticle-based formulations targeting KC2-expressed surface Ags as well as lentiviral vectors[77].

12. MATERIAL AND METHODS

The following data have been published (*Bénéchet, De Simone et al. Nature 2019; De Simone et al. Immunity 2021*).

Mice

C57BL/6, CD45.1 (inbred C57BL/6), Balb/c, Thy1.1 (CBy.PL(B6)-*Thy*^{a}/ScrJ), β-actin-GFP [C57BL/6-Tg(CAG-EGFP)1Osb/J], Ai14(RCL-tdT)-D [B6.Cg-Gt(ROSA)26Sortm14(CAG-tdTomato)Hze/J], β-actin-DsRed [B6.Cg-Tg(CAG-DsRed*MST)1Nagy/J], *Tap1*$^{-/-}$ (B6.129S2-*Tap1*^{tm1Arp}/J), CD11c^{DTR} [B6.FVB-*1700016L2Rik*$^{Tg(Itgax-DTR/EGFP)57Lan}$/J], ROSA26^{iDTR} [C57BL/6-Gt(ROSA)26Sortm1(HBEGF)Awai/J], Cdh5^{CreERT2} [Tg(Cdh5-cre/ERT2)1Rha] mice were purchased from Charles River or The Jackson Laboratory. MUP-core transgenic mice (lineage MUP-core 50 [MC50], inbred C57BL/6, H-2^{b}), that express the HBV core protein in 100% of the hepatocytes under the transcriptional control of the mouse major urinary protein (MUP) promoter, have been previously described (Guidotti et al., 1994). HBV replication-competent transgenic mice (lineage 1.3.32, inbred C57BL/6, H-2^{b}), that express all the HBV Ags and replicate HBV in the liver at high viral copies without any evidence of cytopathology, have been previously described (Guidotti et al., 1995). In indicated experiments, MUP-core and HBV replication-competent transgenic mice were used as C57BL/6 x Balb/c H-2^{bxd} F1 hybrids. Cor93 TCR transgenic mice (lineage BC10.3, inbred CD45.1), in which > 98% of the splenic CD8^{+} T cells recognize a K^{b}-restricted epitope located between residues 93-100 in the HBV core protein (MGLKFRQL), have been previously described (Isogawa et al., 2013). Env28 TCR transgenic mice (lineage 6C2.36, inbred Thy1.1 Balb/c), in which ∼83% of the splenic CD8^{+} T cells recognize a L^{d}-restricted epitope located between residues 28–39 of HBsAg (IPQSLDSWWTSL), have been previously described (Isogawa et al., 2013). For imaging experiments Cor93 transgenic mice were bred against β-actin-GFP, while Env28 transgenic mice were bred against β-actin-DsRed mice (inbred Balb/c). Bone marrow (BM) chimeras were generated by irradiation of MUP-core or C57BL/6 mice with one dose of 900 rad and reconstitution with the indicated BM; mice were allowed to reconstitute for at least 8 weeks before experimental manipulations. Mice were housed under specific pathogen-free conditions and entered experiments at 8-10 weeks of age. In

all experiments, mice were matched for age, sex and (for the 1.3.32 animals) serum HBeAg concentration before experimental manipulations. All experimental animal procedures were approved by the Institutional Animal Committee of the San Raffaele Scientific Institute and are compliant with all relevant ethical regulations.

Viruses and viral vectors

Replication-incompetent LCMV-based vectors encoding HBV core and envelope proteins (rLCMV-core/env) were generated, grown, and titrated as previously described (Bénéchet et al., 2019). Mice were injected intravenously (i.v.) with 2.5×10^5 infectious units of rLCMV vector 4h before $CD8^+$ T cell injection. All infectious work was performed in designated BSL-2 or BSL-3 workspaces, in accordance with institutional guidelines.

Adeno-associated viruses expressing GFP and HBV core protein (AAV-core-GFP) have already been described[84]. Mice were injected with 3 x 10^{10} or 3 x 10^{11} viral genomes (vg) of AAV-core-GFP 15 days prior to further experimental manipulation.

Third-generation, self-inactivating lentiviral vectors (LV.ET.mIL2.142T) that allow expression of murine IL-2 exclusively in hepatocytes thanks to the presence of a synthetic hepatocyte-specific promoter/enhancer as well as specific microRNA 142 target sequences that suppress expression in hematopoietic-lineage cells[76] were generated, produced and titrated as described[85]. Briefly, the gene-synthesized murine interleukin 2 (mIL-2) cDNA was cloned into the previously described transfer vector pCCLsin.cPPT.ET.GFP.142T[85] by standard cloning techniques. Third-generation LVs were produced by calcium phosphate transient transfection of 293T cells of the transfer vector, the packaging plasmid pMDLg/p.RRE, pCMV.REV, the vesicular stomatitis virus glycoprotein G (VSV-G) envelope plasmid pMD2.G and the pAdvantage plasmid (Promega), as previously described[85]. For integrase-defective lentiviral vector (IDLV) production, the pMDLg/p.RRE.D64Vint packaging with a mutant integrase was used instead of pMDLg/p.RRE, as described[86]. Briefly, $9x10^6$ 293T cells were seeded 24 hours before transfection in 15-cm dishes. Two hours before transfection culture medium was replaced with fresh medium. For each dish, a solution containing a mix of the selected transfer plasmid, the packaging plasmids pMDLg/pRRE and pCMV.REV, pMD2.G and the pAdvantage plasmid was prepared using 35, 12.5, 6.25, 9 and 15 μg of plasmid DNA,

respectively. A 0.1X TE solution (10 mM Tris-HCl, 1 mM EDTA pH 8.0 in dH_20) and water (1:2) was added to the DNA mix to 1,250 µL of final volume. The solution was left on a spinning wheel for 20-30 minutes, then 125 µl of 2.5M $CaCl_2$ were added. Right before transfection, a precipitate was formed by adding 1,250 µL of 2X HBS (281 mM NaCl, 100 mM HEPES, 1.5 mM Na2HPO4, pH 7.12) while the solution was kept in agitation on a vortex. The precipitate was immediately added to the culture medium and left on cells for 14-16 hours and after that the culture medium was changed. Supernatant was collected 30 hours after medium change and passed through a 0.22 µm filter (Millipore). Filtered supernatant was transferred into sterile 25 x 89 mm polyallomer tubes (Beckman) and centrifuged at 20,000g for 120 min at 20°C (Beckman Optima XL-100K Ultracentrifuge). Vector pellet was dissolved in the appropriate volume of PBS to allow a 500X concentration. For LV titration, 10^5 293T cells were transduced with serial vector dilutions in the presence of polybrene (16 µg/ml). Genomic DNA (gDNA) was extracted 14 days after transduction. gDNA was extracted by using Maxwell 16 Cell DNA Purification Kit (Promega) according to manufacturer's instructions. Vector copies per diploid genome (vector copy number, VCN) were quantified by quantitative PCR (qPCR) starting from 100 ng of template gDNA using primers (HIV sense: 5'-TACTGACGCTCTCGCACC-3'; HIV antisense: 5'-TCTCGACGCAGGACTCG-3') and a probe (FAM 5'-ATCTCTCTCCTTCTAGCCTC-3') designed to amplify the primer binding site region of LV. Endogenous DNA amount was quantified by a primers/probe set designed to amplify the human telomerase gene (Telo sense: 5'-GGCACACGTGGCTTTTCG-3'; Telo antisense: 5'-GGTGAACCTCGTAAGTTTATGCAA-3'; Telo probe: VIC 5'-TCAGGACGTCGAGTGGACACGGTG-3' TAMRA). Copies per genome were calculated by the formula = [ng LV/ng endogenous DNA] x [n° of LV integrations in the standard curve]. The standard curve was generated by using a CEM cell line stably carrying 4 vector integrants, which were previously determined by Southern blot and FISH analysis. All reactions were carried out in duplicate or triplicate in an ABI Prism 7900HT or Viia7 Real Time PCR thermal cycler (Applied Biosystems). Each qPCR run carried an internal control generated by using a CEM cell line stably carrying 1 vector integrant, which were previously determined by Southern blot and FISH analysis. Titre is expressed as transducing $units_{293T}$ (TU)/mL and calculated using the formula TU/mL

= [VCNx10^5x1/dilution factor]. IDLV titre was determined on 293T cells 3 days after transduction using an ad hoc qPCR, which selectively amplifies the reverse transcribed vector genome (both integrated and non-integrated) discriminating it from plasmid carried over from the transient transfection (RT-LV; ΔU3 sense: 5'-TCACTCCCAACGAAGACAAGATC-3', gag antisense: 5' GAGTCCTGCGTCGAGAGAG-3'). Vector particles were measured by HIV-1 Gag p24 antigen immunocapture assay (Perkin Elmer) according to manufacturer's instructions. Vector infectivity was calculated as the ratio between titre and particles. Vector administration was carried out by tail vein injection in mice at 2.5-10x10^8 TU/mouse, 7 days prior to T cell injection.

All infectious work was performed in designated BSL-2 or BSL-3 workspaces, in accordance with institutional guidelines.

Naïve T Cell Isolation, Adoptive Transfer, and *In Vivo* Treatments

$CD8^+$ T cells from the spleens of Cor93, Env28, TCR-I transgenic mice were purified by negative immunomagnetic sorting (Miltenyi Biotec). Mice were adoptively transferred with 2-5 x 10^6, 2 x $10^{5,}$ or 2 x 10^4 $CD8^+$ T cells. In selected experiments, mice were splenectomized and treated with 200 μg of anti-CD62L mAb (clone MEL-14, BioXcell) 48 hours and 4 hours prior to cell injection, respectively. Splenectomy was performed according to standard procedures[87]. In selected experiments, $CD4^+$ T cells were depleted by injecting i.v. 200 μg of anti-CD4 Ab (clone GK1.5, BioXcell) 3 days and 1 day prior to T cell transfer. In selected experiment, mice were treated with 200 μg of anti-PD-L1 (Clone 10F.9G2, BioXcell) 1 day before and 1 day and 3 days after T cell transfer. In some experiments, Tregs were depleted by injecting i.p. 200 μg of purified anti-CD25 mAbs (clone PC61, BioXcell) 8 days prior to T cell transfer.

Mice were adoptively transferred with 5 x 10^6 or 1 x 10^6 HBV-specific naïve $CD8^+$ TCR transgenic T cells isolated from the spleens of Cor93 and/or Env28 TCR transgenic mice, as described (Bénéchet et al., 2019). IL-2/anti-IL-2 complexes (IL-2c) were prepared by incubating 1.5 μg of rIL-2 (R&D Systems) with 50 μg anti-IL-2 mAb (clone S4B6-1, BioXcell) per mouse, as previously described (Boyman et al., 2006). Mice were injected with IL-2c intraperitoneally (i.p.) one day after T cell transfer, unless otherwise indicated.

In indicated experiments, naïve $CD8^+$ T cells from the spleens of Cor93 TCR transgenic mice were differentiated *in vitro* for 7-9 days into effector cells prior to adoptive transfer (1×10^7 cells), or *in vitro* co-culture, as described (Bénéchet et al., 2019; Guidotti et al., 2015). In indicated experiments, Kupffer cells (KCs) were depleted by intravenous injection of 200µl of clodronate-containing liposomes (Liposoma) 2 days prior to T cell injection, as described (Bénéchet et al., 2019), unless otherwise indicated. In indicated experiments, mice were injected i.p. with 200 µg of anti-Ly6G depleting antibody (clone 1A8, BioXcell) one day before and one day after T cell transfer. In indicated experiments, mice were injected intravenously (i.v.) with 200 µg of anti-Gr1 depleting antibody (clone RB6-8C5, BioXcell) every 48h starting from 3 days before T cell transfer. In indicated experiments, C57BL/6 or MUP-core mice were lethally irradiated and reconstituted for at least 8 weeks with BM from CD11c-DTR mice; dendritic cells were subsequently depleted by injecting i.p. 20 ng per gram of mouse of diphtheria toxin (Millipore) every 48h starting from 3 days before T cell transfer. In indicated experiments, MUP-core mice were lethally irradiated and reconstituted for at least 8 weeks with BM from C57BL/6 or *Tap1*$^{-/-}$ mice. To achieve full reconstitution of Kupffer cells from donor-derived BM, mice were injected with 200µl of clodronate-containing liposomes 28 and 31 days after BM injection. In indicated experiments, MUP-core mice were lethally irradiated and reconstituted for at least 8 weeks with BM from *Cdh5*^{CreERT2}; Rosa26^{iDTR}; Rosa26^{tdTomato}; CX3CR1^{GFP} mice. To achieve full reconstitution of Kupffer cells from donor-derived BM, mice were injected with 200µl of clodronate-containing liposomes 28 and 31 days after BM injection. To induce the expression of the Cre recombinase, mice were treated with 5 mg of Tamoxifen (Sigma) by oral gavage in 200 µl of corn oil one week before further manipulations. KC2 were depleted subsequently by injecting i.p. 20 ng per gram of mouse of diphtheria toxin (Millipore) 3 days and 1 day prior to T cell transfer.

Cell Isolation and Flow Cytometry

Single-cell suspensions of liver, spleen and blood were generated as described (Bénéchet et al., 2019). Kupffer cell isolation was performed as described (Bénéchet et al., 2019). All flow cytometry stainings of surface-expressed and intracellular molecules were performed as described (Giovanni et al., 2020). Cell viability was assessed by staining with Viobility™ 405/520 fixable dye (Miltenyi, #130-109-816), LIVE/DEAD™

Fixable Far-Red dye (Invitrogen, # L34973) or DAPI (Invitrogen, # D1306). Abs used included: anti-CD3 (clone: 145-2C11, Cat#562286, BD Biosciences), anti-CD4 (clone: RM4-5, Cat #48-0042-82, eBioscience), anti-CD8a (clone: 53-6.7, Cat# 558106, BD Biosciences), anti-CD11b (clone: M1/70, Cat#101239), anti-CD19 (clone: 1D3, Cat#562291 BD Biosciences), anti-CD25 (clone: PC61, Cat#102015), anti-CD31 (clone: 390, Cat#102427), anti-CD45 (clone: 30-F11, Cat#564279 BD Biosciences), anti-CD64 (clone: X54-5/7.1, Cat#139311), anti-F4/80 (clone: BM8, Cat#123117), anti-I-A/I-E (clone: M5/114.15.2, Cat#107622), anti-TIM4 (clone: RTM4-54 Cat#130010), anti-TIM4 (polyclonal, Cat#orb103599 Biorbyt), anti-CD69 (clone: H1.2F3, Cat# 104517), anti-CD45.1 (clone: A20, Cat#110716), anti-IFN-γ (clone: XMG1.2, Cat# 557735 BD Biosciences), anti-CD11c (clone: N418, Cat# 117308), anti-I-Ab (clone: AF6-120.1, Cat# 116420), anti-Stat5 pY694 (clone: 47, Cat# 612599 BD Biosciences), anti-Foxp3 (clone FJK-16s, Cat#25-5773-82 Thermofisher), anti-CD122 (clone TM-B1 Cat#123210), anti-CD132 (clone TUgm2 Cat#132306), anti-CD40 (clone 3/23 Cat#558695 BD Biosciences), anti-CD80 (clone 1610A1 Cat#553769 BD Biosciences), anti-H2-K^b (clone AF6-88.5 Cat#742861 BD Biosciences), anti-ESAM (clone 1G8/ESAM, Cat#136203), anti-CD206 (clone C068C2, Cat#141712), anti-Ly6G (clone 1A8, Cat #562700 BD Biosciences), anti-Ly6C (clone HK1.4, Cat# 128008), anti-CD49b (clone DX5, Cat#562453 BD Biosciences), anti CD107b (clone M3/84, Cat #12-5989-82 eBioscience). All Abs were purchased from BioLegend, unless otherwise indicated. Recombinant dimeric H-$2L^d$:Ig and H-$2K^b$:Ig fusion proteins (BD Biosciences) complexed with peptides derived from HBsAg (Env28-39) or from HBcAg (Cor93-100), respectively, were prepared according to the manufacturer's instructions. Dimer staining was performed as described (Iannacone et al., 2005). Flow cytometry staining for phosphorylated STAT5 was performed using Phosflow™ Perm Buffer III (BD Bioscience), following the manufacturer's instructions. Flow cytometry staining for Foxp3 was performed using Foxp3/Transcription Factor Staining Buffer Set (eBioscience), following the manufacturer's instructions. In indicated experiments, cells were stained with CellTrace™ Violet cell proliferation kit (CTV, Invitrogen), following manufacturer's instructions. All flow cytometry analyses were performed in FACS buffer containing PBS with 2 mM EDTA and 2% FBS on a FACS CANTO II (BD Bioscience) or CytoFLEX LX (Beckman Coulter) and analyzed with FlowJo software (Treestar).

Cell Sorting

For the experiments in described in **Fig. 15**, single-cell suspensions from spleens and livers were stained with Viobility 405/520 fixable dye (Miltenyi), with PB-conjugated anti-CD8α (clone 53-6.7) and PE-conjugated anti-CD45.1 Abs. Live $CD8^+$ $CD45.1^+$ cells were sorted on a MoFlo Legacy (Beckman Coulter) cell sorter in a buffer containing PBS with 2% FBS. Cells were always at least 98% pure (data not shown).

RNA Purification and RNA-seq Library Preparation

For the experiments in described in **Fig. 15,** total RNA was purified from 8,000-300,000 sorted cells with the ReliaPrep RNA Cell Miniprep System (Promega). Sequencing libraries were generated using the Smart-seq2 method[78]. Briefly, 5 ng of RNA were retrotranscribed and cDNA was amplified using 15 PCR cycles and purified with AMPure XP beads (Beckman Coulter). After purification, the concentration was determined using Qubit 3.0 (Life Technologies) and the size distribution was assessed using Agilent 4200 TapeStation system. Then, the tagmentation reaction was performed starting from 0.5 ng of cDNA for 30 minutes at 55°C and the enrichment PCR was carried out using 12 cycles. Libraries were then purified with AMPure XP beads, quantified using Qubit 3.0 and single-end sequenced (75 bp) on an Illumina NextSeq 500.

RNA-Seq Data Processing and Analysis

For the experiments in described in **Fig. 15,** reads were generated on a NextSeq 500 (Illumina) instrument following the manufacturer's recommendations. Single end reads (75bp) were aligned to the mm10 reference genome using STAR[88] aligner. `featureCounts` function from Rsubread package[89] was used to compute reads over RefSeq *Mus musculus* transcriptome, with option minMQS set to 255. Further analyses were performed with edgeR R package[90]. Pearson's correlation was computed for each couple of samples on log transformed RPKM. Read counts were normalized with the Trimmed Mean of M-values (TMM) method[91] using `calcNormFactors` function and dispersion was estimated with the `estimateDisp` function. Differential expression across different conditions was evaluated fitting a negative binomial generalized linear

model on the dataset with `glmQLFit` function and then performing a quasi-likelihood (QL) F-test with `glmQLFTest` function. Batch information was included in the design as covariate.

Differential Gene Expression Analysis

For the experiments in described in **Fig. 15.**

Hepatic CD8$^+$ T cells from WT mice injected with rLCMV-core versus MUP-core mice. Genes with an RPKM (Reads Per Kilobase per Million) value higher than 1 in at least two samples in the datasets were retained. We first defined inducible genes, namely those genes with $\log_2FC_{RPKM}$ >2.5 and FDR<0.01 relative to naïve T cells in at least one condition or time point. For each comparison, only genes with an RPKM value higher than 1 in at least two samples in the comparison were selected. For each time point, induced genes were classified as expressed at higher levels in the WT + rLCMV-core condition setting FDR < 0.1 and $\log_2FC_{RPKM}$ > 1.5 (WT + rLCMV-core vs MUP-core) as cut-offs. Genes with an FDR < 0.1 and a $\log_2FC_{RPKM}$ < -1.5 in the WT + rLCMV-core vs MUP-core comparison were classified as expressed at higher levels in MUP-core. The remaining genes were defined as non-differentially expressed between WT + rLCMV-core and MUP-core.

Hepatic or splenic CD8$^+$ T cells from WT mice injected with rLCMV-core versus Cor93 T_N. We first defined as expressed genes those having CPM > 1 in at least two samples in the dataset. Induced genes were defined using as cut-offs a $\log_2FC_{RPKM}$ > 2.5 and FDR < 0.01 relative to naïve T cells in at least one condition or time point. For each comparison, only genes with an RPKM value higher than 1 in at least two samples in the comparison were selected.

Hepatic CD8$^+$ T cells from WT mice injected with rLCMV-core versus MUP-core mice with or without IL-2c treatment. We first defined as expressed genes those having CPM > 1 in at least two samples in the dataset. Induced genes were defined using as cut-offs a $\log_2FC_{RPKM}$ > 2.5 and FDR < 0.01 relative to naïve T cells in at least one condition. For each comparison, only genes with an RPKM value higher than 1 in at least two samples in the comparison were selected. Induced genes were then classified as expressed at higher levels in the WT + rLCMV-core condition (hypo-expressed in MUP-core at day 5) setting $\log_2FC_{RPKM}$ > 1.5 and FDR < 0.01 (WT + rLCMV-core vs MUP-core) as cut-off. Genes with a $\log_2FC_{RPKM}$ < -1.5 and FDR < 0.01 in the WT + rLCMV-core vs MUP-

core comparison were classified as expressed at higher levels (hyper-expressed in MUP-core at day 5) in MUP-core. We then classified genes hypo-expressed in MUP-core as rescued if they displayed $log_2FC_{RPKM} > 1$ and FDR < 0.01 in the IL-2c-treated MUP-core versus MUP-core comparison. Conversely, genes hyper-expressed in MUP-core were defined as rescued if displaying $log_2FC_{RPKM} < -1$ and FDR < 0.01 in the IL-2c-treated MUP-core versus MUP-core comparison. The remaining genes were classified as not rescued.

Gene Ontology (GO) Analyses

For the experiments in described in **Fig. 15,** for each time point, we ranked expressed genes by decreasing order of log_2FC_{RPKM} values in the WT+rLCMV-core versus MUP-core comparison. We then performed Gene set enrichment analysis (GSEA)[92] on each of these ranked lists using the clusterProfiler R package[93] and the Gene Sets contained in the Biological Processes ontology from the org.Mm.eg.db database. GO categories with q-value < 0.1 were retained and aggregated using REVIGO[94] (similarity score=0.7), yielding 143 seed GO categories showing enrichment in WT+rLCMV-core or in MUP-core in at least one time point.

Gene Expression Analysis in Published Datasets

For the experiments in described in **Fig. 15**, RNA-seq/SRA data were downloaded from the Gene Expression Omnibus repository (GEO) and converted to the FastQ format. Reads were then aligned against the whole *Mus musculus* mm10 genome build using STAR aligner (v 2.6.0a) with default options, generating BAM files. Read counts for all expressed genes (Ensembl annotation v94; GENCODE M19) were obtained using featureCounts (Rsubread v 3.7). Features with < 1 CPM were filtered out. The resulting count matrix was then normalized using the normalization factors generated by the upperquartile method[95] implemented in edgeR Bioconductor package. Hierarchical cluster analysis was performed on RPKM values. The similarity of the samples was measured using the Pearson correlation coefficient and the complete-linkage was used as the distance measure of the agglomerative hierarchical clustering. For Illumina BeadChip data, the normalized expression matrix was downloaded from the GEO repository. Genes

whose expression level corresponded to the 65th percentile of the distribution of the log2 expression values were expressed.

ATAC-seq

For the experiments in described in **Fig. 15**ATAC (Assay for Transposase Accessible Chromatin)-seq was performed as described[96] with slight modifications. Briefly, 8,000-50,000 cells per sample were sorted and centrifuged at 1,600 rpm for 5 minutes. Then, the transposition reaction was performed using digitonin 1% (Promega), Tn5 transposase and TD Buffer (Illumina) for 45 minutes at 37°C. Immediately following transposition, the reaction was stopped using a solution of 900 mM NaCl and 300 mM EDTA, 5% SDS and Proteinase K (Sigma-Aldrich) for 30 minutes at 40°C. Transposed DNA fragments were purified using AMPure XP beads (Beckman Coulter), barcoded with dual indexes (Illumina Nextera) and PCR amplified with KAPA HiFi PCR Kit (KAPA Biosystems). Then, the concentration of the library was determined using Qubit 3.0 (Life Technologies) and the size distribution was assessed using Agilent 4200 TapeStation system. Libraries were single-end sequenced (75 bp) on an Illumina NextSeq 500.

ATAC-seq Data Processing and Analysis

Reads were generated on NextSeq 500 (Illumina) instrument following manufacturer's recommendations. Single end reads (75bp) were aligned to the mm10 reference genome using BWA[97] aligner. Bam files were processed using samtools[98] and BEDTools suits: reads with a mapping quality lower then 15 or duplicated were discarded. Moreover, unassigned reads and reads mapped on chromosomes Y and M were removed. MACS2[99] `callpeak` function with parameters `-g mm --nomodel --shift -100 --extsize 200` was used for peak calling. For each sample peaks with a q-value lower than 1e-10 were selected. Peaks from all samples that passed filter were then merged with `mergeBed` function form BEDTools, resulting in 72884 regions. Reads counts were computed on this set of regions using `coverageBed` function from BEDTools. The set of 72884 regions was annotated using ChIPpeakAnno R package[100]. Each region was associated to the gene with the closest TSS. Further analyses were performed with edgeR R package. Pearson's correlation was computed for each pair of

samples on log transformed CPM. As previously described for RNA-seq data, read counts were normalized with the TMM method using `calcNormFactors` function and dispersion was estimated with the `estimateDisp` function. Differences in peaks intensities across different conditions were evaluated fitting a negative binomial generalized linear model on the dataset with `glmQLFit` function and then performing a quasi-likelihood (QL) F-test with `glmQLFTest` function. Batch information was included in the design as covariate.

Definition of Induced and Differentially Induced ATAC-seq peaks

We first defined inducible peaks, namely those regions with $log_2FC_{CPM}>2.5$ and FDR<0.001 relative to naïve T cells in at least one condition or time point. For each time point, induced peaks were classified as induced at higher levels in the WT + rLCMV-core condition setting FDR < 0.1 and $log_2FC_{CPM} > 1.5$ (WT + rLCMV-core vs MUP-core) as cut-offs. Peaks with an FDR < 0.1 and a $log_2FC_{CPM} < -1.5$ in the WT + rLCMV-core vs MUP-core comparison were classified as induced at higher levels in MUP-core. The remaining peaks were defined as non-differentially induced between WT + rLCMV-core and MUP-core.

Motif Enrichment Analysis

Enrichment analysis of known motifs was performed with HOMER[101] using `findMotifsGenome.pl` script. For each time point we ranked ATAC-seq peaks according to log_2FC_{CPM} values in the WT + rLCMV-core versus MUP-core comparison and selected the 200 regions showing highest or lowest log_2FC_{CPM} values. These sets of differentially induced regions were compared to a background composed by a set of 3899 regions with unchanged intensities (FDR > 0.1 and abs(log_2FC) < 0.5) between both MUP-core and WT + rLCMV-core versus naïve in all time points.

Purification of viral nucleic acids from serum

Twenty µl of serum were incubated for 2 hours at 37°C with 180 µl IsoHi Buffer (150 mM NaCl, 0.5% NP40, 10 mM Tris pH 7.4), 5 mM $CaCl_2$, 5 mM MgCl2, 1U DNaseI (Life Technologies), 5U Micrococcal Nuclease (Life Technologies). The digestion was stopped by the addition of 20 mM EDTA pH 8.0 and viral nucleic acid purification performed with the QIAmp MiniElute Virus Spin Kit (Qiagen, Cat #57704), according to the manufacturer's instructions.

RT-qPCR

Total RNA was extracted from frozen livers using ReliaPrep™ RNA Tissue Miniprep System (Promega), according to the manufacturer's instructions, as described[102], genomic DNA contamination was removed using Ambion® TURBO DNA-freeTM DNase. 1 µg of total RNA was reverse transcribed with Superscript IV Vilo (Life Technologies) prior to qPCR analysis for mouse *il2* (TaqMan Mm00434256, Life Technologies), *ifng* (TaqMan Mm01168134, Life Technologies), HBV core (forward TACCGCCTCAGCTCTGTATC, reverse CTTCCAAATTAACACCCACCC, probe TCACCTCACCATACTGCACTCAGGCAA). Reactions were run and analysed on Quant Studio 5 instrument (Life Technologies). For viremia quantification, a standard curve was drawn using plasmid DNA. All experiments were performed in triplicate and normalized to the reference gene *GAPDH*.

Western blot analysis

Western blot analysis on frozen liver homogenates or on KCs was performed exactly as described[103]. Primary Abs include anti-STAT5 and anti-pSTAT5 (Tyr694) (rabbit; Cell Signaling #8215), anti-HBcAg (polyclonal, Dako), β-Actin (polyclonal; Abcam #ab228001) and H3 (polyclonal; abcam #ab1791). Secondary Ab include horseradish peroxidase-conjugated goat anti-rabbit IgG (Jackson ImmunoResearch). Reactive proteins were visualized using a Clarity Western ECL substrate kit (Bio-Rad), and exposure was performed using UVItec (Cambridge MINI HD, Eppendorf). Images were acquired by NineAlliance software. Band quantification was performed with ImageJ

software on 16-bit images and normalized on the matching housekeeping protein as a loading control. Each lane corresponds to a different mouse.

Southern blot analysis

Southern blot analysis on total DNA isolated from frozen livers (left lobe) was performed exactly as described[102].

Cell Purification

For the experiment described in **Fig. 19**, KCs were sorted from liver non-parenchymal cells as live, lineage negative ($CD3^-$, $CD19^-$, $Ly6G^-$, $CD49b^-$), $CD45^+$, $CD11b^{int}$, $F4/80^+$, $CD64^+$, $MHCII^+$, $TIM4^+$ cells. For the experiment described in **Fig. 20**, single cells were sorted from liver non-parenchymal cells as live, $CD45^+$, lineage negative ($CD3^-$, $CD19^-$, $Ly6G^-$, $CD49b^-$), $F4/80^+$, $CD64^+$ cells. For the experiment described in **Fig. 21**, KCs were sorted from liver non-parenchymal cells as live, $CD45^+$, $CD11b^{int}$, $F4/80^+$, $MHCII^+$, $TIM4^+$ cells. Among total KCs, KC1 were sorted as $CD206^-$ $ESAM^-$ cells and KC2 as $CD206^+$, $ESAM^+$ cells. Total KCs, KC1 and KC2 were flow cytometry-sorted with a 100 μm nozzle at 4°C on a FACSAria Fusion (BD) cell sorter in a buffer containing PBS with 2% FBS. Cells were always at least 98% pure (data not shown). In indicated experiments, $F4/80^+$ cells were purified from liver non-parenchymal cells by positive immunomagnetic separation (Miltenyi Biotec, #130-110-443), according to the manufacturer's instructions. In indicated experiments, $CD8^+$ T cells were purified from splenocytes using EasySep™ kit (StemCell # 19858), according to the manufacturer's instructions.

Single-cell RNA-Seq

Single cells were sorted on a 96-well plate and cDNA libraries were generated using the Smart-seq v2 protocol (Picelli et al., 2014) with the following modifications: i) 1mg/ml BSA Lysis buffer (Ambion® Thermo Fisher Scientific, Waltham, MA, USA); ii) use of 200 pg cDNA with 1/5 reaction of Illumina Nextera XT kit (Illumina, San Diego,

CA, USA). The length distribution of the cDNA libraries was monitored using a DNA High Sensitivity Reagent Kit on the Perkin Elmer Labchip (Perkin Elmer, Waltham, MA, USA). All samples were subjected to an indexed paired-end sequencing run of 2x151 cycles on an Illumina HiSeq 4000 system (Illumina, San Diego, CA, USA) (298 samples/lane). The RSEM tool (Li and Dewey, 2011) was used to perform Transcript Per Million (TPM) normalization starting from FASTQ files.

Single cell data analysis was performed using Seurat (v3.2.2) (Stuart et al., 2019). 169 cells were obtained after applying a filter to the TMP matrix of at least 200 genes expressed per cell and only genes expressed in at least 3 cells were retained. TPM expression was further normalized and scaled using the SCTransform function, and Umap reduction was then applied on first 12 Principal Components after running PCA. Unbiased clustering was made using the FindClusters function in Seurat with default parameters and a resolution value of 1. Specific markers for the different unbiased clusters were found using the function FindAllmarkers or FindMarkers in Seurat with default parameters and were then used for functional enrichment analysis with the online tool *Enrichr* (Kuleshov et al., 2016).

RNA Purification and RNA-seq Library Preparation

Bulk RNA-seq on $CD206^{-}CD107b^{-}$ and $CD206^{+}CD107b^{+}$ cells: between 20,000 and 50,000 cells were flow cytometry-sorted using CD206 (*Mrc1*) and CD107b (*Lamp2*) to identify $CD206^{-}$, $CD107b^{-}$ and $CD206^{+}$, $CD107b^{+}$ cells. Total RNA was extracted using Arcturus PicoPure. RNA Isolation kit (Arcturus. Thermo Fisher Scientific, Waltham, MA, USA) according to manufacturer's protocol. All Mouse RNAs were analyzed on Agilent Bioanalyser (Agilent, Santa Clara, CA, USA) for quality assessment with RNA Integrity Number (RIN) range from 5.8 to 6.7 and median of RIN 6.4. cDNA libraries were prepared using 2 ng of total RNA and 1ul of a 1:50,000 dilution of ERCC RNA Spike in Controls (Ambion. Thermo Fisher Scientific, Waltham, MA, USA) using the Smart-Seq v2 protocol (Picelli et al., 2014) with the following modifications: i) addition of 20 μM TSO; ii) use of 200 pg cDNA with 1/5 reaction of Illumina Nextera XT kit (Illumina, San Diego, CA, USA). The length distribution of the cDNA libraries was monitored using a DNA High Sensitivity Reagent Kit on the Perkin Elmer Labchip

(Perkin Elmer, Waltham, MA, USA). All samples were subjected to an indexed paired-end sequencing run of 2x151 cycles on an Illumina HiSeq 4000 system (Illumina) (25 samples/lane)

Bulk RNA-seq experiment on total KCs (shown in **Fig. 19**) and bulk RNA-seq experiment on sorted KC1 and KC2 (shown in **Fig. 21**): flow cytometry-sorted KCs, KC1 and KC2 were lysed in ReliaPrep™ RNA Cell Miniprep System (Promega #Z6011) and total RNA was isolated following manual extraction. DNA digestion was performed with TURBO DNA-free™ Kit (Invitrogen #AM1907). RNA was quantified with Qubit™ RNA HS Assay Kit (Invitrogen # Q32852) and analysis of its integrity was assessed with Agilent RNA 6000 Pico Kit (Agilent #5067-1513) on a Bioanalyser instrument. 6 RNA samples of sorted KC1 and KC2, were processed with the "SMART-seq Ultra Low Input 48" library protocol to obtain 30.0M clusters of fragments of 1x100nt of length through NovaSeq 6000 SP Reagent Kit (100 cycles).

RNA-Seq bioinformatics analysis

Bulk RNA-seq experiment on $CD206^-$, $CD107b^-$ and $CD206^+$, $CD107b^+$ cells: raw reads were obtained and mapped to the mouse genome build GRCm38. Gene counts were generated using featureCounts (part of the R subread package) (Liao et al., 2019) with GENCODE version M9 annotations. Differential Expression Analysis genes (DEGs) and MA plots were performed using the R package *edgeR* (Robinson et al., 2010).

Bulk RNA-seq experiment on total KCs (shown in **Fig. 19**) and on sorted KC1 and KC2 (shown in **Fig. 21**): raw reads were aligned to mouse genome build GRCm38 using STAR aligner (Dobin et al., 2013). Read counts per gene were then calculated using featureCounts based on GENCODE gene annotation version M16. Read counts were subject to log2 TPM (transcript per million) normalization to account for transcript length and library size.

Only genes with a TPM value higher than 1 in at least 4 (for the total KC experiment in **Fig. 19**) or 3 (for the KC2 vs KC1) samples were considered for following analysis. Differentially Expressed Genes (DEGs) between groups treated with IL-2c and PBS were identified by generating a linear model using LIMMA R package (Ritchie et al., 2015). Only DEGs with an adjusted P value < 0.05 (using Benjamini Hochberg

correction method) were selected for further analysis. For the final KC2 vs KC1 comparison an additional |logFC| > 1 filter was applied.

Functional Enrichment Analysis

Bulk RNA-seq analysis of the experiment described in **Fig. 19**: of the 4073 significant (FDR < 0.05) identified DEGs between control (PBS) and treated (IL-2c) samples, 1515 were up-regulated and 2558 were down-regulated. Those were subject to a functional enrichment analysis using the *EnrichR* R package (Kuleshov et al., 2016). Both the up- and the down-regulated DEGs were checked for any biological signature enrichment in both the Gene Ontology Biological Process Database (2018) and the Kyoto Encyclopedia of Genes and Genomes for Mouse (2019). After merging the results for the two databases, 858 significant (FDR < 0.05) Terms were identified, of which 428 were derived from the up-regulated DEGs and 430 from the down-regulated ones. To select the top enriched terms, only those with a high Combined Score (-log(p-value) * Odds Ratio) were considered. Based on the distribution of the Combined Score in the up-regulated terms and in the down-regulated ones, a threshold of 100 was chosen for the former, while a threshold of 30 for the latter.

Clustering of up-regulated Terms

For visualization and analysis, both up-regulated and down-regulated terms were subject to a clustering algorithm, to identify the most prominent biological signatures. Briefly, a Jaccard Index Similarity score was calculated for each pair set of terms, based on the DEGs annotated for each term, using an *in-house* developed script. Next, terms were clustered using a hierarchical clustering method, using as distance measure the Pearson correlation between the calculated Jaccard Index Similarity scores. An arbitrary number of clusters was selected and manually annotated based on the terms present. To visualize the result, the *pheatmap* R package was used.

Radar plots visualization

Radar plots were generated using the *fmsb* R package. Different sets of genes were selected based on literature analysis, defining different biological processes. For each category, the mean TPM expression for each gene within samples (separately for control and treated samples) was calculated. Next, the mean between all the genes belonging to a category was calculated and used as the value to represent the dimension in the radar plot.

Gene Set Enrichment Analysis

Gene Set Enrichment Analysis (GSEA) from bulk RNA-seq of KC1 and KC2 (**Fig. 21**) was performed using the GseaPreranked Java tool (Subramanian et al., 2005) using pre-ranked Log2 fold changes between KC2 and KC1 populations in expressed genes. HALLMARK_IL2_STAT5_SIGNALING Gene Set contained in MsigDB (Broad Institute) (Liberzon et al., 2015), Version 6. Since the gene set is based on human genes, mouse orthologs in humans were identified using the *homologene* R package (https://CRAN.R-project.org/package=homologene).

Immunoblot analysis

Immunoblot on plated KCs was performed as described (Zordan et al., 2018). Primary Abs include anti-STAT5 and anti-pSTAT5 (Tyr694) (rabbit; Cell Signaling Technology #8215) and β-actin (polyclonal; Abcam ab228001). As secondary Ab horseradish peroxidase-conjugated goat anti-rabbit IgG (Jackson ImmunoResearch, Cat# 111-035-003) was used. Reactive proteins were visualized using a Clarity Western ECL substrate kit (Bio-Rad), and exposure was performed using UVItec (Cambridge MINI HD, Eppendorf). Images were acquired by NineAlliance software.

Confocal Immunofluorescence Histology and Histochemistry

Confocal microscopy analysis of livers was performed as described (Guidotti et al., 2015). For confocal images of KC1 and KC2, C57BL/6 mice were injected i.v. with 2 μg of anti-F4/80 Alexa Fluor 488 (BioLegend, #123120) and 2 μg of anti-CD206 APC

(BioLegend, #141708) 10 minutes before harvesting the liver. The liver was fixed overnight in PBS with 4% paraformaldehyde and subsequently incubated for 24h in PBS with 30% sucrose. Next, liver lobes were embedded in O.C.T (Killik Bio-Optica) and cut at -14°C into 60 μm thick sections with a cryostat. Sections were blocked for 15 min with blocking buffer (PBS, 0.5% BSA, 0.3 % Triton) and stained for 1h at room temperature (RT) with anti-CD38 Alexa Fluor 594 (BioLegend, #102725) in wash/stain buffer (PBS, 0.2% BSA, 0.1% triton). Sections were then washed twice for 5 min, stained with DAPI (Sigma**)** for 5 min, washed again and mounted for imaging with FluorSave™ Reagent (Millipore). For additional confocal imaging, the following primary Abs were used for staining: anti-CD45.1 AF647 (110720, BioLegend), anti-F4/80 (BM8, Invitrogen), anti-Lyve-1 (NB600-1008, Novus Biological), anti-CD38 (102702, BioLegend). The following secondary Abs were used for staining: Alexa Fluor 488-, Alexa Fluor 514-, Alexa Fluor 568-conjugated anti-rabbit or anti-rat IgG (Life Technologies). Image acquisition was performed with a 63x oil-immersion or 20x objective on an SP5 or SP8 confocal microscope (Leica Microsystem). To minimize fluorophore spectral spillover, the Leica sequential laser excitation and detection modality was used. Where necessary to compensate for uneven slide illumination, fluorescent intensity of layers was normalized using Imaris normalize Layers tool. Where necessary, autofluorescence was filtered from the image by channel subtraction of a deep red autofluorescent channel from APC signal with the Imaris Channel Arithmetics tool.

Intravital Multiphoton Microscopy

Liver intravital multiphoton microscopy was performed as described[57,84]. Liver sinusoids were visualized by injecting nontargeted Quantum Dots 655 (Invitrogen) i.v. during image acquisition. Images were acquired with a LaVision BioTec TriMScope II coupled to a Nikon Ti-U inverted microscope enclosed in a custom-built environmental chamber (Life Imaging Services) that was maintained at 37-38°C with heated air. Continuous body temperature monitoring through a rectal probe was performed to ensure that a narrow range of 37–38°C was always maintained. Fluorescence excitation was provided by two tuneable femtosecond (fs)- pulsed Ti:Sa lasers (680–1080 nm, 120 fs pulse-width, 80 MHz repetition rate, Ultra II, Coherent), an Optical Parametric Oscillator

(1000–1600 nm, 200 fs pulse-width, 80 MHz repetition rate, Chameleon Compact OPO, Coherent). The setup includes four non-descanned photomultiplier tubes (Hamamatsu H7422-40 GaAsP High Sensitivity PMTs and Hamamatsu H7422-50 GaAsP High Sensitivity red-extended PMT from Hamamatsu Photonics K.K.), a 25X, 1.05 NA, 2 mm working distance, water-immersion multiphoton objective (Olympus). For 4D analysis of cell migration, stacks of 7-15 square xy sections (512 × 512 pixel) sampled with 4 μm z spacing were acquired every 5-32 s for up to 2 hours, to provide image volumes that were 40 μm in depth and with an xy field of view variable between 100×100 μm^2 and 450×450 μm^2. Sequences of image stacks were transformed into volume-rendered, 4D time-lapse movies with Imaris (Bitplane). The 3D positions of the cell centroids were segmented by semi-automated cell tracking algorithm of Imaris. The semiautomatic surface-rendering module in Imaris (Bitplane) was used to create 3D volumetric surface objects corresponding either to individual cells or to the liver vascular system. Signal thresholds were determined using the Imaris Surface Creation module, which provides automatic threshold.

Biochemical Analyses

The extent of hepatocellular injury was monitored by measuring serum alanine aminotransferase (sALT) activity at multiple time points after treatment, as previously described (Guidotti et al., 2015). Serum HBeAg was measured by enzyme-linked immunosorbent assays (ELISA), as previously described (Guidotti et al., 2015). Blood cell counts were measured by Vet abc™ (scil).

QUANTIFICATION AND STATISTICAL ANALYSIS

Results are expressed as mean ± s.e.m. All statistical analyses were performed in Prism (GraphPad Software), and details are provided in the figure legends. Normality of data distribution was tested in all graphs with a Shapiro-Wilk or D'Agostino & Pearson normality test and parametric tests were chosen only when normality could be confirmed for each dataset. One-tailed test were chosen over two-tailed test when basic biology dictates that the change between the control and treatment group can only occur into one direction (e.g., in cell depletion experiments, where the number of cells will be decreased in the treatment vs the control group). Comparisons are not statistically significant unless indicated.

13. REFERENCES

1. Treuting, P. M. & Dintzis, S. M. Comparative anatomy and histology : a mouse and human atlas. in *Comparative anatomy and histology : a mouse and human atlas* 461 (2012).

2. Sherif R. Z. Abdel-Misih, M. B. Liver Anatomy. **90**, 643–653 (2014).

3. Crispe, I. N. Hepatic T cells and liver tolerance. *Nat. Rev. Immunol.* **3**, 51–62 (2003).

4. Zheng, M., Yu, J. & Tian, Z. Characterization of the liver-draining lymph nodes in mice and their role in mounting regional immunity to HBV. *Cell. Mol. Immunol.* **10**, 143–150 (2013).

5. Krenkel, O. & Tacke, F. Liver macrophages in tissue homeostasis and disease. doi:10.1038/nri.2017.11

6. Crispe, I. N. The Liver as a Lymphoid Organ. doi:10.1146/annurev.immunol.021908.132629

7. Mackay, I. Hepatoimmunology: A perspective. 36–44 (2002).

8. Knolle, P. *et al.* Human Kupffer cells secrete IL-10 in response to lipopolysaccharide (LPS) challenge. 226–229 (1995).

9. Catala, M., Anton, A. & Portoles, M. Characterization of the simultaneous binding of Escherichia coli endotoxin to Kupffer and endothelial liver cells by flow cytometry. *Cytometry* **283**, 280–283 (1998).

10. Balmer, M. L. *et al.* The Liver May Act as a Firewall Mediating Mutualism Between the Host and Its Gut Commensal Microbiota. *Sci. Transl. Med.* **6**, 237ra66-237ra66 (2014).

11. Mingozzi, F. *et al.* Induction of immune tolerance to coagulation factor IX antigen by in vivo hepatic gene transfer. **111**, 1347–1356 (2003).

12. Radziewicz, H. *et al.* Liver-Infiltrating Lymphocytes in Chronic Human Hepatitis C Virus Infection Display an Exhausted Phenotype with High Levels of PD-1 and Low Levels of CD127 Expression. *J. Virol.* **81**, 2545–2553 (2007).

13. Guidotti, L. G., Isogawa, M. & Chisari, F. V. Host-virus interactions in hepatitis B virus infection. *Curr Opin Inmunol* **36**, 61–66 (2015).

14. Kamada, N. The immunology of experimental liver transplantation in the rat.

Immunology **55**, 369–387 (1985).

15. Qian, S. *et al.* Murine Liver Allograft Transplantation: Tolerance and Donor Cell Chimerism. *Hepatology* **19**, 916–924 (2010).

16. Bishop, G. A. & Mccaughan, G. W. Immune Activation Is Required for the Induction of Liver Allograft Tolerance : Implications for Immunosuppressive Therapy. **7**, 161–172 (2001).

17. John, B., Klein, I. & Crispe, I. N. Immune Role of Hepatic TLR-4 Revealed by Orthotopic Mouse Liver Transplantation. (2007). doi:10.1002/hep.21446

18. Lopez, B. G., Tsai, M. S., Baratta, J. L., Longmuir, K. J. & Robertson, R. T. Characterization of Kupffer cells in livers of developing mice. *Comp. Hepatol.* **10**, 2 (2011).

19. Crispe, I. N. Liver antigen-presenting cells. *J. Hepatol.* **54**, 357–365 (2011).

20. Bilzer, M., Roggel, F. & Gerbes, A. L. Role of Kupffer cells in host defense and liver disease. *Liver Int. Off. J. Int. Assoc. Study Liver* **26**, 1175–1186 (2006).

21. Gomez Perdiguero, E. *et al.* Tissue-resident macrophages originate from yolk-sac-derived erythro-myeloid progenitors. *Nature* **518**, 547–551 (2015).

22. Scott, C. L. *et al.* Bone marrow-derived monocytes give rise to self-renewing and fully differentiated Kupffer cells. *Nat. Commun.* **7**, 10321 (2016).

23. You, Q., Cheng, L., Kedl, R. M. & Ju, C. Mechanism of T cell tolerance induction by murine hepatic Kupffer cells. *Hepatology* **48**, 978–990 (2008).

24. M Isogawa, J. C. Y. M. K. K. F. C. CD40 activation rescues antiviral CD8+ T cells from PD-1-mediated exhaustion. *PLoS Pathog.* **9**, e1003490 (2013).

25. Heymann, F. & Tacke, F. Immunology in the liver--from homeostasis to disease. *Nat. Rev. Gastroenterol. Hepatol.* **13**, 88–110 (2016).

26. Kudo, S., Matsuno, K., Ezaki, T. & Ogawa, M. A novel migration pathway for rat dendritic cells from the blood: hepatic sinusoids-lymph translocation. *J. Exp. Med.* **185**, 777–784 (1997).

27. J. Cohen, D. Griffin, R. Lamb, M. Martin, V. Racanello, B. R. *Field's Virology*. (2013).

28. Fattovich, G. Natural history of hepatitis B. *J. Hepatol.* **39**, 50–58 (2003).

29. Yan, H. *et al.* Sodium taurocholate cotransporting polypeptide is a functional receptor for human hepatitis B and D virus. *Elife* **2012**, 1–28 (2012).

30. Rehermann, B. & Nascimbeni, M. Immunology of hepatitis B virus and hepatitis C virus infection. *Nat. Rev. Immunol.* **5**, 215–229 (2005).

31. Liaw, Y. F. & Chu, C. M. Hepatitis B virus infection. *Lancet* **373**, 582–592 (2009).

32. Chisari, Francis V; Isogawa, M; Wieland, S., Chisari, F. V, Isogawa, M. & Wieland, S. F. Pathogenesis of Hepatitis B virus infection. *Pathol Biol* **58**, 258–266 (2010).

33. Xia, Y. *et al.* Secreted Interferon-Inducible Factors Restrict Hepatitis B and C Virus Entry in Vitro. *J. Immunol. Res.* **2017**, (2017).

34. Jilbert, A. R. *et al.* Rapid resolution of duck hepatitis B virus infections occurs after massive hepatocellular involvement. *J Virol* **66**, 1377–1388 (1992).

35. Thimme, R. *et al.* CD8 + T Cells Mediate Viral Clearance and Disease Pathogenesis during Acute Hepatitis B Virus Infection CD8+ T Cells Mediate Viral Clearance and Disease Pathogenesis during Acute Hepatitis B Virus Infection †. *J Virol.* **77**, 68–76 (2003).

36. Iannacone, M. & Guidotti, L. Mouse Models of Hepatitis B Virus Pathogenesis. (2015). doi:10.1101/cshperspect.a021477

37. Isogawa, M., Chung, J., Murata, Y., Kakimi, K. & Chisari, F. V. CD40 Activation Rescues Antiviral CD8+ T Cells from PD-1-Mediated Exhaustion. *PLoS Pathog.* **9**, 1–16 (2013).

38. Spolski, R., Li, P. & Leonard, W. J. Biology and regulation of IL-2: from molecular mechanisms to human therapy. *Nat. Rev. Immunol.* **18**, 648–659 (2018).

39. Ross, S. H. & Cantrell, D. A. Signaling and Function of Interleukin-2 in T Lymphocytes. *Annu. Rev. Immunol.* **36**, 411–433 (2018).

40. Wang, X., Rickert, M. & Garcia, K. C. Structure of the quaternary complex of interleukin-2 with its alpha, beta, and gammac receptors. *Science* **310**, 1159–1163 (2005).

41. Chinen, T. *et al.* An essential role for the IL-2 receptor in T(reg) cell function. *Nat. Immunol.* **17**, 1322–1333 (2016).

42. Jiang, T., Zhou, C. & Ren, S. Role of IL-2 in cancer immunotherapy. *Oncoimmunology* **5**, e1163462 (2016).

43. Donohue, J. H. & Rosenberg, S. A. The fate of interleukin-2 after in vivo administration. *J. Immunol.* **130**, 2203–2208 (1983).

44. Létourneau, S. *et al.* IL-2/anti-IL-2 antibody complexes show strong biological activity by avoiding interaction with IL-2 receptor alpha subunit CD25. *Proc. Natl. Acad. Sci. U. S. A.* **107**, 2171–2176 (2010).

45. Germain, R. N., Robey, E. A. & Cahalan, M. D. A Decade of Imaging Cellular

Motility and Interaction Dynamics in the Immune System. **336**, 1676–1682 (2012).

46. Benechet, A. P., Menon, M. & Khanna, K. M. Visualizing T cell migration in situ. *Front. Immunol.* **5**, 1–12 (2014).

47. von Andrian, U. H. Intravital microscopy of the peripheral lymph node microcirculation in mice. *Microcirculation* **3**, 287–300 (1996).

48. Amino, R. *et al.* Imaging malaria sporozoites in the dermis of the mammalian host. *Nat. Protoc.* **2**, 1705–1712 (2007).

49. Tavares, J. *et al.* Role of host cell traversal by the malaria sporozoite during liver infection. *J. Exp. Med.* **210**, 905–915 (2013).

50. Harris, T. H. *et al.* Generalized Lévy walks and the role of chemokines in migration of effector CD8+ T cells. *Nature* 3–7 (2012). doi:10.1038/nature11098

51. Miller, M. J. Two-Photon Imaging of Lymphocyte Motility and Antigen Response in Intact Lymph Node. *Science (80-.).* **296**, 1869–1873 (2002).

52. Herz, J., Zinselmeyer, B. H. & McGavern, D. B. Two-Photon Imaging of Microbial Immunity in Living Tissues. *Microsc. Microanal.* **18**, 730–741 (2012).

53. Salmon, H. *et al.* Ex vivo imaging of T cells in murine lymph node slices with widefield and confocal microscopes. *J. Vis. Exp.* 1–5 (2011). doi:10.3791/3054

54. Salmon, H. *et al.* Matrix architecture defines the preferential localization and migration of T cells into the stroma of human lung tumors. *J Clin Invest* **122**, 899–910 (2012).

55. Moreau, H. D. *et al.* Dynamic in situ cytometry uncovers t cell receptor signaling during immunological synapses and kinapses in vivo. *Immunity* **37**, 351–363 (2012).

56. Murooka, T. T. & Mempel, T. R. Multiphoton intravital microscopy to study lymphocyte motility in lymph nodes. *Methods Mol. Biol.* **757**, 247–257 (2011).

57. Benechet, A. P., Ganzer, L. & Iannacone, M. Intravital Microscopy Analysis of Hepatic T Cell Dynamics. **1514**, (2017).

58. A Bertoletti, C. F. Adaptive immunity in HBV infection. *J. Hepatol.* **64**, S71–S83 (2016).

59. LG Guidotti, B. M. H. S. F. C. High-level hepatitis B virus replication in transgenic mice. *J. Virol.* **69**, 6158–6169 (1995).

60. LG Guidotti, V. M. Y. L. C. R. F. C. Hepatitis B virus nucleocapsid particles do not cross the hepatocyte nuclear membrane in transgenic mice. *J. Virol.* **68**, 5469–5475 (1994).

61. Sitia, G. Kupffer cells hasten resolution of liver immunopathology in mouse models of viral hepatitis. *PLoS Pathog.* **7**, e1002061 (2011).

62. Wherry, E. Molecular signature of CD8+ T cell exhaustion during chronic viral infection. *Immunity* **27**, 670–684 (2007).

63. Best, J. Transcriptional insights into the CD8+ T cell response to infection and memory T cell formation. *Nat. Immunol.* **14**, 404–412 (2013).

64. Dominguez, C. The transcription factors ZEB2 and T-bet cooperate to program cytotoxic T cell terminal differentiation in response to LCMV viral infection. *J. Exp. Med.* **212**, 2041–2056 (2015).

65. Kurachi, M. The transcription factor BATF operates as an essential differentiation checkpoint in early effector CD8+ T cells. *Nat. Immunol.* **15**, 373–383 (2014).

66. Chen, J. NR4A transcription factors limit CAR T cell function in solid tumours. *Nature* **567**, 530–534 (2019).

67. Liu, X. Genome-wide analysis identifies NR4A1 as a key mediator of T cell dysfunction. *Nature* **567**, 525–529 (2019).

68. Scott-Browne, J. Dynamic changes in chromatin accessibility occur in CD8+ T cells responding to viral infection. *Immunity* **45**, 1327–1340 (2016).

69. Sen, D. R. *et al.* The epigenetic landscape of T cell exhaustion. *Science (80-.).* **354**, 1165 LP – 1169 (2016).

70. A Schietinger, J. D. R. B. J. B. P. G. Rescued tolerant CD8 T cells are preprogrammed to reestablish the tolerant state. *Science (80-.).* **335**, 723–727 (2012).

71. AH Sharpe, K. P. The diverse functions of the PD1 inhibitory pathway. *Nat. Rev. Immunol.* **18**, 153–167 (2018).

72. R Spolski, P. L. W. L. Biology and regulation of IL-2: from molecular mechanisms to human therapy. *Nat. Rev. Immunol.* **18**, 648–659 (2018).

73. Manske, K. Outcome of anti-viral immunity in the liver is shaped by the level of antigen expressed in infected hepatocytes. *Hepatology* **68**, 2089–2105 (2018).

74. Tolksdorf, F. The PDL1-inducible GTPase Arl4d controls T effector function by limiting IL-2 production. *Sci. Rep.* **8**, (2018).

75. O Boyman, M. K. M. R. C. S. J. S. Selective stimulation of T cell subsets with antibody-cytokine immune complexes. *Science (80-.).* **311**, 1924–1927 (2006).

76. BD Brown, M. V. A. Z. L. S. S. L. N. Endogenous microRNA regulation suppresses transgene expression in hematopoietic lineages and enables stable

gene transfer. *Nat. Med.* **12**, 585–591 (2006).

77. Bénéchet, A. P. *et al.* Dynamics and genomic landscape of CD8+ T cells undergoing hepatic priming. *Nature* **574**, 200–205 (2019).

78. Picelli, S. Full-length RNA-seq from single cells using Smart-seq2. *Nat. Protoc.* **9**, 171–181 (2014).

79. Huang, A. C. *et al.* T-cell invigoration to tumour burden ratio associated with anti-PD-1 response. *Nature* **545**, 60–65 (2017).

80. Joffre, O. P., Segura, E., Savina, A. & Amigorena, S. Cross-presentation by dendritic cells. *Nat. Rev. Immunol.* **12**, 557–569 (2012).

81. Raeber, M. E., Rosalia, R. A., Schmid, D., Karakus, U. & Boyman, O. Interleukin-2 signals converge in a lymphoid-dendritic cell pathway that promotes anticancer immunity. *Sci. Transl. Med.* **12**, (2020).

82. Freitas-Lopes, M., Mafra, K., David, B., Carvalho-Gontijo, R. & Menezes, G. Differential Location and Distribution of Hepatic Immune Cells. *Cells* **6**, 48 (2017).

83. Pachella, L. A., Madsen, L. T. & Dains, J. E. The Toxicity and Benefit of Various Dosing Strategies for Interleukin-2 in Metastatic Melanoma and Renal Cell Carcinoma. *J. Adv. Pract. Oncol.* **6**, 212–221 (2015).

84. Guidotti, L. Immunosurveillance of the liver by intravascular effector CD8+ T cells. *Cell* **161**, 486–500 (2015).

85. Cantore, A. Liver-directed lentiviral gene therapy in a dog model of hemophilia B. *Sci. Transl. Med.* **7**, 277ra28-277ra28 (2015).

86. Mátrai, J. Hepatocyte-targeted expression by integrase-defective lentiviral vectors induces antigen-specific tolerance in mice with low genotoxic risk. *Hepatology* **53**, 1696–1707 (2011).

87. Reeves, J. P., Reeves, P. A. & Chin, L. T. Survival surgery: removal of the spleen or thymus. *Curr. Protoc. Immunol.* **Chapter 1**, Unit 1.10 (2001).

88. Dobin, A. STAR: ultrafast universal RNA-seq aligner. *Bioinformatics* **29**, 15–21 (2013).

89. Y Liao, G. S. W. S. The Subread aligner: fast, accurate and scalable read mapping by seed-and-vote. *Nucleic Acids Res.* **41**, e108–e108 (2013).

90. MD Robinson, D. M. G. S. edgeR: a Bioconductor package for differential expression analysis of digital gene expression data. *Bioinformatics* **26**, 139–140 (2010).

91. MD Robinson, A. O. A scaling normalization method for differential expression

analysis of RNA-seq data. *Genome Biol.* **11**, (2010).

92. Subramanian, A. Gene set enrichment analysis: a knowledge-based approach for interpreting genome-wide expression profiles. *Proc. Natl Acad. Sci. USA* **102**, 15545–15550 (2005).

93. G Yu, L.-G. W. Y. H. Q.-Y. H. clusterProfiler: an R package for comparing biological themes among gene clusters. *OMICS* **16**, 284–287 (2012).

94. F Supek, M. B. N. Š. T. Š. REVIGO summarizes and visualizes long lists of gene ontology terms. *PLoS One* **6**, e21800 (2011).

95. JH Bullard, E. P. K. H. S. D. Evaluation of statistical methods for normalization and differential expression in mRNA-Seq experiments. *BMC Bioinformatics* **11**, (2010).

96. JD Buenrostro, B. W. H. C. W. G. ATAC-seq: A Method for Assaying Chromatin Accessibility Genome-Wide. *Curr. Protoc. Mol. Biol.* **109**, 21.29.1–9 (2015).

97. H Li, R. D. Fast and accurate short read alignment with Burrows-Wheeler transform. *Bioinformatics* **25**, 1754–1760 (2009).

98. Li, H. The Sequence Alignment/Map format and SAMtools. *Bioinformatics* **25**, 2078–2079 (2009).

99. Zhang, Y. Model-based analysis of ChIP-Seq (MACS). *Genome Biol.* **9**, (2008).

100. Zhu, L. ChIPpeakAnno: a Bioconductor package to annotate ChIP-seq and ChIP-chip data. *BMC Bioinformatics* **11**, (2010).

101. Heinz, S. Simple combinations of lineage-determining transcription factors prime cis-regulatory elements required for macrophage and B cell identities. *Mol. Cell* **38**, 576–589 (2010).

102. Fioravanti, J. Effector CD8+ T cell-derived interleukin-10 enhances acute liver immunopathology. *J. Hepatol.* **67**, 543–548 (2017).

103. Zordan, P. Tuberous sclerosis complex-associated CNS abnormalities depend on hyperactivation of mTORC1 and Akt. *J. Clin. Invest.* **128**, 1688–1706 (2018).

104. Helmchen, F. & Denk, W. Deep tissue two-photon microscopy. (2005).

105. Zipfel, W. R., Williams, R. M. & Webb, W. W. Nonlinear magic: multiphoton microscopy in the biosciences. **21**, 1369–1378 (2003).